PIEZOELECTRIC ARTIFICIAL KELP:

EXPERIMENTALLY VALIDATED PARAMETER OPTIMIZATION

OF A QUASI-STATIC, FLOW-DRIVEN ENERGY HARVESTER

A Thesis

by

ALEXANDER MORGAN PANKONIEN

Submitted to the Office of Graduate Studies of
Texas A&M University
in partial fulfillment of the requirements for the degree of

MASTER OF SCIENCE

August 2011

Major Subject: Aerospace Engineering

Piezoelectric Artificial Kelp: Experimentally Validated Parameter Optimization of a Quasi-Static, Flow-Driven Energy Harvester

PIEZOELECTRIC ARTIFICIAL KELP:

EXPERIMENTALLY VALIDATED PARAMETER OPTIMIZATION

OF A QUASI-STATIC, FLOW-DRIVEN ENERGY HARVESTER

A Thesis

by

ALEXANDER MORGAN PANKONIEN

Submitted to the Office of Graduate Studies of
Texas A&M University
in partial fulfillment of the requirements for the degree of

MASTER OF SCIENCE

Approved by:

Chair of Committee,	Zoubeida Ounaies
Committee Members,	Robert Randall
	John Hurtado
Head of Department,	Dimitris Lagoudas

August 2011

Major Subject: Aerospace Engineering

ABSTRACT

Piezoelectric Artificial Kelp: Experimentally Validated Parameter Optimization of a Quasi-Static, Flow-Driven Energy Harvester. (August 2011)

Alexander Morgan Pankonien, B.S., Texas A&M University

Chair of Advisory Committee: Dr. Zoubeida Ounaies

Piezoelectric energy harvesting is the process of taking an external mechanical input and converting it directly into electrical energy via the piezoelectric effect. To determine the power created by a piezoelectric energy harvester, a specific application with defined input and design constraints must first be chosen. The following thesis established a concept design of a hydrokinetic energy harvesting system, the piezoelectric artificial kelp (PAK), which uses piezoelectric materials to harvest coastal ocean waves while having a beneficial impact on the surrounding environment. The harvester design mimics the configuration of sea-kelp, a naturally occurring plant that anchors to the ocean floor and extends into the water column. Underwater currents caused by wave-action result in periodic oscillations in the kelp. In order to determine the average power generated by this design concept, predictive tools were devised that allowed for the determination of the optimized average power produced by the piezoelectric energy harvester. For a stiff energy harvester, the linear differential equations were analytically solved to find an equation for the average power generated as a function of design parameters. These equations were used to compare the effect on power output of the design configuration and piezoelectric material choice between a piezopolymer (PVDF) and a piezoceramic (PZT). The homogeneous bimorph was found to have the optimal design configuration and it was shown that a harvester constructed using PVDF would produce approximately 1.6 times as much power as one using PZT. For a flexible energy harvester, an iterative nonlinear solution technique using an

assumed polynomial solution for the local curvature of the energy harvester was used to verify and extend the analytic solutions to large deflections. An energy harvester was built using off-the-shelf piezoelectric elements and tested in a wave tank facility to validate experimentally the voltage and average power predicted by the analytical solution. The iterative code showed the PAK harvester to produce volumetric power on the order of other energy harvesting concepts (17.8 $\mu W/cm^3$). Also, a full-scale PAK harvester approximately ten meters long in typical wave conditions was found to produce approximately one watt of power.

DEDICATION

To my wife, my family, and everyone who has taken a risk

Problems cannot be solved with the same level thinking that created them.
–Albert Einstein

Growth and change are the law of all life. Yesterday's answers are inadequate for today's problems – just as the solutions of today will not fill the needs of tomorrow.
–Franklin D. Roosevelt

ACKNOWLEDGEMENTS

I would like to thank my wife, Ambi, for all of her support throughout the many frustrations of the research process and my family for their continual encouragement. I am also incredibly grateful to my advisor, Dr. Zoubeida Ounaies, for her continued willingness to consider patiently and critically many long-winded thoughts, for believing in my ability to succeed, and providing me with the means to succeed. I would like to thank my other committee members, Dr. Hurtado and Dr. Randall, for giving so freely of their time and resources to help guide me through unfamiliar territory to useful answers. I would also like to thank Dr. Boyd for providing the data acquisition equipment for the experimental testing. I would like to thank Dr. Randall for providing the wave tank for the experimental testing and John Reed for the repeated advice on its renovation and use. Thanks to Ross Flach and the other members of the Aerospace Engineering Machine Shop for timely and critical help in assembling the clamp setup. The author would also like to thank Dr. Jeffrey Martin from Sandia Labs for both the concept design and coining of the phrase: piezoelectric artificial kelp system.

NOMENCLATURE

$[]^E$	Constant Electrical Field
$[]^S$	Constant Strain
$[]^T$	Constant Stress
b	Beam Width
d	Stress-Charge Piezoelectric Coupling Coefficients
D	Charge Displacement
e	Strain-Charge Piezoelectric Coupling Coefficients
ε	Permittivity
E	Electric Field
h	Beam Thickness
PVDF	Polyvinylidene Fluoride
PZT	Lead Zirconate Titanate
Q	Charge
R_{int}	Internal Resistance
s	Compliance
S	Strain
t	Layer Thickness
T	Stress
Y_i	Stiffness of Inert Material
Y_p	Stiffness of Piezoelectric Material

TABLE OF CONTENTS

Page

Page

LIST OF FIGURES

Page

Page

Page

LIST OF TABLES

Page

1. INTRODUCTION AND PROBLEM STATEMENT

1.1 Introduction to Alternative Energy

In the past few years, significant attention has been given by the Department of Energy to develop methods for harvesting electrical energy from alternative sources, such as hydrokinetic power harvested from the ocean. The Electric Power Research Institute has estimated that the annual average incident wave energy at 60 m depth off the U.S. coastline is 2,100 TWh per year [1]. To bring perspective to this number, according to the Department of Energy's website, in 2005 the United States used approximately 3,600 TWh of electricity a year. Overseas, countries such as Britain have established programs to examine harvesting this abundant energy source. The Scottish government has invested in the creation of the Saltire Prize, which is "£10 million awarded to any team demonstrating in Scottish waters, commercially viable wave or tidal energy technology achieving minimum electrical output of 100 GWh over a continuous 2 year period using only the power of the sea." That is to say the prize is awarded for a system that can produce .0014% of the US daily needs. Clearly, projects that can show competitive feasibility in terms of cost, power density, reliability and environmental impact on a national scale have a significant opportunity to flourish. In this thesis, the investigations focus on demonstrating the feasibility of using piezoelectric materials to convert the natural mechanical motions seen in kelp forests due to oceanic wave action, into electricity.

1.2 Introduction to Piezoelectricity

First discovered in quartz by the Curie brothers in 1880, piezoelectric materials exhibit the ability to directly convert mechanical energy into electrical energy, and vice

---

This thesis follows the style of *IEEE Transactions on Ultrasonics, Ferroelectrics and Frequency Control.*

versa [2]. Although early research primarily focused upon naturally occurring materials, many other types of piezoelectric materials have been discovered, including ceramics, polymers and composites [2]. Today, commonly used piezoelectric materials include the piezoceramic lead zirconate titanate (PZT) and the piezopolymer polyvinylidene fluoride (PVDF). The word "piezoelectric" is derived from a combination of "piezo" meaning force or pressure, and electricity. Applying a compressive stress to the material displaces charge, resulting in charge flow across the boundaries of the material, referred to as the direct piezoelectric effect [3]. If an equal but opposite tensile stress is applied rather than a compressive stress, then the displaced charge will be equal in magnitude but opposite in sign. For example, if the oppositely charge surfaces of a piezoelectric material with applied stress, σ, are connected via a circuit, with an impedance, Z, then a charge, Q, will flow through the circuit according to the circuit's impedance and produce a voltage, V, as shown in Figure 1.

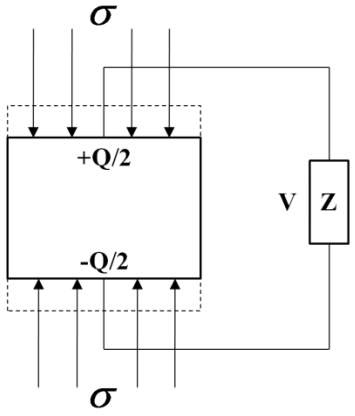

Figure 1: The Direct Piezoelectric Effect

Conversely, if a voltage or charge is applied to the material, the material will experience a body force that will induce an internal stress in the material through the inverse piezoelectric effect that, if unblocked, will lead to a resultant strain [3]. The electromechanical coupling in piezoelectric materials is commonly expressed as a set of linear equations that can be written in terms of any of the electromechanical coupling

coefficients: d, e, g, or h. Described in terms of stress-electric field relations, the linear coupling can be written as:

$$D = dT + \varepsilon^T E \quad (1)$$

$$S = s^E T + dE \quad (2)$$

where "ε^T" is the permittivity of the piezoelectric material under constant stress conditions and "s^E" is the mechanical compliance of the material under constant electrical field conditions. Note that the conditions at which the electrical material parameter was measured must be noted for piezoelectric materials, because of the electromechanical coupling and vice versa. The convention states that the superscript $[]^T$ denotes an electrical parameter measured under constant stress conditions, $[]^S$ denotes an electrical parameter measured under constant strain conditions. Similarly, $[]^E$ denotes a mechanical parameter measured under constant electrical field. Alternatively, for the purposes of clarity, the equations can be written in partially inverted forms as the strain-electric field relations:

$$D = eS + \varepsilon^S E \quad (3)$$

$$T = c^E S + eE \quad (4)$$

where "c^E" is the mechanical stiffness of the material, the inverse of the mechanical compliance. By defining a coordinate system within the material, the above equation can be simplified for a material in a uniaxial stress state in the 1-direction and electric field applied in the 3-direction, as shown in

Figure **2**.

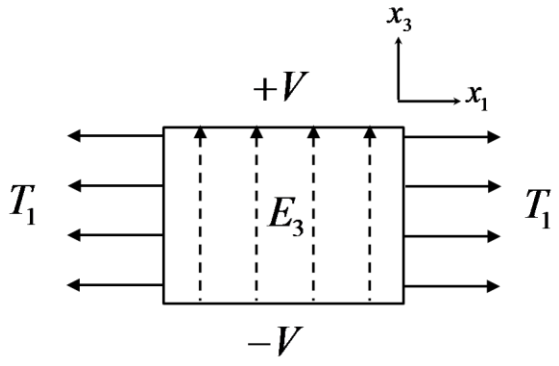

Figure 2: Stress State and Electrical Field in 1-3 Material Plane

The previous equations then reduce to:

$$D_{31} = e_{31} S_1 + \varepsilon_{33}^S E_3 \quad (5)$$

$$T_1 = c_{11} S_1 + e_{31} E_3 \quad (6)$$

where the coefficients are related according to the equations below. Note that Y is the storage modulus of a material. For the purposes of this paper, the storage modulus was approximated to be transversely isotropic in the 1-2 plane and thus not dependent upon material orientation in this plane. Another convention was defined where the subscript $[]_p$ represents the piezoelectric material, and $[]_i$ denotes the inactive material. Accordingly, Y_p is assumed to be the storage modulus of the piezoelectric material.

$$c_{11}^E = \frac{1}{s_{11}^E} = Y_p \quad (7)$$

$$e_{31} = d_{31} Y_p \quad (8)$$

$$\varepsilon_{33}^S = \varepsilon_{33}^T - d_{31}{}^2 Y_p \quad (9)$$

1.3 Introduction to Piezoelectric Energy Harvesting

In the past decade, piezoelectric energy harvesting has become a topic of scientific focus. In vibration-based energy harvesting, a vibrating inertial mass is bonded to a piezoelectric element which develops stresses as a result of the vibrations. The changing stresses induce a current in the circuit via the electromechanical coupling in the material, demonstrating a novel means to recover waste vibration energy [4-6]. In a cantilevered beam configuration, shown in Figure 3, the vibrations act as an applied moment to the beam via the beam's inertia. The beam then undergoes transverse deflections which result in bending and internal stresses that create an internal moment balancing the applied moment.

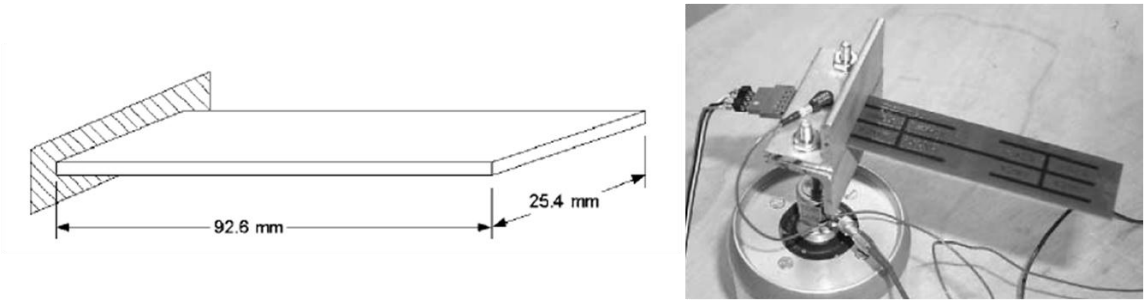

Figure 3: Cantilevered Beam [7]

Sodano et. al considered a cantilever beam configuration to demonstrate harvesting of vibration energy [7]. By assuming small transverse deflections and Euler-Bernoulli beam theory a set of linear dynamic equations were found and solved using a Rayleigh-Ritz method to determine the current generated by a piezoelectric energy harvester. The results showed that optimized average output power occurred for a cantilevered beam energy harvester at the natural frequency of the beam [8]. To further increase deflections and thus average power produced by the beam, a tip mass was added to increase the inertia and thus the applied moment to the beam, increasing power output. The linear model was adjusted to account for the change in rotational inertia [8].

The effect of the impedance of the circuit on the power generated by the piezoelectric energy harvester was also thoroughly investigated [6, 9-12].These investigations demonstrated the importance of matching the impedance of the circuit to the energy harvester. Initially, only resistive loads were investigated, showing how varying the real part of the circuit's impedance could affect the average power generated by the energy harvester [13]. Further research has also analyzed tuning the imaginary part of the impedance by adding a capacitor or inductors in addition to a resistor [6, 12, 14, 15].

Early energy harvesting literature has primarily focused on monolithic piezoceramic wafer such as PZT bonded to a stiff structure, such as aluminum or steel [4, 5, 13, 14, 16]. The relatively stiff nature of the piezoelectric energy harvesting material has allowed for the assumption of small-deflections for the vibrating structure to remain valid. Under these assumptions, multi-modal solutions and coupled distributed

parameter solutions have been used to solve for the fully-coupled time dependent differential equations for the cantilevered beam's position and the circuit voltage. The average output power predicted by these methods has also been experimentally verified [17].

Recently, energy harvesting research has moved beyond the linear differential equations to solving specific cases where nonlinear effects can increase the power generated. By adding a magnet to the end of the beam which interacted with other magnets nearby nonlinear beam behavior occurred that increased the bandwidth of vibration energy harvesting [18, 19]. Additionally, the effect of the nonlinear dynamics of a bistable plate on the power output of a bonded piezoelectric element have been investigated [20]. Further, the change in voltage at various levels of excitation near resonance for a cantilevered beam energy harvester has been used to investigate the nonlinearity of the electroelastic material parameters [21].

However, because of the limitations of parameters of size associated with the production of monolithic piezoceramic elements, most energy harvesting applications have been limited to power produced in the microwatt to milliwatt range due to volumetric power densities on the order of 1 microwatt/cm^3 [16, 22]. Due to the brittle nature of PZT and the high processing temperatures around 1300^oC, standard PZT sizes are limited to lengths and widths on the order of ten centimeters and thickness on the order of millimeters. Accordingly most of the recent piezoelectric energy harvesting applications have been driven by military needs for autonomous or remote sensors, micro aerial vehicles, and other micro systems where energy density – the amount of energy stored per unit volume – is the driving parameter. Much of this work has been on high frequency (100Hz to 1KHz) generators and techniques. In order to reach the level of sustained average power to charge a device such as a cellphone or laptop, vibration-driven energy harvesters on the order of 100 cubic centimeters would be needed [16]. To address the main limitations imposed by size, weight, and quantity of micro-system vibration-driven harvesters larger motion-driven harvesters and flow-driven harvesters have been proposed to potentially achieve orders of magnitude higher volumetric power

density [16]. Alternative piezoelectric materials such as the piezoelectric polymer polyvinylidene fluoride, (PVDF) and the flexible piezoelectric fiber composites (PFCs), have been also been proposed for energy harvesting applications from renewable energy sources [23].

Although the piezoelectric coupling coefficients for PVDF are an order of magnitude lower than that of traditional piezoceramics, the polymers also have much lower permittivities as seen in Table 1 below [24], which will later be shown as an advantage for energy harvesting.

Table 1: Comparison of Material Parameters for PVDF and PZT

Defined Material Metrics	PVDF	PZT	Ratio for PZT to PVDF
Charge-Stress Coupling (d_{31})	23 pC/N	190 pC/N	8.26
Relative Permittivity ($\varepsilon_{33}^T/\varepsilon_0$)	12	1700	142
Storage Modulus (Y_p)	4 GPa	61 GPa	15.3
Electromechanical Coupling (k_{31})	0.141	0.382	2.71
Specific Resistance	$8 \cdot 10^{14}$ Ωm	$8 \cdot 10^{12}$ Ωm	$1 \cdot 10^{-2}$

Accordingly, specific applications can allow for the flexibility of polymer films to harvest comparable power densities [23, 25]. One example of such an application is the EEL system developed at Princeton University. The EEL technology is designed to harness lower frequency oscillations (3Hz to 20Hz) for power production. This system exploits traveling vorticies behind a bluff body in a flow to induce undulating motion in a piezoelectric polymer similar to an eel swimming [26]. To maintain regular oscillations, the eel must lay perpendicular to the water column and parallel to current flow. Power output ranges from milliwatts to watts for sizes geometries optimized for specific current flow characteristics. A system such as this is dependent upon steady flows, such as those found in rivers or ocean areas with constant strong currents. In this

thesis we hope to define a concept that can harvest comparable amounts of energy for oscillating flows through an alternative concept design.

1.4 Problem Statement

1.4.1 Concept Design

As discussed at the start of this section, harvesting ocean waves has great promise to address some of the energy needs in the U.S. A design concept was proposed that combines the potential of piezoelectric energy harvesting technology with the vast potential of this resource to demonstrate the feasibility of efficiently harvesting electrical power. Specifically, piezoelectric artificial kelp (PAK), a concept developed at Sandia national labs (Dr. Jeffrey Martin) can convert the natural mechanical motions seen in kelp forests, due to ocean wave action, into electricity. The PAK system, as shown in Figure 2 will convert the natural mechanical motions of underwater currents caused by ocean waves into electricity. Tethered to the ocean floor and extending vertically in the water column, the PAK would undergo periodic flexure with each wave. Similar to natural mechanical motions seen in kelp forests, the PAK would convert the flexure into electricity via the direct piezoelectric effect as shown in Figure 4.

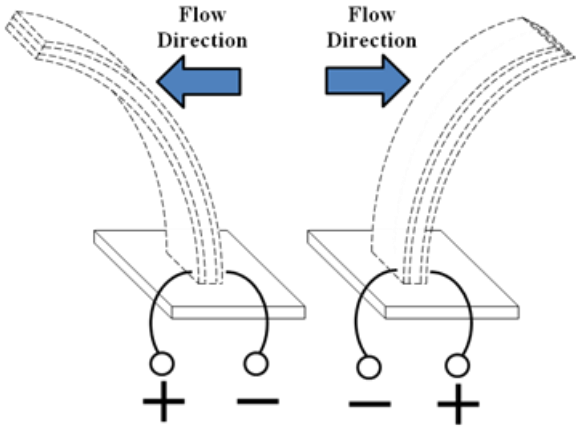

Figure 4: PAK Concept for Charge Generation

On a large power production scale, arrays of PAK ribbons could be strung together into synthetic kelp forests on the ocean floor along the coast. In contrast to most forms of hydrokinetic energy harvesting system, such as turbines and tidal harvesting, the PAK system will have no fast moving parts which would interfere with the surrounding environment. Mounted on the coastal ocean floor, the harvesters would not impede surface traffic and could potentially serve as a wildlife refuge while still producing useful power. Assuming that sufficient considerations were taken to ensure that the PAK system would not extend close enough to the ocean's surface so as to fould boat propellers, the PAK would not significantly affect boat movement. By serving as a wildlife refuge, PAK could also increase the local fish population. On a smaller scale, the devices could be used as an unobtrusive way to power underwater measurement devices that would report periodically, such as salinity or particulate monitors.

1.4.2 Selected Construction Configurations

To limit the possibility of construction configurations for comparison for the PAK, several simplifying assumptions were made. After reviewing the literature, a common method of cantilevered beam energy harvester construction is selected. Cantilevered beam energy harvesters are most commonly constructed by laminating

plies of piezoelectric material onto an inactive material substrate or directly onto one another. It was assumed that this construction created a layered beam with a cross-section that did not change with the width or length of the beam. Within this category of laminated beam harvesters, four predominant configurations are found: the homogeneous bimorph, the heterogeneous bimorph, the N-layered active beam and the unimorph.

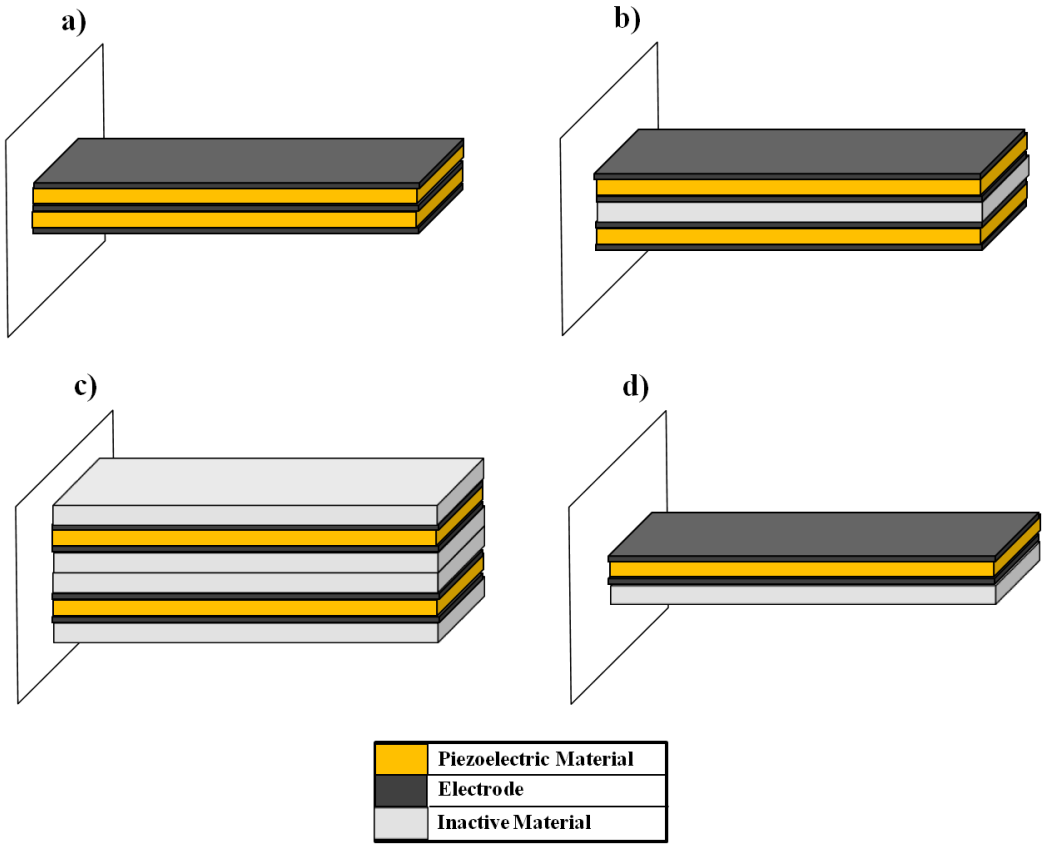

Figure 5: Common Energy Harvester Configurations.
a) Homogeneous Bimorph b) Heterogeneous Bimorph
c) N-Layered Active Beam d) Unimorph

Because the laminated harvester's construction varies only in the thickness direction of the beam, the harvester layup configuration could be fully characterized by describing the variation in the thickness direction. As shown in the previous figure, it

was assumed that electrodes covered the upper and lower surfaces of each layer of piezoelectric material and that the electrodes had a negligible thickness compared to the other materials used in the construction of the harvester. Using this convention, the homogeneous bimorph is described as two piezoelectric plies of equal thickness laminated together with an adhesive of negligible thickness, symmetric about the neutral axis of the beam, as shown in Figure 5a. The heterogeneous bimorph, also consists of two piezoelectric elements laminated to an inactive material. This single layer consisting of a ply of piezoelectric material bonded to an inactive material bonded to another piezoelectric material could represent the entirety of the heterogeneous bimorph so long as it layup is symmetric about the neutral axis of the beam, as shown in Figure 5b. However, the previously described layer could also be repeated several times through the thickness of the beam. Repeating the pattern N times creates an N-layered active laminate, as shown in Figure 5c. The final configuration represents the case where the harvester is simply constructed from an asymmetric configuration where the piezoelectric layer is bonded to an inactive material, shown in Figure 5d. To determine how these various configurations impact the power produced by the PAK, it was important to understand what materials would be used in the harvester.

1.4.3 Piezoelectric Material Choices

Using the PAK system as a test bed, the current research seeks to establish a material comparison parameter for flow-driven applications to compare how piezoelectric material choice affects the average power generated by the energy harvester. Prior to 1970, the only known piezoelectric materials were ceramics such as quartz or PZT as shown in Figure 6a, in the form of the commercially available QuickPack from Midé (Midé, Medford MA). In 1969, PVDF was discovered by Kawai to exhibit dipole polarization expanding the realm of piezoelectric materials into polymers [27], as shown in Figure 6b in the laminated film element from Measurement Specialties (MSI Inc., Hampton VA).

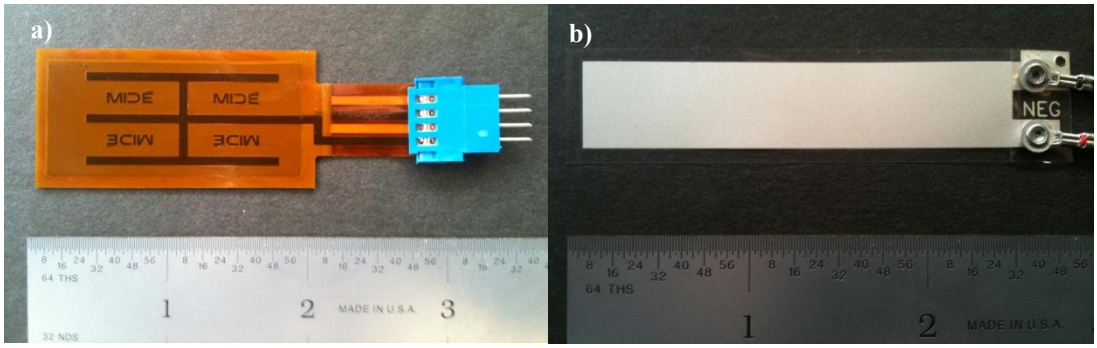

Figure 6: Piezoelectric Material Options
a) PZT QuickPack and b) PVDF Laminated Film Element

Whereas the production of traditional piezoceramic plates such as PZT is a costly and energy intensive process that results in size limitations and requires the use of lead oxide (as part of the material's composition), comparatively the production process for PVDF has a relatively low cost and energy usage. PVDF has not been previously used in energy harvesting applications because it has a piezoelectric coupling coefficient that is roughly one order of magnitude smaller than that of traditional piezoceramic elements, as previously shown in Table 1.

By assuming piezoelectric materials with isotropic mechanical properties, a simplified analysis was performed that allowed for comparison of the energy harvesting properties the most commonly used piezoceramic, PZT, with the most commonly used piezopolymer, PVDF. Similarly, the inactive materials used in the heterogeneous bimorph and unimorph configurations were assumed to be isotropic materials of arbitrary mechanical stiffnesses.

1.4.4 Scope of Analysis

To optimize the power output for the PAK harvester for a given set of ocean conditions, the effect of harvester construction configuration, physical dimensions and material choices were considered. To limit the scope of the possible construction configurations for the harvester, the research was limited to the previously described configurations commonly found in literature: homogeneous bimorph, heterogeneous

bimorph, unimorph. In the construction of these configurations, the active materials to be used in construction were limited to isotropic materials, namely, a monolithic piezoceramic, PZT, and a piezopolymer, PVDF. The inactive material used for the heterogeneous bimorph and unimoph configurations were assumed to be an isotropic material of arbitrary mechanical stiffness to be optimized by the analysis. A volumetric average power analysis established a common metric to compare the effect of the physical dimensions on the output of the harvester. Within these given constraints, the following work has determined the construction configuration and material choices that optimize the power output of the PAK for arbitrary dimensions. In doing so, the work establishes a new, experimentally validated tool for the analysis of power output by flow-driven cantilevered beam energy harvesters.

2. DETERMINATION OF AVERAGE POWER

2.1 Problem Formulation

2.1.1 Fluid-Structure Interaction

As a first step of determining the power created by the energy harvester, the dynamics and loading of the harvester were determined. The forces exerted on the harvester by the environment were determined by making several simplifying assumptions about the fluid flow and its interaction with the harvester. It was assumed that the forces on the harvester were predominantly due to underwater fluid flow. In the coastal environment underwater currents can have several different origins [28]. Because of the nature of the application, an oscillatory current flow with high flow speed and frequency was desired. Tidal currents generally have very high flow speeds, on the order of tens of centimeters per second in most areas; however because the frequency of the oscillations in tidal driven current are on the order of days, they were determined to be an unsuitable source for energy harvesting. Another source of large flow speeds, rip tides can generate underwater current speeds on the order of meters per second and have a frequency of oscillation on the order of tens of seconds being as they are caused by the interaction of surface waves with bluff bodies, typically sandbars. However, because the currents interact with the sandbar, carrying sand away and shifting the position of both the higher flow speeds and the sandbar itself, utilizing the rip tide currents generated by sandbar interaction with a stationary energy harvester would be difficult. Surface gravity waves generate oscillatory current flows underwater. Often driven by the interaction of wind with the water's surface, surface gravity waves in coastal environments have periods on the order of seconds to tens of seconds [29]. Also, the underwater currents generated by surface gravity waves can have currents magnitudes on the order of tens of centimeters per second to meters per second. Across the frequency spectrum of surface

waves, it has been shown that waves of this period have the greatest total incident energy on the coastline [30].

Linear wave theory, which assumes a sinusoidal oscillation of wave height with time, was used to modeling the underwater currents generated by surface gravity waves[31]. According to linear wave theory, the underwater current flow also varies as a function of time, total water depth, position of the measurement from the ocean floor, wave period, and vertical distance between the wave's crest and trough. The horizontal component of the velocity is taken to be:

$$u(\eta,t)=\frac{\pi H_0}{\tau}\frac{\cosh(\frac{2\pi}{L}\eta)}{\sinh\left(\frac{2\pi}{L}d\right)}\sin\left(\frac{2\pi}{\tau}t\right) \tag{10}$$

where H_0 was taken as the distance between the crest and trough of the wave, τ was the period of the wave, d was the water depth, η was the distance measured from the ocean floor, and L was taken to be the wave length, which was defined by the relation [30]:

$$L=\frac{g\tau^2}{2\pi}\tanh\left(\frac{2\pi d}{L}\right) \tag{11}$$

The force of the underwater current on the harvester was estimated to have the effect of a distributed load on the harvester in the horizontal direction only, as shown in Figure 7.

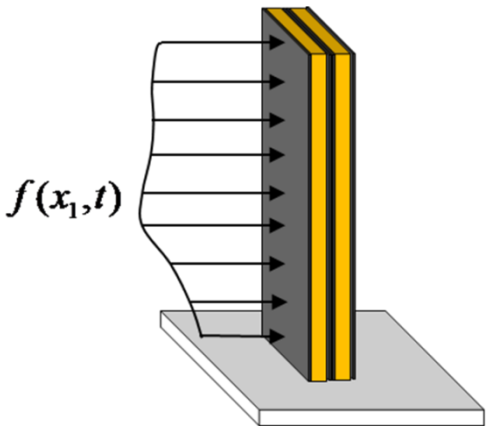

Figure 7: Distribution of Forces on Harvester

The total force applied by the current on the harvester was estimated using a simplified version of Morison's equation where the inertial effects of the harvester were ignored and the change in displacement of the harvester was considered to be negligible compared to the flow velocity. The reference area for the drag coefficient was taken to be the projected area of the harvester in the horizontal flow. Assuming that no other underwater current sources were present, the direction of the current flow according to linear wave theory was assumed to be the same at all depths.

$$F_{appl}(t) = C_d \frac{1}{2} \rho S_{ref} \frac{\int_0^l (u(\eta,t))^2 dx}{l} sign\ (u(t)) \tag{12}$$

The magnitude of the distributed load at each point along the harvester's length, in the flow was then determined to be:

$$f(\eta,t) = C_d \frac{1}{2} \rho b (u(\eta,t))^2 sign\ (u(t)) \tag{13}$$

For this particular application, the applied distributed load is:

$$f(\eta,t) = C_d \frac{1}{2} \rho b \left(\frac{\pi H_0}{\tau} \frac{\cosh(\frac{2\pi}{L}\eta)}{\sinh\left(\frac{2\pi}{L}d\right)} \sin\left(\frac{2\pi}{\tau}t\right) \right)^2 sign\left(\sin\left(\frac{2\pi}{\tau}t\right)\right) \tag{14}$$

which is of the form:

$$f \sim \sin^2\left(\frac{2\pi}{\tau}t\right) sign\left(\sin\left(\frac{2\pi}{\tau}t\right)\right) \tag{15}$$

For linear analysis of rigid harvester undergoing small deflection due to the flow, the projected area was simply calculated to be the harvester's length multiplied by its width. The drag coefficient would be determined by the specific reference area and flow conditions for the specific application.Using the derived load-moment relation for a cantilevered beam with an applied distributed load in the 3-direction, the applied moment in the beam was defined as:

$$M_{appl}\Big|_{x_1=l} - M_{appl}\Big|_{x_1=x} = -\int_x^l \int_x^l f_z \, d\eta \, dx \tag{16}$$

Using the assumed distributed load applied by the force of drag by the fluid on the harvester, and no applied moment at the free end, the moment applied to the beam by the fluid flow was found to be:

$$M_{appl}\Big|_{x_1=x} = \int_x^l \int_x^l C_d \frac{1}{2} \rho b \left(u(\eta,t)\right)^2 sign\left(u(t)\right) d\eta dx \tag{17}$$

Substituting for the fluid flow from this particular application:

$$M_{appl}\Big|_{x_1=x} = \int_x^l \int_x^l C_d \frac{1}{2} \rho b \left(\frac{\pi H_0}{\tau} \frac{\cosh(\frac{2\pi}{L}\eta)}{\sinh\left(\frac{2\pi}{L}d\right)} \sin\left(\frac{2\pi}{\tau}t\right) \right)^2 sign\left(\sin\left(\frac{2\pi}{\tau}t\right)\right) d\eta dx \tag{18}$$

2.1.2 Derivation of Equations of Equilibrium

The harvester was assumed to be approximated by a plate of width b, and length l, and a thickness h that is infinitesimal compared its width or length. A coordinate system was established for analysis of the harvester with the origin at the root of the beam located at center of the plane that contains the neutral axis and the x_1, x_2, and x_3 axes in the length, width and thickness directions of the beam respectively, as shown in Figure 8.

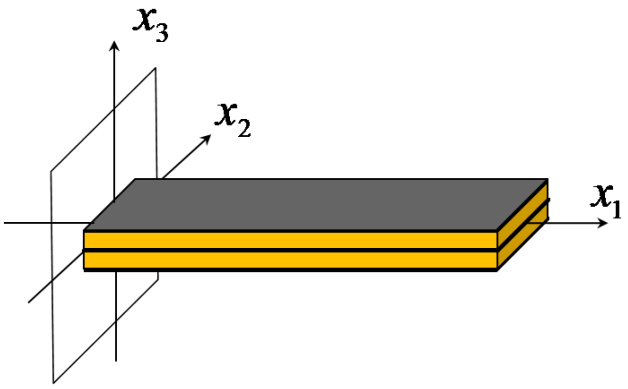

Figure 8: Definition of Coordinate System

A virtual work formulation was developed for the differential equations of conservation of linear momentum over the volume of the beam where δx_1, δx_2, and δx_3 represent the virtual displacements relative to the original configuration in the x_1,x_2, and x_3 directions respectively.

$$\int_V \left(\frac{\partial T_{11}}{\partial x_1} + \frac{\partial T_{12}}{\partial x_2} + \frac{\partial T_{13}}{\partial x_3} + f_1 \right) \delta u_1 dV = 0 \tag{19}$$

$$\int_V \left(\frac{\partial T_{12}}{\partial x_1} + \frac{\partial T_{22}}{\partial x_2} + \frac{\partial T_{23}}{\partial x_3} + f_2 \right) \delta u_2 dV = 0 \tag{20}$$

$$\int_V \left(\frac{\partial T_{13}}{\partial x_1} + \frac{\partial T_{23}}{\partial x_2} + \frac{\partial T_{33}}{\partial x_3} + f_3 \right) \delta u_3 dV = 0 \tag{21}$$

These equations assumed a quasi-static loading scenario where the effect of the inertia of any differential element is negligible compared to the body forces applied to the beam for the frequency of the oscillations experienced to the beam. Using an assumed solution for the kinematics where the beam only experiences relative displacements due to bending about the x_2-axis, the harvester experiences a local change in bending angle in, $\boldsymbol{\theta}$, which when multiplied by the distance from the neutral axis, results in:

$$u_1 = -\overline{x_3}\theta, u_2 = 0, u_3 = u_3(x_1) \text{ where } \theta = \frac{du_3}{dx_1} \tag{22}$$

Substituting the variational forms of the displacements with the assumed kinematics, the virtual work equations simplify to:

$$\int_V \left(\frac{\partial T_{11}}{\partial x_1} + \frac{\partial T_{12}}{\partial x_2} + \frac{\partial T_{13}}{\partial x_3} + f_1 \right) \left(-\overline{x_3} \delta \frac{du_3}{dx_1} \right) dV = 0 \tag{23}$$

$$\int_V \left(\frac{\partial T_{13}}{\partial x_1} + \frac{\partial T_{23}}{\partial x_2} + \frac{\partial T_{33}}{\partial x_3} + f_3 \right) \delta u_3 dV = 0 \tag{24}$$

A transverse loading case with a distributed load, f_3, was assumed where the shear forces in the x_1-x_2 plane, and that the shear forces in the x_1-x_3 plane, and the normal stress in the x_3 direction are relatively small compared to the axial stress induced by the loading. The resultant equations reduced to:

$$\int_V \left(\frac{\partial T_{11}}{\partial x_1} + \frac{\partial T_{13}}{\partial x_3} \right) \left(-\overline{x_3} \delta \frac{du_3}{dx_1} \right) dxdydz = 0 \tag{25}$$

$$\int_V \left(\frac{\partial T_{13}}{\partial x_1} + f_3 \right) \delta u_3 dxdydz = 0 \tag{26}$$

Assuming arbitrary virtual displacements allows for separation of the individual integrands into separate integrals. Assuming that the construction of the harvester does not change over the length or width of the harvester, the integration simplified the equations:

$$\frac{d}{dx_1} b \int T_{11} \overline{x_3} dx_3 + b \int \frac{\partial T_{13}}{\partial x_3} \overline{x_3} dx_3 = 0 \tag{27}$$

$$\frac{d}{dx_1} b \int T_{13} dx_3 + b \int f_3 dx_3 = 0 \tag{28}$$

Given no applied shear loading on the top or bottom of the plate:

$$\int_V \left(\frac{\partial T_{13}}{\partial x_1} + f_3 \right) \delta u_3 dxdydz = 0 \tag{29}$$

The internal moment and shear due to stresses at each cross section in the beam are defined to be:

$$M_{\text{int.}} = b \int T_{11} \overline{x_3} dx_3 \tag{30}$$

$$Q = b \int T_{13} dx_3 \tag{31}$$

$$\overline{f_3} = \int f_3 dx_3 \tag{32}$$

Then the equations of equilibrium take the form of the Euler-Bernoulli beam formulation:

$$\frac{dM_{\text{int}}}{dx_1} - Q = 0 \tag{33}$$

$$\frac{dQ}{dx_1} + \overline{f_3} = 0 \tag{34}$$

The above equations were then combined into one governing equation to be solved for each cross section along the harvester, assuming that the magnitude of the distributed load does not vary in the x_1 direction:

$$\frac{dM_{\text{int}}}{dx_1} + \int_{x_1}^{l} \overline{f_3} d\eta = 0 \tag{35}$$

Or the moment at any point, s, along the length of the beam can be found by:

$$M_{\text{int}}\Big|_{x_1=l} - M_{\text{int}}\Big|_{x_1=s} = -\int_s^l \int_s^l \overline{f_3} dx_1 dx_1 \tag{36}$$

2.1.3 Electromechanical Conversion

Next, the stresses in the beam were related to the properties for both the active and inactive materials. According to the previously derived piezoelectric coupling equations, the stress induced in differential piezoelectric element can be found by knowing its strain and piezoelectric field. The Euler-Bernoulli beam equation previously derived showed a uniaxial stress state where it was shown that the governing equation of balance of linear momentum could be fully conserved knowing only the applied moment on the beam and the normal stress in the 1 direction, T_{11}. For a piezoelectric element it was shown that:

$$T_1 = c_{11} S_1 + e_{31} E_3 \tag{6}$$

The stress in an inactive isotropic material is similarly defined knowing the Young's Modulus of the material:

$$T_1 = YS_1 \tag{37}$$

From the assumed kinematics, the local relative displacement in the 1-direction was assumed to be a function of the distance in the 3-direction from the neutral axis, and the local angle of deflection:

$$u = -\overline{x_3}\theta \tag{38}$$

Assuming infinitesimal strain, the resultant strain was determined by:

$$S_1 = \frac{du_1}{dx_1} = -\overline{x_3}\frac{d\theta}{dx_1} \tag{39}$$

where the local change in curvature of the beam, **κ**, is defined by:

$$\kappa = \frac{d\theta}{dx_1} \tag{40}$$

Thus we defined the strain in the material to be:

$$S_1 = (x_3 - x_3^*)\frac{d\theta}{dx_1} \tag{41}$$

where x_3^* is the location of the neutral axis. Through the result previously derived through the equations of equilibrium the externally applied moment due to the fluid flow is balanced by the internal stresses:

$$M_{\text{int}} = b\int T_{11}\overline{x_3}dx_3 \tag{42}$$

By substituting the constitutive equations for the material properties, and the previously derived relationship between the normal stress in the 1-direction and the internal moment, a lumped parameter model of the following form can be derived for each specific beam construction:

$$M_{\text{int}} = \Sigma YI\kappa + \Omega V \tag{43}$$

This equation, which was derived using the piezoelectric material constitutive relation and the differential equations of equilibrium, represents the balance of bending moments within the beam and represents the first of two coupled equations describing the system. The moment-curvature coupling, ΣYI, is also known as D_{11} in plate theory and the moment-voltage coupling is dependent upon both construction and connection pattern of piezoelectric layers. The voltage applied to the harvester was related to the voltage of each piezoelectric layer through the connection pattern. It was assumed that the piezoelectric material layers extended the entire length and width of the beam and each layer had an electrode of negligible thickness on its top and bottom surface. The thickness of each piezoelectric layer was assumed to be uniform with respect to the width and length of the beam, allowing the electrical field to be approximated by:

$$E_3 = -\frac{V_{layer}}{t_{p_{layer}}} \tag{44}$$

2.1.4 Electrical Circuit

The charge displaced by each piezoelectric element was found by integrating the charge displacement over the length and width of the beam.

$$Q_{layer} = \frac{1}{t_{p_{layer}}} \int_{t_{p,low}}^{t_{p,high}} \int_0^l \int_0^b \left[e_{31} S_1 + \varepsilon_{33}^S E_3 \right] dx_1 dx_2 dx_3 \tag{45}$$

Each piezoelectric layer was assumed to displace charge equal to its average state of strain. Because the strain was assumed to vary linearly through the thickness of the beam, the average state of strain was evaluated by evaluating the strain at the midpoint of each layer with respect to the thickness.

$$Q_{layer} = \int_0^l \int_0^b \left[e_{31} \overline{x_{3_{mid}}} \kappa + \varepsilon_{33}^S E_3 \right] dx_1 dx_2 \tag{46}$$

For an energy harvester with piezoelectric layers connected in parallel, the voltage was the same for each layer and the charge displaced by each layer was additively combined in accordance with conservation of charge. For an energy harvester with piezoelectric layers connected in series, the total charge displaced was the average of all of the layers and the voltage for each layer was additively combined.

The power generated by the harvester, P, was defined by the following relation, where I represents the current flow from the positive to negative terminal of the harvester and V represents the voltage across the harvester.

$$P = IV \tag{47}$$

If the harvester were connected to a closed circuit of no impedance, then current would flow from the positive to negative terminal, but no voltage drop would be experienced and no power would be produced by the harvester. Similarly if the harvester were connected to an open circuit of infinite impedance, then it would generate a potential difference across the terminals, but no current would flow. Accordingly an electrical circuit of non-zero finite impedance must be connected to the energy harvester in order to capture power.

It has been well noted in literature that the electrical impedance introduced to the system by attaching a circuit affects the power generated by the energy harvester [8]. The charge generated by the direct piezoelectric effect interacts with the impedance to generate a potential across the impedance. Also the potential across the impedance is also experienced by the energy harvester through the indirect piezoelectric effect, which has also been called the piezo back-coupling effect [17]. It has been shown that despite this coupling, usable power can be derived from a piezoelectric energy harvester. Sodano et. al showed how this circuit can be used to harvest electrical power from a piezoelectric energy harvester to charge a battery [4].

A commonly used circuit noted in literature for generating and storing power from a piezoelectric energy harvester connects the harvester to a full-bridge diode rectifier circuit and a large smoothing capacitor to store energy in a battery, as shown in Figure 9.

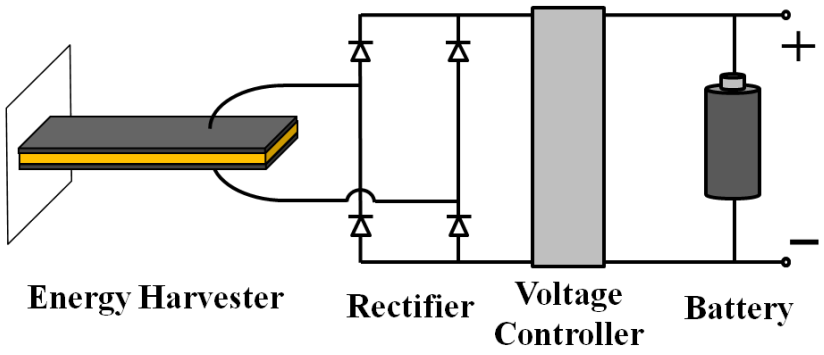

Figure 9: Reference Energy Harvesting Circuit Configuration

A significant effort has been made recently to create an energy harvesting circuit that can optimize the effective electrical impedance for a given energy harvester, thereby optimizing the power produced by the harvester while minimizing the power required to control the impedance. Ottman et. al analyzed a circuit that used a discontinuous step-down converter to optimize the average power charging a battery [6]. For the optimization technique used by Ottman et. al, the average power stored was expressed in

terms of the magnitude of the current generated by the harvester, I_p, the angular frequency of the periodic current source, ω, and the capacitance of the harvester, C_p:

$$\langle P \rangle\Big|_{opt} = \frac{I_p^{\,2}}{2\pi\omega_{circ} C_p} \tag{48}$$

Using the definition of current generated by charge displacement:

$$i(t) = \frac{\mathrm{dQ}}{dt} \tag{49}$$

In Ottman's analysis, the reference circuit used a sinusoidal input current. Thus the optimized output equation could be rewritten in terms of the magnitude of the charge displacement using the relation:

$$I_p = Q_p \omega_{circ} \tag{50}$$

Thus the average power generated by an energy harvester for the reference circuit can be expressed as:

$$\langle P \rangle\Big|_{opt} = \frac{\omega_{circ} Q_p^{\,2}}{2\pi C_p} = \frac{Q_p^{\,2}}{\tau_{circ} C_p} \tag{51}$$

The goal of the impedance matching for the application was to define a relatively simple circuit that could be easily analyzed so that an optimized power equation of the same form as the previous equation could be written. The resultant average power for the simplified circuit analysis could then be related to the average power of the reference circuit using a simple scalar multiple. A simple load resistor of an unknown magnitude was chosen for simplified analysis in this circuit. The energy harvester was connected in series with the load resistor, shown in Figure 10.

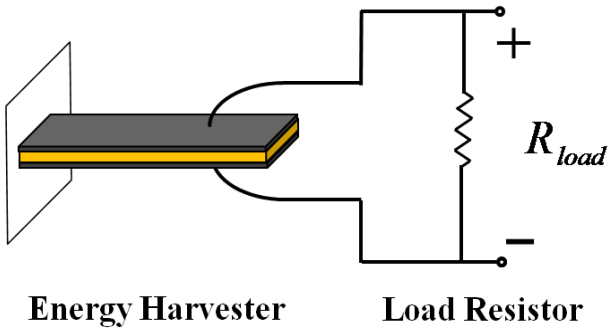

Figure 10: Resistor Only Energy Harvesting Circuit

The voltage generated by the energy harvester is then simply written using the equation for conservation of charge.

$$\frac{V(t)}{R} = i(t) \tag{52}$$

The current generated by the harvester is determined by taking the derivative of the previously defined charge displacement:

$$i(t) = \frac{dQ}{dt} = \frac{d}{dt}\int_0^l \int_0^b \left[e_{31} \bar{z}_{mid} \kappa + \varepsilon_{33}^S E_3 \right] dxdy \tag{53}$$

The current generated by the harvester is grouped according to the parameters that are dependent upon the strain experienced by the harvester and the voltage across the electrodes of the harvester, resulting in the following parameters.

$$\frac{V(t)}{R_{tot}} + C_p \frac{dV(t)}{dt} = \frac{dQ(t)}{dt} \tag{54}$$

This equation, which was derived using the conservation of charge produced by the energy harvester and the second constitutive equation of piezoelectric materials, represents the second of the two coupled equations that describe the system. From a circuit analysis standpoint, the piezoelectric energy harvesting circuit used to investigate the loading scenario for the given application will be approximated by a current source, capacitor, the internal resistance of the piezoelectric layers and load resistor in parallel, as shown in Figure 11.

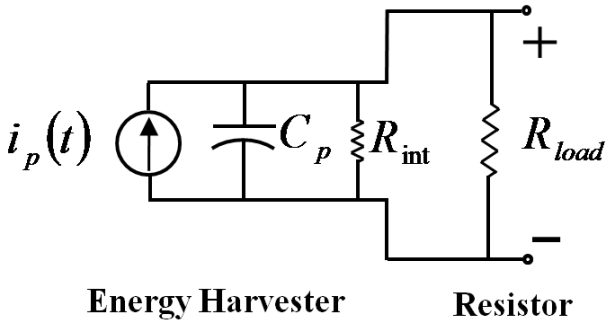

Figure 11: Assumed Equivalent Circuit

2.2 Small Deflection Average Power Optimization

2.2.1 Simplification Assumptions

The two, coupled equations were first solved for the given system by assuming small deflection of the beam. The curvature for a beam in the original coordinate was written as:

$$\kappa = \frac{-\frac{d^2 x_3}{dx_1^2}}{\left(1+\left(\frac{dx_3}{dx_1}\right)^2\right)^{3/2}} \tag{55}$$

By assuming small deflections, the change in the deflection x_3 is assumed to remain constant with respect to the distance in the x_1 direction. Additionally, the projected length of the beam in the original coordinate system could be approximated by the original length of the beam. Thus, the integrated moment over the length of the beam was then defined as:

$$\int_0^l M_{appl}\, dx_1 = \int_0^l \int_x^l \int_x^l C_d \frac{1}{2}\rho b \left(\frac{\pi H_0}{\tau} \frac{\cosh(\frac{2\pi}{L}\eta)}{\sinh\left(\frac{2\pi}{L}d\right)} \sin\left(\frac{2\pi}{\tau}t\right) \right)^2 sign\left(\sin\left(\frac{2\pi}{\tau}t\right)\right) d\eta\, dx\, dx \tag{56}$$

Assuming small deflections so that the length of the beam did not vary with time, the time dependent variables can be separated and the integrated moment was written as:

$$\int_0^l M_{appl}\, dx_1 = \psi \left(\sin\left(\frac{2\pi}{\tau} t \right) \right)^2 sign\left(\sin\left(\frac{2\pi}{\tau} t \right) \right) \tag{57}$$

Using the constitutive equation for the material to find the charge generated by the electrode and the first governing equation, the charge generated by each piezoelectric layer can be written. By assuming that the voltage remains constant over the length and width of the beam:

$$\begin{aligned} Q_{layer} &= \frac{e_{31}\overline{x_{3_{mid}}}}{\Sigma YI} b \int_0^l M_{appl.}(x_1) dx_1 \left(\sin\left(\frac{2\pi}{\tau} t \right) \right)^2 sign\left(\sin\left(\frac{2\pi}{\tau} t \right) \right) \\ &- \left(\varepsilon_{33}^S + \frac{e_{31}\overline{x_{3_{mid}}}\,\Omega}{\Sigma YI} \right) \frac{bl}{t_{p_{layer}}} V \end{aligned} \tag{58}$$

The parameters can then be grouped in the following form:

$$Q_{layer} = Q_p \left(\sin\left(\frac{2\pi}{\tau} t \right) \right)^2 sign\left(\sin\left(\frac{2\pi}{\tau} t \right) \right) - C_p V \tag{59}$$

These common terms can be used for the linear analysis of the circuit for optimization using the previously mentioned second governing differential equation.

$$\frac{V(t)}{R_{tot}} + C_p \frac{dV(t)}{dt} = \frac{dQ(t)}{dt} \tag{60}$$

2.2.2 Optimization of Load Resistance

Conventionally, in cantilevered beam piezoelectric energy harvesting analysis, the vibration and thus deflection of the beam is taken to be small and expressed in a series of normalized eigenfunctions representing the bending mode for each natural frequency of the beam. Optimization of circuit parameters is performed via complex analysis by assuming a linear system with harmonic input displacements or forces, harmonic deflection response, and harmonic output voltage response of the form:

$$f \sim Ae^{j\omega t} \tag{61}$$

These assumptions allow the analysis and optimization of circuit parameters in the frequency domain rather than the time domain. However, for the given application, as shown in equation distributed load equation below, the forcing function for the current system was not harmonic, but was assumed to be a smooth, periodic function of the form:

$$f \sim \sin^2\left(\frac{2\pi}{\tau}t\right) sign\left(\sin\left(\frac{2\pi}{\tau}t\right)\right) \tag{62}$$

For small deflections resulting in linear geometric equations, it has been shown that through the electromechanical coupling of the piezoelectric element, the charge generated by the piezoelectric element was of the following form, shown in Figure 12. The resultant current generated is shown in Figure 13.

$$Q = Q_p \sin^2\left(\frac{2\pi}{\tau}t\right) sign\left(\sin\left(\frac{2\pi}{\tau}t\right)\right) \tag{63}$$

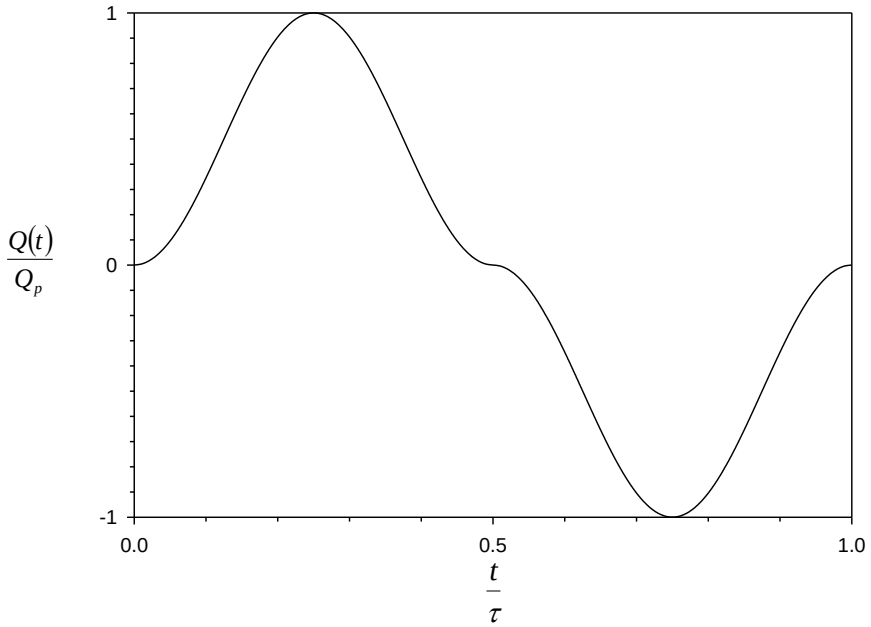

Figure 12: Charge Displaced Versus Time

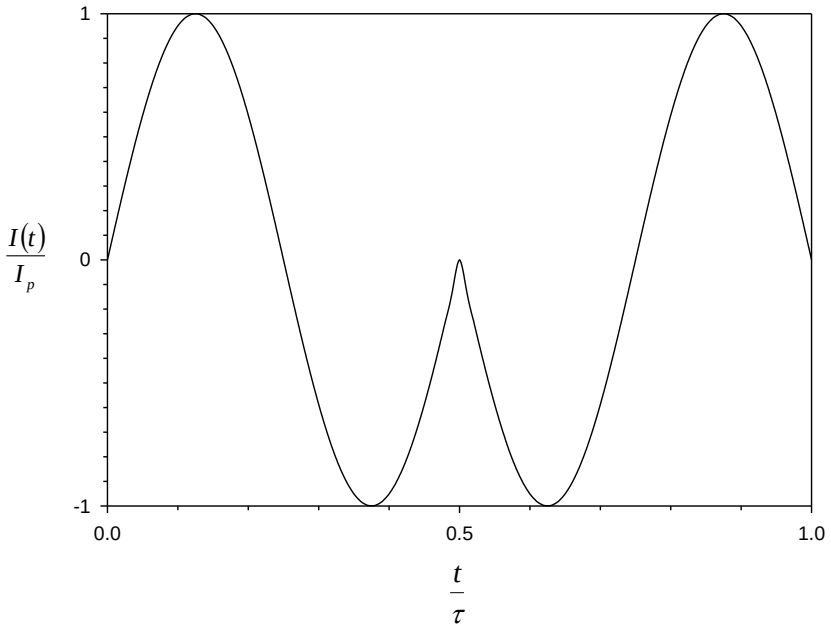

Figure 13: Current Versus Time

The form of the current with respect to time was used to solve the second governing differential equation analytically.

$$V(t) = \left(\int \frac{i(t) e^{\frac{t}{R_{tot} C_p}}}{C_p} dt + const \right) e^{\frac{-t}{R_{tot} C_p}} \tag{64}$$

Using integration by parts, the integral was simplified to be of the form:

$$\int i(t) e^{\frac{t}{RC}} dt = \int \frac{dQ}{dt} e^{\frac{t}{RC}} dt = Q(t) e^{\frac{t}{RC}} - \int Q e^{\frac{t}{RC}} dt \tag{65}$$

Then the voltage simplifies to become:

$$V(t) = \left(Q(t) e^{\frac{t}{RC}} - \int Q(t) e^{\frac{t}{RC}} dt + const \right) e^{\frac{-t}{R_{tot} C_p}} \tag{66}$$

Because the form of the charge displaced by the energy harvester is periodic, and the system is assumed to be in steady-state the analysis of the time domain can be confined to a single interval. The charge was then written in piecewise form to allow for

analytic analysis over the single interval, which then resulted in a piecewise solution for the voltage.

$$Q(t) = \sin^2\left(\frac{2\pi}{\tau}t\right) sign\left(\sin\left(\frac{2\pi}{\tau}t\right)\right) = \begin{cases} \sin^2\left(\frac{2\pi}{\tau}t\right) & \text{for } t = \left[0, \tau/2\right] \\ -\sin^2\left(\frac{2\pi}{\tau}t\right) & \text{for } t = \left[0, \tau/2\right] \end{cases} \tag{67}$$

The only integral in the formulation of voltage was then solved exactly as:

$$\int Q(t) e^{\frac{t}{RC}} dt = Q_p e^{\frac{t}{R_{tot} C_p}} \left(\frac{16\pi^2 C_p^2 R_{tot}^2 - 4\pi C_p R_{tot} \sin\left(\frac{4\pi}{\tau}t\right) - \tau^2 \cos\left(\frac{4\pi}{\tau}t\right) + \tau^2}{32\pi^2 C_p^2 R_{tot}^2 + \tau^2} \right) \tag{68}$$

The constant of integration in the voltage formulation was then solved by assuming a periodic boundary condition that:

$$V(t = 0) = V(t = \tau) \tag{69}$$

Because of the previous assumption about the circuit, the internal resistance of the piezoelectric energy harvester and the load resistance were identified to be in parallel with one another. Thus the inverse of the total resistance was written as the sum of the inverses of the internal and load resistances.

$$\frac{1}{R_{tot}} = \frac{1}{R_{\text{int}}} + \frac{1}{R_{load}} \tag{70}$$

The power dissipated across the load resistance in the circuit at any point in time was then defined by:

$$P(t) = \frac{V^2}{R_{load}} \tag{71}$$

The power was then averaged over the period by using the fundamental theorem of calculus.

$$\langle P \rangle = \frac{1}{\tau} \int_0^{\tau} P(t) dt \tag{72}$$

Terms within the average power equation were then rearranged to allow for the identification of two dimensionless ratios of parameters:

$$r_1 = \frac{\tau}{R_{\text{int}} C_p}, r_2 = \frac{R_{\text{int}}}{R_{load}} \tag{73}$$

The average power dissipated across the load resistor was then written as:

$$\langle P \rangle = \frac{Q_p^{\,2}}{\tau C_p} f(r_1, r_2) \tag{74}$$

For any measured time constant r_1, a resistance ratio, r_2, could be defined that would optimize the average power dissipated across the load resistor. The resultant range of the function, f, for all r_1 and r_2 is found in Figure 14.

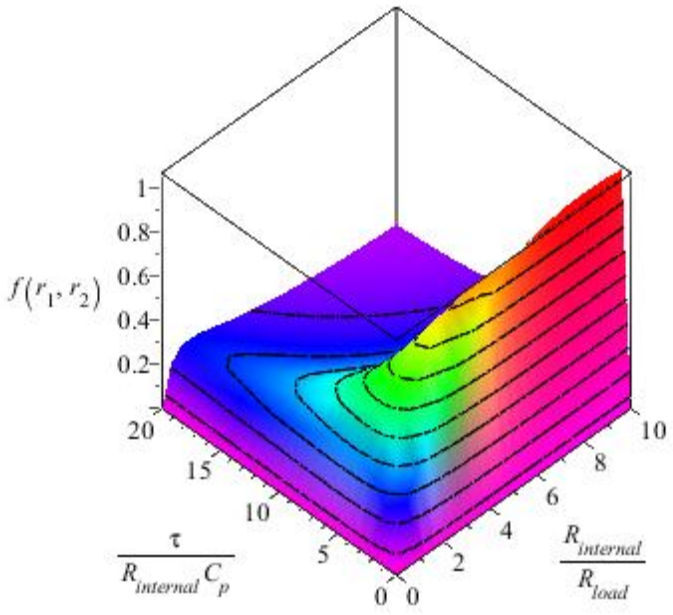

Figure 14: Power Output across Load Resistor as a Function of Circuit Parameters

For a specific period and measured internal resistance and capacitance, a ratio between the internal resistance and load resistance exist that maximizes the output power. The power is maximized for cases where the time constant is much less than 10. A particular case where $r_1=5.2\text{x}10^{-6}$ is displayed in Figure 15.

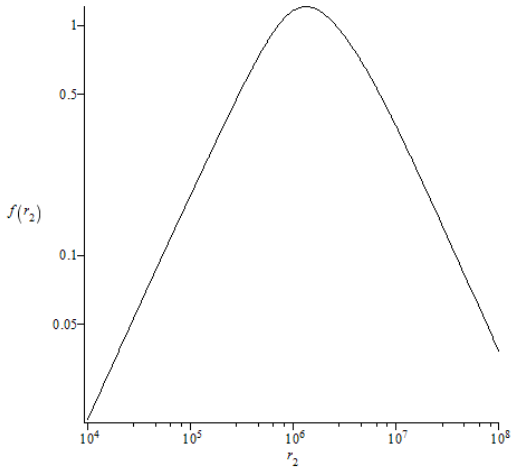

Figure 15: Sample Power Optimization across Load Resistor

For a time constants relevant to the application (much less than ten and greater than zero) then average power dissipated across the optimal load resistor is found to be:

$$\left\langle \hat{P} \right\rangle \approx 1.208 \frac{Q_p^{\ 2}}{\tau C_p} \tag{75}$$

Converting the optimized average power from the reference circuit from Ottman et. al to a similar format results in:

$$\left\langle \hat{P} \right\rangle = \frac{Q_p^{\ 2}}{\tau C_p} \tag{76}$$

Thus the power generated across the load resistor could be related to the reference circuit by a scalar value. The potential expected to be generated by the harvester was approximated using the previously mentioned piecewise equation and is periodic and of the same period as the loading. An example of the form that was expected from the resultant analysis with a charge displacement amplitude and capacitance on the order of that expected for the relevant application is shown below in Figure 16.

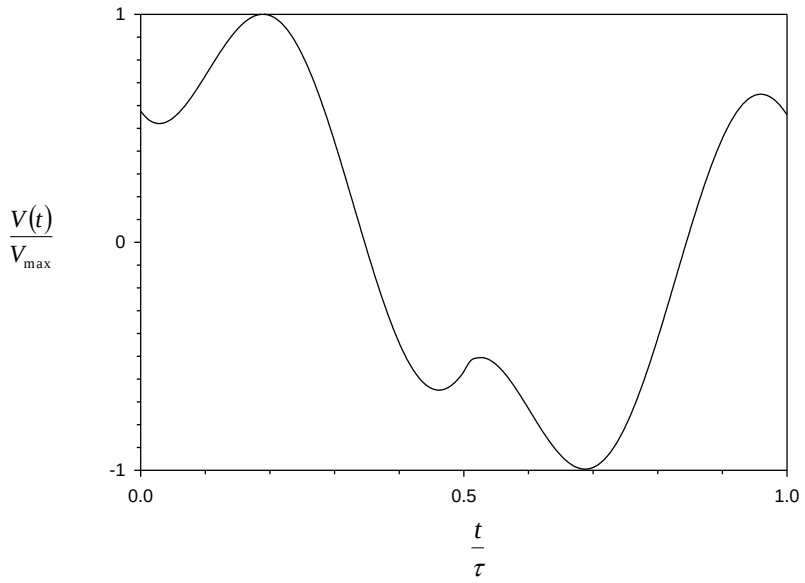

Figure 16: Sample Piecewise Voltage for One Period
(τ=1 sec, Q_p=6x10^{-8} C, C_p=12x10^{-8} F/m and R=1.5 MΩ)

2.3 Experimental Validation of Linear Analysis

2.3.1 Experimental Setup Description

Following the analytic optimization and comparison of the various energy harvesting configurations and piezoelectric material choices, a method was sought to validate the analysis. For ease of construction of the experimental validation setup, it was desired to use preconstructed harvesters from commercially available prepackaged piezoelectric elements that could be combined to create an effective piezoelectric energy harvester. As a prepackaged material option, the QP20n QuickPack harvester from Mide Corporation, previously depicted in Figure 4a, was chosen. Constructed using two piezoelectric layers of PZT and bonded together using epoxy, the QuickPack resembled the 2-layer heterogeneous bimorph energy harvester with the inactive material as epoxy. The measured beam dimensions and material parameters from the QuickPack data sheet are listed below in Table 2.

Table 2: QuickPack Construction and Material Parameters

Parameter	Value
Beam Length (l)	48.4 mm
Beam Width (b)	25.4 mm
Beam Thickness (h)	696 μm
Total Active Material Thickness (t_p)	508 μm
Number of Active Material Layers	2
Construction Configuration	Two-Layer Heterogeneous Bimorph
Active Material	PZT
Inactive Material	Epoxy (Y_i = 4.5 GPa)
Connection Pattern	Parallel

Several plans were considered for simulating proportional loading for the energy harvester for the given application. Although several initial plans involved simply loading the beam and measuring the resultant potential generated across an open circuit potential, such experimental setups would prevent the accurate measurement of the effective adjustment of the piezoelectric capacitance due to piezoelectric back-coupling. A constant periodic force on the same order of magnitude of frequency and scale was needed to accurately characterize the magnitude of the effective piezoelectric capacitance as well as the amplitude of the charge displacement.

A wave tank with a water depth on the order of the length of commercially available pre-packaged piezoelectric elements was sought for the purpose of providing periodic loading via wave action, similar to that expected in the given application. A wooden wave tank 16 feet in length, 4 feet in width, and 9 inches deep was provided for use by Dr. Randall from Texas A&M University in the Ocean Engineering Department, as shown in Figure 17.

Figure 17: Wave Tank Used for Experimental Testing

The waves in the wave tank were driven by a variable speed electric motor connected to plunger, shown in Figure 18, which was used to generate periodic waves of steady amplitude.

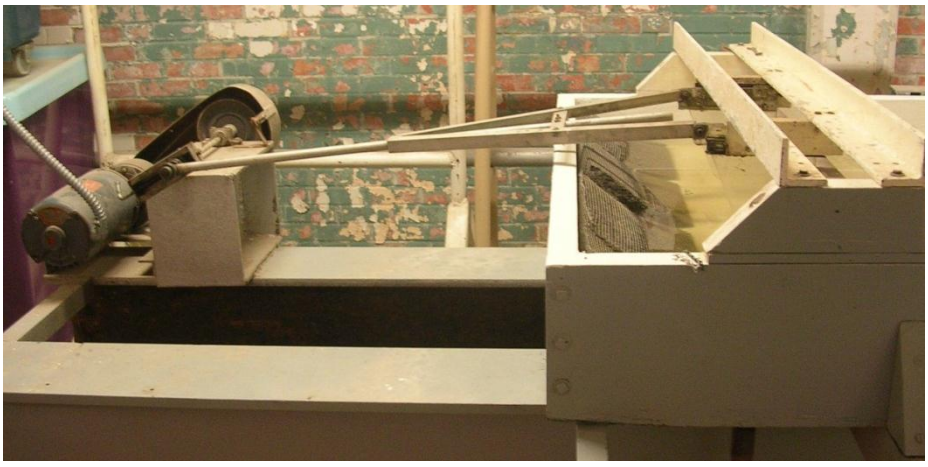

Figure 18: Wave Action Driving Mechanism

However, because the wave tank was constructed from wood and had not been used in the past decade cracks in the wood prevented the wave tank from holding water at a consistent level. Because the magnitude of the loading on the harvester was dependent upon the wave height and wave length and thus water depth, the wave tank was renovated to prevent the water level from decreasing during the experiments, several images from the wave tank renovation process can be found in Appendix A. The wave tank was sanded, caulked, painted and re-caulked to minimize the water loss that would occur during experimentation.

In the PAK harvester concept, the harvesters are anchored by a substructure on the ocean floor. A clamp device was needed to secure the harvester to the bottom of the wave tank without penetrating the waterproof paint lining the bottom of the wave tank. The resultant concept involved using a clamp welded to a heavy metal plate to anchor the harvester to the bottom of the tank without moving. The model of the installed device is shown below with a close-up of the assembly is shown in Figure 19.

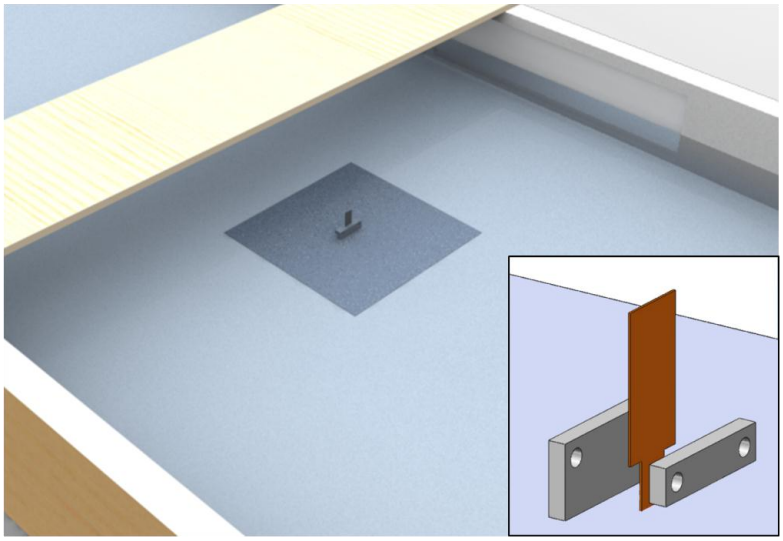

Figure 19: To-Scale Model of Experimental Setup with Close-Up of Clamp Assembly

2.3.2 Loading Measurement Description

It was necessary to have a force measurement device located in the water to calibrate the magnitude of the loading experienced by the energy harvester. Although the linear wave theory described the flow conditions in the wave tank through the wave height, wave period and water depth, the relationship between the flow conditions and the resultant moment induced on the harvester also needed to be determined. The moment induced on the harvester was measured by using a strain gage attached to a cantilevered beam constructed on inactive material. The clamp design was altered to include a second clamp for the inactive cantilevered beam with the strain gage, as seen in Figure 20. The inactive beam was a homogeneous beam composed of an isotropic polymer, while the harvester was a heterogeneous bimorph consisting of epoxy and PZT. Still, the assumption was made that for the low loading conditions that both the inactive beam and the harvester would experience small deflections, resulting in the same loading conditions.

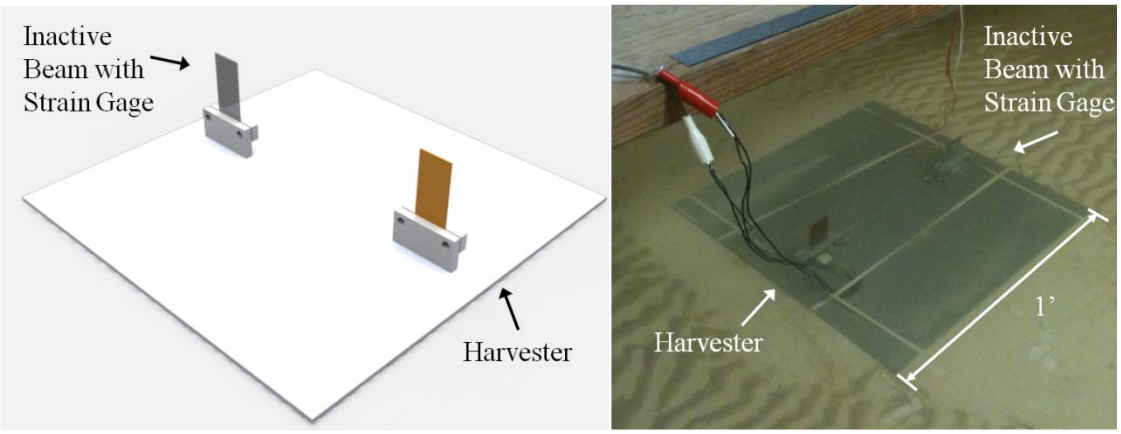

Figure 20: Final Model of Clamp Setup (left) and Installed Setup (right)

2.3.3 Testing Procedure and Conditions

By constructing an inactive beam of the same width and length as the energy harvester, to be used in the same flow conditions, it was assumed that both the beam

with the strain gage and the harvester would experience the same forces. The strain gage on the harvester was connected in a quarter-bridge formation which was then connected to a data acquisition device. The respective voltages were connected via breadboard and connector block to a National Instruments PCI-6040e Multifunction DAQ which was installed into a Desktop PC where the signals were digitally recorded and analyzed using SignalExpress. The entire data acquisition setup is shown in Figure 21.

Figure 21: Data Acquisition Setup

The relation between the applied moment and voltage across the strain gage bridge was measured was calibrated directly with the inactive beam installed in the clamp. The harvester was mounted in the clamp configuration to the side of the wave tank and the voltage was measured across the strain gage bridge for several different proof masses were hung from the end of the cantilevered beam. The results for the moment-voltage relation were fit with a linear regression curve with a coefficient of determination of R^2=0.9987. The results from the calibration were shown in Figure 22.

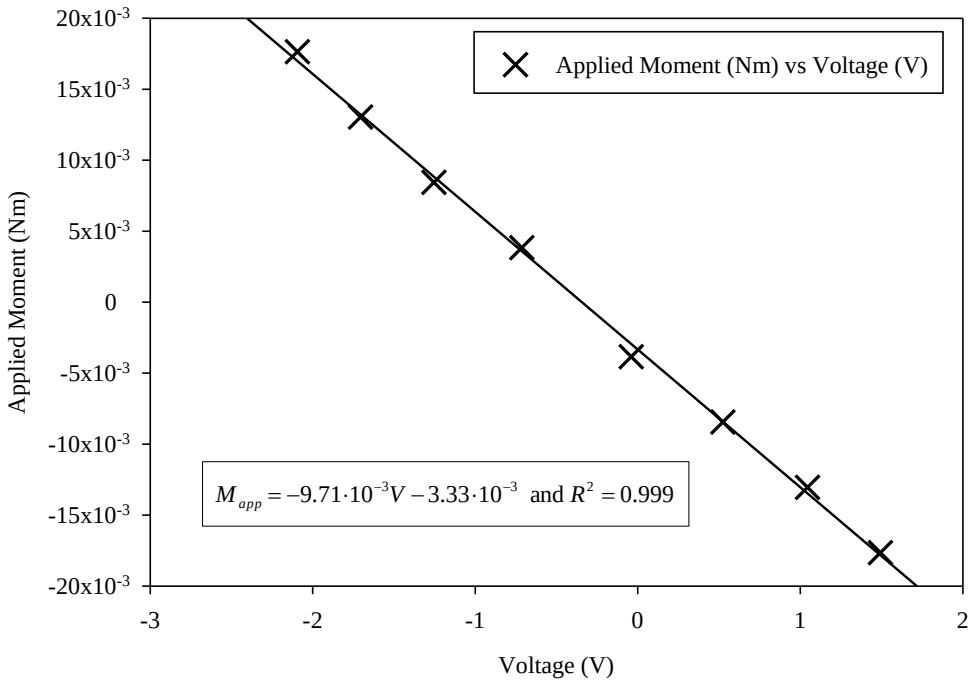

Figure 22: Sample Strain Gage Calibration Data

The calibrated inactive beam with strain gage and the QuickPack were waterproofed, and completely submerged in the wave tank. The setup was oriented so that the direction of bending would coincide with the direction of wave propagation.

The wave generator was adjusted so that wave period was on the order of one second, and the wave height would be small enough to vary sinusoidally with time, in accordance with linear wave theory. The resultant water depth, wave trough to crest distance, and wave period were recorded. The wave length and maximum flow speed were calculated using the previously defined relation from linear wave theory and were also tabulated in Table 3.

Table 3: Summary of Flow Parameters

Parameter	Value
Water Depth (d)	0.137 m
Wave Crest-Trough Distance (H)	0.041 m
Wave Period (τ)	1.01 sec
Calculated Wavelength (L)	1.07 m
Calculated Depth-Averaged Maximum Flow Speed (u_{max})	0.16 m/s

2.4 Large Deflection Solution Formulation

As previously discussed in the linear analysis, the volumetric power is proportional to the fourth power of the length and the inverse of the fourth power of the thickness of the energy harvester. Additionally, PVDF, which can be mass produced and has a higher power volumetric average power output than PZT has an order of magnitude lower stiffness than PZT. For small deflections, it was assumed that the projected beam length in the flow could be approximated by the original length of the beam. However the design concept includes long, thin beam possibly constructed using compliant polymers. Clearly the small deflection would not remain valid for the relatively large loading expected from the design concept. The integral of the applied moment over the projected length of the beam in the flow can be over-approximated using the assumption that the original length in the flow is equal to the projected length of the beam in the flow. Thus optimizing the average power for the PAK for all material and construction parameter involves extending analysis of the PAK harvester to large deflections.

In small deflection assumptions, the curvature of the beam was assumed to be constant with respect to the x_1 direction. For large deflections, the curvature of the beam must be approximated with a higher order function. For the purposes of this analysis, a new coordinate, s, was defined, denoting the arc length along the beam, as shown in Figure 23.

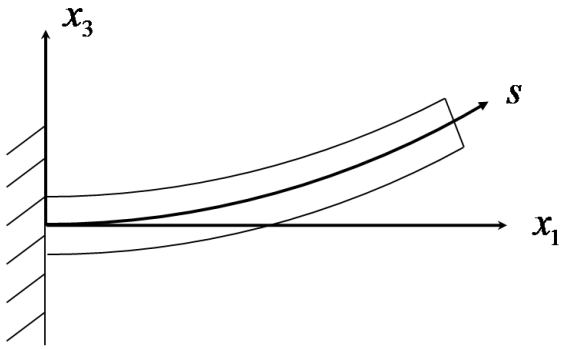

Figure 23: Description of Curvilinear Coordinate System

The local change in angle of the beam was then defined to be a polynomial function of the arc length position along the beam nondimensionalized by the length of the beam, in accordance with the method established by Dado et al. [32].

$$\theta(\bar{s}) = \sum_{i=0}^{N} a_i (\bar{s})^i \quad \text{where} \quad \bar{s} = \frac{s}{l} \tag{77}$$

Then the curvature of the beam at each point alnong the arc length was defined as:

$$\kappa(\bar{s}) = \frac{d\theta}{d\bar{s}} = \sum_{i=0}^{N} i a_i (\bar{s})^{i-1} \tag{78}$$

Using the newly defined kinematics for the curvature of the beam, the moment balance at each point along the arc length of the beam was defined by the first governing equation.

$$\sum YI\kappa + \Omega V - M_{appl}(\bar{s}) = 0 \tag{79}$$

In accordance with the method previously, described, a residual error in the moment balance over a differential element along the arc length was established. Because the voltage was assumed to remain constant over the length of the beam, the change in moment induced in the beam by the voltage over a differential section of the arc length was assumed to be zero. Thus the linear piezoelectric effect did not directly impact the formulation for the residual of the moment and the residual error of moment balance was identified as:

$$e(\bar{s}) = \sum YI \frac{d^2\theta}{d\bar{s}^2} + \frac{d\sum YI}{d\bar{s}} \frac{d\theta}{d\bar{s}} - \frac{dM_{appl}}{d\bar{s}} \tag{80}$$

For the case of this study, where the cross section of the beam did not change with respect to the arc length position of the beam, and the only applied load was a distributed load in the x_3 direction. Also substituting the curvature with the assumed kinematics, the residual error became:

$$e(\bar{s}) = \sum YI \sum_{i=0}^{N} i(i-1)a_i \bar{s}^{(i-2)} + \left[\int_{\bar{s}}^{1} f_3(\bar{s}) d\bar{s}\right] \cos\left(\sum_{i=0}^{N} a_i \bar{s}^i\right) \tag{81}$$

Rather than satisfying the moment balance by minimizing the error at every point along the arc length along the beam, the weak formulation of conservation of moment was used. The total moment balance over the length of the beam is satisfied that the integral of the square of the residual was minimized:

$$TRE_M = \int_0^1 \left(e(\bar{s})\right)^2 d\bar{s} \tag{82}$$

The total residual error of the moment was minimized by differentiating the total residual error of the moment with respect to each unknown.

$$\frac{dTRE_M}{da_i} = 0 \tag{83}$$

Note that the polynomial functions that were used did not represent an orthonormal basis set and because of the formulation in the nondimensionalized arc length coordinate system, the magnitude of the coefficients were also determined to be dependent upon the specific loading parameters and beam stiffness for each scenario.. The correction to the unknown polynomial coefficients were iteratively determined using the Newton-Rhapson technique. Because the polynomials represent an orthogonal basis, the resultant was N linearly independent equations with N unknowns, a_i.

$$\frac{d^2TRE_M}{da_i da_j} \Delta a_i = \frac{dTRE_M}{da_i} \tag{84}$$

Applying the boundary conditions from a cantilevered beam, the local change in angle of was assumed to be zero at the root of the beam, resulting in:

$$a_0 = 0 \tag{85}$$

The applied moment at the end of the beam was assumed to be zero however the internal moment induced in the beam is also related to the voltage applied to the beam according to the first governing equation and the first constitutive equation.

$$M_{appl.}(\bar{s} = 1) = 0 = \left(\sum YI\right)\left.\frac{d\theta}{ds}\right|_{s=l} + \Omega V \tag{86}$$

$$a_N = -\sum_{i=0}^{N-1} \frac{i}{N} a_i - \frac{l\Omega}{N\left(\sum YI\right)} V \tag{87}$$

The piezoelectric back-coupling entered into the formulation as a boundary condition to be satisfied after the corrections to the other unknown coefficient.

In the initial conditions for the assumed coefficients, the magnitude of the unknown coefficients was assumed to be zero, corresponding with the physical case of the beam undergoing no deflection. The total residual error of the moment was calculated after each iteration and the program was iterated until the newly determined coefficients resulted in a total residual error of the moment below a predefined criteria. The integration along the arc length of the beam was conducted numerically using 16-point Gauss-Legendre integration. Note that for large polynomials, the bending stiffness matrix has a high condition, resulting in numerical errors and thus problems with iteration convergence. An example of the minimization of the total residual error of the moment was plotted versus iteration also the condition of the bending stiffness matrix, K, was plotted versus iteration in Figure 24.

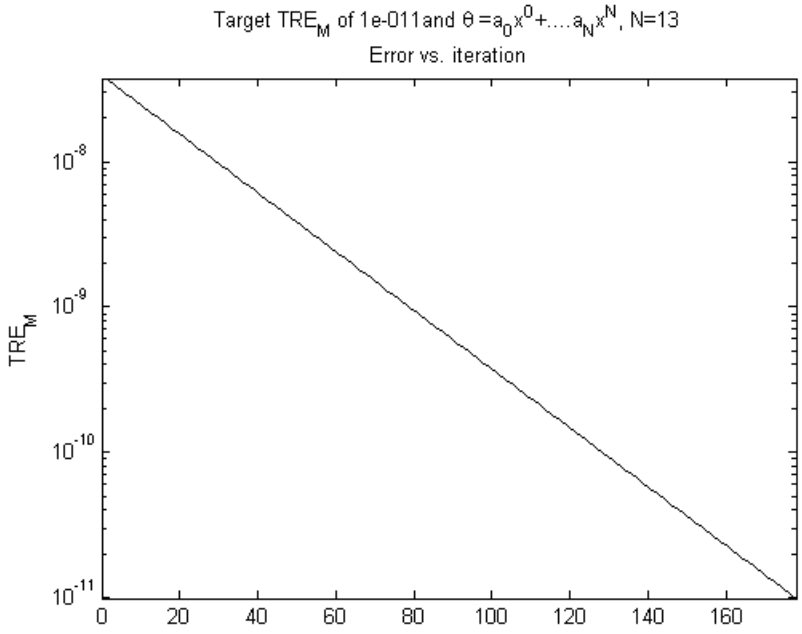

Figure 24: Sample Minimization of Total Residual Error of Moment

For small induced moments due to voltage relative the moments induced by curvature, the resultant equations converge within the same time scale as the formulation written for a beam without piezoelectric coupling. With the solution for coefficients determined for a given loading scenario, the charge generated by the harvester at each time step was determined by the second constitutive equation resulting in the following relation:

$$Q_{layer} = b\int_0^l e_{31}\,\overline{x_{3_{mid}}}\,\frac{d\theta}{ds}\,\bar{ds} = be_{31}\,\overline{x_{3_{mid}}}\sum_{i=0}^{N} a_i \tag{88}$$

Using the previously defined code as a nonlinear transformation of force and voltage into curvature and thus charge displacement, an iterative solution technique was written to determine the curvature of the beam and the voltage of the circuit over the period of analysis for the oscillating energy harvester. The curvature of the beam was linked to the charge displacement using the second constitutive equation. The second governing differential equation regarding the circuit was solved by approximating the

current generated using central time finite differencing method for the charge displaced by the energy harvester, as shown in the equation below:

$$C_p \frac{V_{j+1} - V_{j-1}}{2\Delta t} + \frac{V_j}{R} = \frac{Q_{j+1} - Q_{j-1}}{2\Delta t} \tag{89}$$

Periodic boundary conditions were imposed at the beginning and end of the period of analysis. Such that:

$$V\Big|_{t=0} = V\Big|_{t=\tau} \tag{90}$$

$$\left.\frac{dV}{dt}\right|_{t=0} = \left.\frac{dV}{dt}\right|_{t=\tau} \tag{91}$$

The period of analysis was divided into M equal length subintervals of time. Beginning with t=0, the charge generated by the beam under the specific loading was evaluated at M time steps. The result was a tri-banded matrix of M-linearly independent equations and M unknowns of the form:

$$Z^{-1}V = I \tag{92}$$

The voltage generated across the piezoelectric element and thus load resistor was calculated by inverting the impedance stiffness matrix multiplying by the approximated current generated by the harvester.

The "new" voltages were then substituted into the previously mentioned iterative deflection determination method to find the adjustment to the coefficients for the polynomial approximation of the curvature at each time step. A total residual error metric for the voltage was defined by summing the squares of the differences between the new and old voltage after each iteration:

$$TRE_V = \sum_{j=0}^{M} \left(V_k^{new} - V_{old}^{new}\right)^2 \tag{93}$$

Because the circuit coupled each bending response and the voltage response for all time steps in the time domain, the bending for each harvester could not be directly computed without the knowledge of the voltage from the other time steps. The iterative solution technique would use the nonlinear beam bending program to determine the charge generated by the harvester at each time step. The resultant voltages across the

period of analysis were computed and then substituted into the nonlinear beam bending program to find the resultant bending at each time step. The process was iterated until the total residual error of voltage was calculated to be approximately zero.

$$TRE_{V} \approx 0 \tag{94}$$

$$TRE_{M} \approx 0 \tag{95}$$

Once a solution for the voltage across the period of oscillation had been converged upon, the power dissipated across the resistor at each time step was determined by squaring the voltage at each time step and dividing by the load resistance. The power was averaged over the time domain by numerically integrated using composite Simpson's rule.

3. RESULTS OF ANALYSIS

3.1 Small Deflection Analysis Results

3.1.1 Homogeneous Bimorph Results

The average power generated by the homogeneous bimorph configuration was investigated using the previously mentioned formulation for average power. In the homogeneous bimorph configuration, the piezoelectric layers occupy the entirety of the thickness of the beam.

$$t_p = h \tag{96}$$

Because the homogeneous bimorph configuration is symmetric, the neutral axis was determined to be in the middle of the beam. Accordingly the middle coordinates of the upper and lower layers of the beam and the neutral axis are, respectively:

$$\overline{x_{3,upper}} = \frac{h}{4}, \overline{x_{3,lower}} = -\frac{h}{4} \tag{97}$$

For a homogeneous bimorph with its layers connected in parallel, conservation of charge allowed for the upper and lower piezoelectric layers to be added together. Note that due to the opposite stress state in the upper and lower piezoelectric layers and the manner in which the electrodes were connected, the upper and lower piezoelectric layers must be oriented in the same direction.

$$Q_{tot} = Q_{upper} + Q_{lower} \tag{98}$$

For a homogeneous bimorph the characteristic beam parameters for moment-curvature coupling and moment-voltage coupling were found to be:

$$\sum YI = \frac{bh^3}{12} Y_p, \Omega = \frac{bh}{2} e_{31} \tag{99}$$

Accordingly the magnitude of the charge displacement and the effective capacitance of the piezoelectric element were found to be:

$$Q_p = \frac{6 d_{31} b \psi}{h^2}, C_p = \frac{\left(4\varepsilon_{33}^T - 7 d_{31}^2 Y_p\right) bl}{h} \tag{100}$$

When written using the material constants from the stress-charge relation, the optimized average power generated by the bimorph energy harvester was determined to be:

$$\left\langle \hat{P} \right\rangle = \frac{43.498 \left(d_{31} \psi\right)^2}{\tau\left(4\varepsilon_{33}^T - 7 d_{31}^2 Y_p\right)} \frac{b}{h^3 l} \tag{101}$$

The effect of harvester size on power generation was investigated by establishing a volumetric power metric.

$$\frac{\left\langle \hat{P} \right\rangle}{V} = \frac{43.498 \left(d_{31} \psi\right)^2}{\tau\left(4\varepsilon_{33}^T - 7 d_{31}^2 Y_p\right)} \frac{1}{h^4 l^2} \tag{102}$$

Note that for the bimorph configuration even though length only appears once in the denominator, the loading parameter, Ψ, includes a triple integration with respect to length. Accordingly the volumetric power produced by the energy harvester scales proportional to the fourth power of the length and the inverse of the fourth power of the thickness:

$$\frac{\left\langle \hat{P} \right\rangle}{V} \sim \frac{l^4}{h^4} \tag{103}$$

The material parameters from the average power equation were grouped together to investigate how material choice impacts the average power generated by the heterogeneous bimorph. A piezoelectric electromechanical coupling coefficient was used to group the relevant material parameters:

$$k_{31}^2 = \frac{d_{31}^2 Y_p}{\varepsilon_{33}^T} \tag{104}$$

Then the average power generated by the homogeneous bimorph was rewritten to be the following, where Λ_1 represented a reference power multiplier for the homogeneous bimorph that was dependent upon material choice or internal construction.

$$\left\langle \hat{P} \right\rangle = \frac{k_{31}^2}{Y_p\left(4 - 7 k_{31}^2\right)} \Lambda_1 \tag{105}$$

$$\text{where} \quad \Lambda_1 = \frac{\pi\psi^2}{\tau}\frac{b}{lh^3} \tag{106}$$

Accordingly a power multiplier metric was identified that was dependent upon the piezoelectric material properties but not the physical dimensions of the harvester or the loading conditions. For small values of the electromechanical coupling factor, k_{31}, the power multiplier metric was simplified using a first order Taylor series approximation which resulted in a simplified figure of merit that could be used to identify the effect of material choice on the energy harvester output.

$$\left\langle \hat{P} \right\rangle \sim \frac{d_{31}^2}{\varepsilon_{33}^T} \tag{107}$$

Hence the ratio between the power produced by two homogeneous bimorph energy harvesters of similar dimensions and loading but constructed with different materials was determined by taking the ratio of the material construction parameters. The ratio of the average power generated by a harvester constructed of PVDF to a harvester constructed with PZT is presented in Table 4. The listed material parameters are taken from the material data sheets from the Mide Coorporation and the Measurement Specialties Corporation.

Table 4: Metrics for Material Comparison of Average Power

Defined Material Metrics	**PVDF**	**PZT**	**Ratio for PVDF to PZT**
k_{31}	0.141	0.382	0.369
Material Power Multiplier	1.29×10^{-12} m^3/J	8.05×10^{-13} m^3/J	1.60
Power Multiplier for Small k_{31} Assumption	4.98×10^{-12} m^3/J	2.39×10^{-12} m^3/J	2.08

As can be seen, even though the stress-charge piezoelectric coupling coefficient for PVDF was an order of magnitude lower than that for PZT, the permittivity of PVDF

was also 2 orders of magnitude lower than the permittivity for PZT and the storage modulus for PVDF is and order of magnitude lower than that of PZT. Resultantly it was found that PVDF would produce on the same order of magnitude of power as PZT for the homogeneous bimorph configuration.

3.1.2 Analysis of Heterogeneous Bimorph

The previously mentioned methodology for comparing the size effect and material choice was extended to the heterogeneous bimorph. The homogeneous bimorph case was a special case of the heterogeneous bimorph, the beam was assumed to be composed of only two materials, the active and inactive material. The active material was bonded in equal amounts to the opposite sides of the inactive material, as shown below in Figure 25.

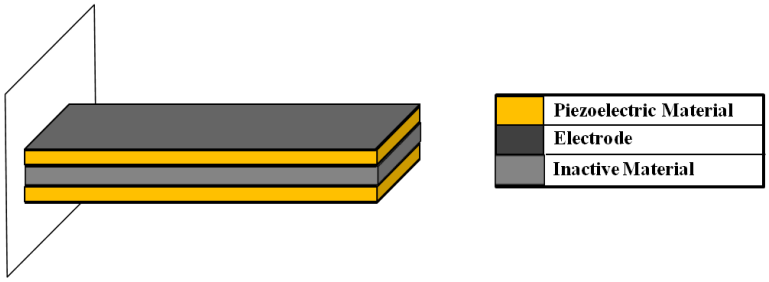

Figure 25: Design Configuration of a Heterogeneous Bimorph

The thickness of the piezoelectric material was defined to be equal to the total thickness of the beam less the thickness of the inactive material.

$$t_p = h - t_i \tag{108}$$

Because the beam construction was assumed to be symmetric, the position of the neutral axis was determined to be in the center of the beam. The location of the middle of the upper and lower piezoelectric layers with respect to neutral axis were determined to be:

$$\overline{x_{3,upper}} = \frac{h}{2} - \frac{t_p}{2}, \overline{x_{3,lower}} = \frac{t_p}{2} - \frac{h}{2} \tag{109}$$

The moment-curvature and moment-voltage coupling coefficients for the heterogeneous bimorph configuration to be implemented in the first governing differential equation were found to be:

$$\sum YI = \frac{b\left(h - t_p\right)^3}{12}\left(Y_i - Y_p\right) + \frac{bh^3}{12}Y_p, \Omega = \frac{b\left(2h - t_p\right)}{2}d_{31}Y_p \tag{110}$$

Then, for the loading for the given application the amplitude of the charge function and the magnitude of the effective capacitance of the piezoelectric element were derived. The equation for optimized average power was then derived using the previously discussed method, the resultant equation can be found in Appendix B. Two construction comparison parameters were established: a stiffness ratio, to vary the ratio of the stiffness of the active to inactive material and a thickness ratio, to vary the total thickness of the active material to the thickness of the beam.

$$\xi = \frac{t_p}{h}, \lambda = \frac{Y_p}{Y_i} \tag{111}$$

The average power equation for the heterogeneous bimorph was then used to compare the ratio in expected average power for two materials. The ratio of average power for a beam constructed using PVDF versus a beam constructed using PZT was varied over the ranges expected for the stiffness ratio and thickness ratio, shown in Figure 26.

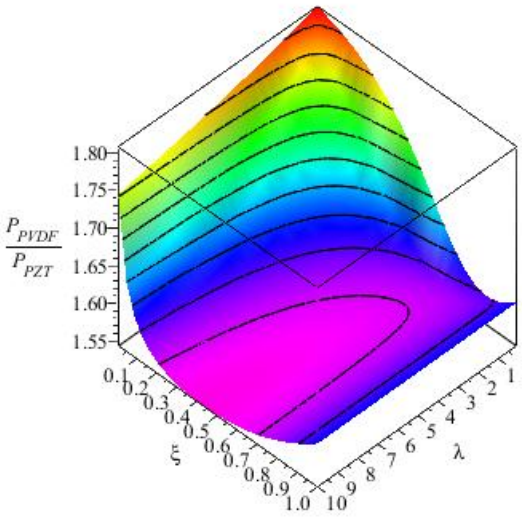

Figure 26: Power Ratio for PVDF to PZT
for Heterogeneous Bimorph of Constant Beam Thickness

The results reflect that for all construction parameters for the heterogeneous bimorph, the expected ratio in average power produced by a harvester constructed using PVDF produced roughly 1.55 to 1.85 times the average power produced by a harvester of similar dimensions using PZT. These values correspond well with the ratio in average power and the first order approximation derived for the homogeneous bimorph. So, the effect of choosing PVDF instead of PZT for construction was effectively decoupled from the analysis of construction by assuming that a scalar value roughly equal to ratio predicted by linear analysis of the homogeneous bimorph. This result was used to represent the difference in effect of piezoelectric material choice across all construction parameter ranges. For the following plots representing predicted average power, only PVDF was plotted.

A similar method was used to determine the effect of the construction parameters on the average power output of the heterogeneous bimorph. The average power equation for the heterogeneous bimorph was divided by the power coefficient, Λ_1, removing the effect of the harvester thickness, width, length and loading conditions from the analysis.

The result was plotted over the range of expected material parameter values, seen in Figure 27.

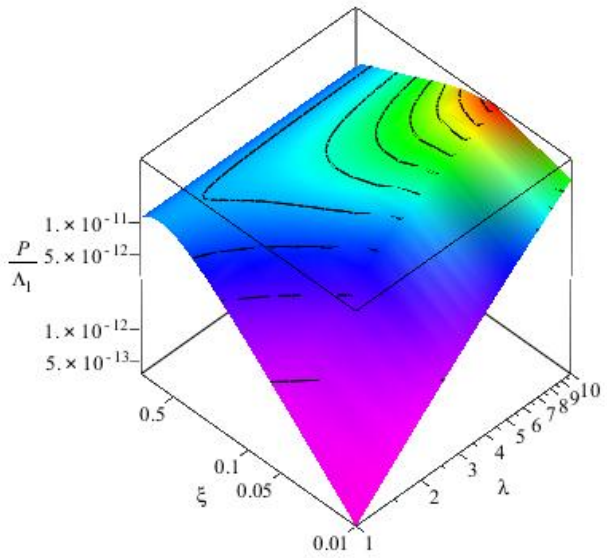

Figure 27: Construction Configuration of N-Layered Active Laminate

Maximizing the ratio of the stiffness of the piezoelectric material to the stiffness of the inactive material maximizes the expected average power produced by the harvester. Piezoelectric layers of thickness on the order of one tenth of the total thickness of the harvester would be needed to attain optimal average power at this thickness. As the stiffness ratio was increased further, the desired thickness of the piezoelectric element also decreased, as shown in Figure 28.

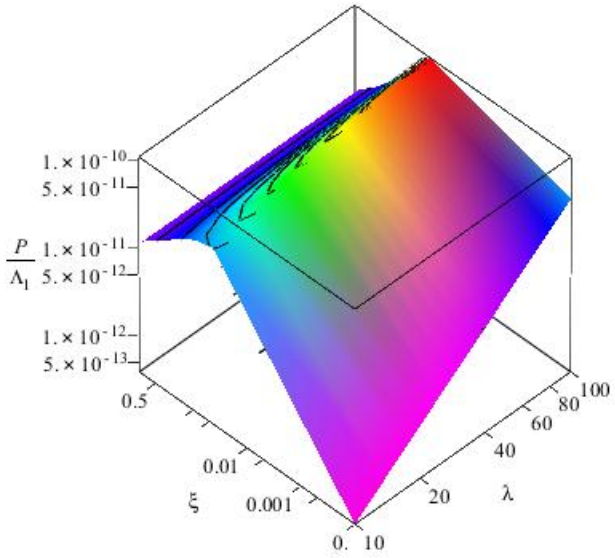

Figure 28: Effect of Construction on Power for a Heterogeneous Bimorph of Large Stiffness Ratio

The average power equation for a heterogeneous bimorph was then divided by the average power equation for a homogeneous bimorph to provide a comparative reference for the effects of construction. The ratio between the average power for a heterogeneous bimorph and a homogeneous bimorph was varied over the relevant ranges for the thickness and stiffness ratios. Because the construction parameters and material choice were found to be inseparably linked, the ratio of the heterogeneous bimorph to the homogeneous bimorph was plotted for PVDF in Figure 29.

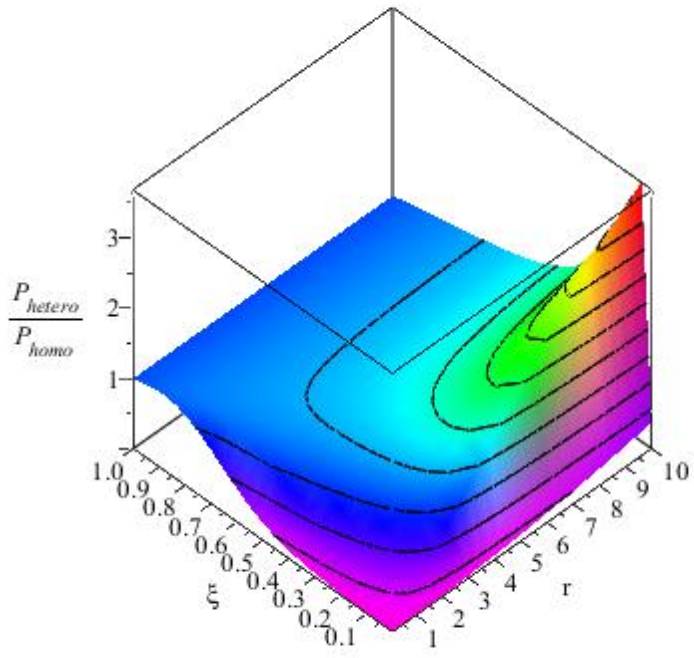

Figure 29: Power Ratio of Heterogeneous to Homogeneous Bimorph for Constant Harvester Thickness

The above plots show that for a harvester of a prescribed thickness, h, more power is produced for cases where the piezoelectric material is significantly stiffer than the inactive material and the piezoelectric material occupies the outermost possible position in the beam. Both of these construction designs concentrate a higher average stress in the piezoelectric material while minimizing the capacitance of the material, allowing for a higher average power output compared to a homogeneous bimorph of equal dimensions. However, decreasing the size of the piezoelectric layer might not be possible due to material availability and production limitations. So, the previous analysis would not apply because it does not take into account the effect of increasing the thickness of the harvester to accommodate the specified thickness of the piezoelectric layers.

As an alternative method to analyzing the effect of harvester configuration, a new reference power multiplier for the homogeneous bimorph is defined where the total thickness of the piezoelectric layers is held constant in the beam constant while the total

thickness of the harvester is allowed to vary. This method enabled the comparison of the positive impact of stress concentration in the piezoelectric element with the negative impact of increasing the harvester thickness. In the new formulation of power of the homogeneous bimorph, the total thickness of the beam was substituted by the total thickness of the piezoelectric element.

$$\left\langle \hat{P} \right\rangle = \frac{k_{31}^{\ 2}}{Y_p\left(4 - 7k_{31}^2\right)}\Lambda_2 \tag{112}$$

$$\text{where} \quad \Lambda_2 = \frac{\pi\psi^{\ 2}}{\tau}\frac{b}{lt_p^{\ 3}} \tag{113}$$

The optimized average power for the heterogeneous bimorph was then divided by the new reference power multiplier to investigate the variation of construction parameters. The variation in the power for various constructions is displayed in Figure 30.

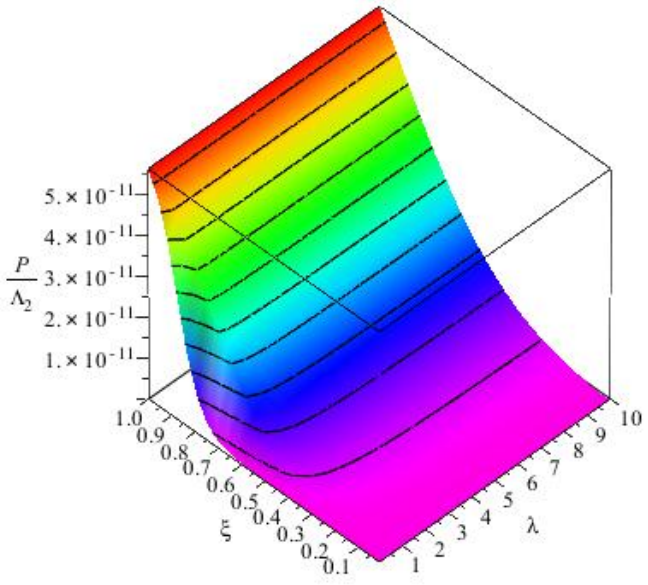

Figure 30: Effect of Construction on Power for a Heterogeneous Bimorph with Specified Piezoelectric Thickness

With the size effect of the thickness of the harvester included, it can be seen that the power produced by the heterogeneous bimorph is maximized when the piezoelectric layer represents the entire thickness of the beam. This result illustrates that the optimal configuration for a heterogeneous bimorph is a homogeneous bimorph, which was confirmed by plotting the power ratio of the heterogeneous bimorph and the homogeneous bimorph for a range of expected construction parameters, shown in Figure 31.

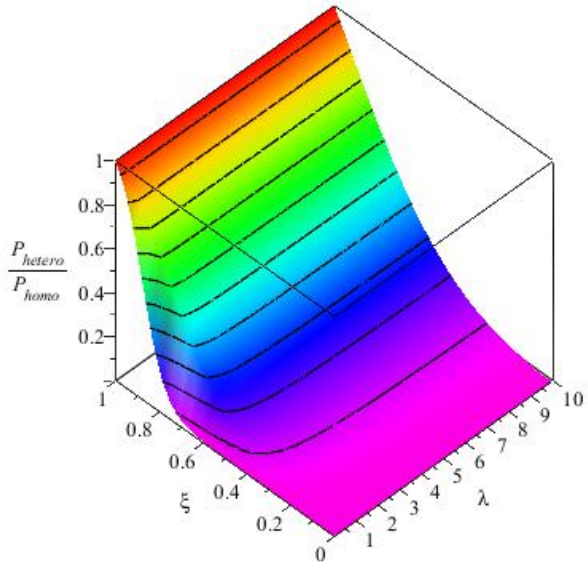

Figure 31: Power Ratio of Heterogeneous to Homogeneous Bimorph for Constant Piezoelectric Thickness

Because of practical considerations, a beam may be modeled as a homogeneous bimorph but constructed as heterogeneous bimorph of known layer thickness. Even when considering lower thickness ratios, the ratio of power produced by a harvester with PVDF as its active material to the power from a harvester with PZT as its active material is on the order of the result predicted from the homogeneous bimorph analysis, as shown in Figure 32.

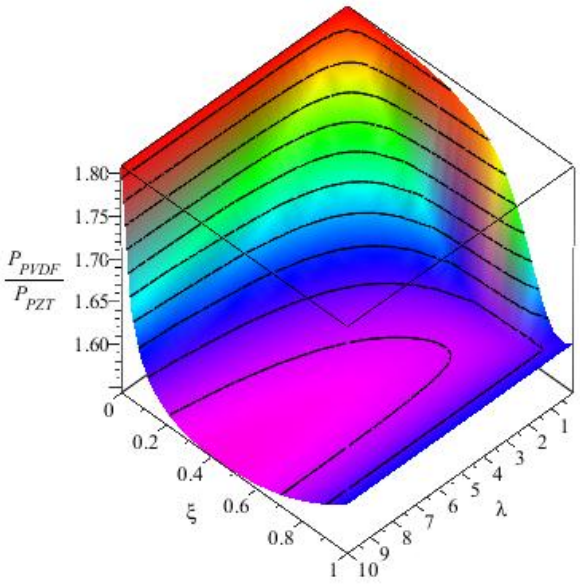

Figure 32: Power Output across Load Resistor as a Function of Circuit Parameters

3.1.3 Analysis of N-Layered Active Laminate

As another practical construction consideration, it could be desirable to use several piezoelectric layers laminated together to approximate a homogeneous bimorph. Production limitations on the layer thickness of PVDF make such a design appealing for large-scale applications where a thick beam is needed to withstand failure criteria, while still maintaining a high piezoelectric volume fraction. An N-layered active laminate was thus defined to be a symmetric beam constructed of N identical layers of a piezoelectric layer bonded to two layers of inactive material of equal thickness, where N is divisible by two. An example of a 2-Layered Active Laminate is shown in Figure 33, with the repeating unit of layers noted.

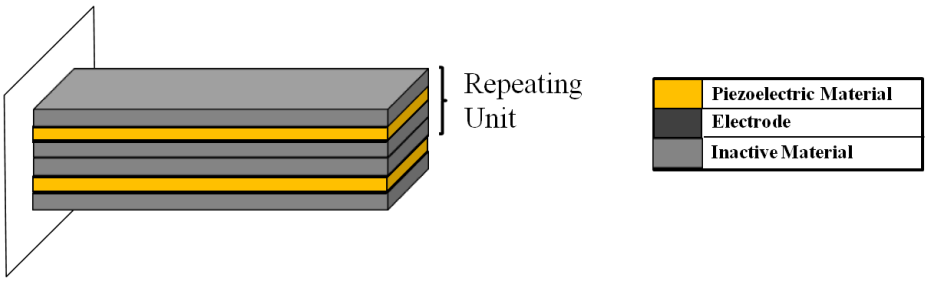

Figure 33: Design Configuration of N-Layered Active Laminate

For a symmetric beam construction the position of the neutral axis was determined to be in the center of the beam. An index, j, ranging from 1 to N/2 was defined denoting the layering position measured from the neutral axis of the beam. The location of the center of the layers in the x_3 direction for the with respect to neutral axis was determined to be:

$$\overline{x_{3,upper}} = \frac{hj}{N} - \frac{h}{2N}, \overline{x_{3,lower}} = -\frac{hj}{N} + \frac{h}{2N} \tag{114}$$

The moment-curvature coupling and moment-voltage coupling coefficients for the N-Layered Active Laminate were found to be:

$$\sum YI = \frac{1}{12}\frac{b(Y_p - Y_i)t_p^{\,3}}{N^2} + \frac{1}{12}bY_i h^3 + \frac{1}{12}\frac{\left((Y_p - Y_i)N^2 - (Y_p - Y_i)\right)t_p h^2}{N^2} \tag{115}$$

$$\Omega = \frac{bhN}{4} d_{31} Y_p \tag{116}$$

The equation for optimized average power was then derived using the previously discussed method and the construction and stiffness ratio were substituted to nondimensionalize the range of construction parameters. For the case where the thickness of the piezoelectric material approaches the total thickness of the beam and the number of material layers approaches infinity, the result from the homogeneous bimorph case is recovered. To illustrate this effect, a sample case with a finite number of layers was chosen. The following results were presented for the case where N=10.

Following the previously defined method for material comparison, the average power produced by a 10-Layered Active Laminate was compared for PVDF and PZT by plotting the ratio of average powers over the design space as shown in Figure 34. Again

the material comparison factor from the homogeneous bimorph case is recovered for large thickness ratios. PVDF was shown to produce average power on the same order of magnitude of the piezoceramic, PZT and was effectively bounded on the low end by the homogeneous bimorph estimate.

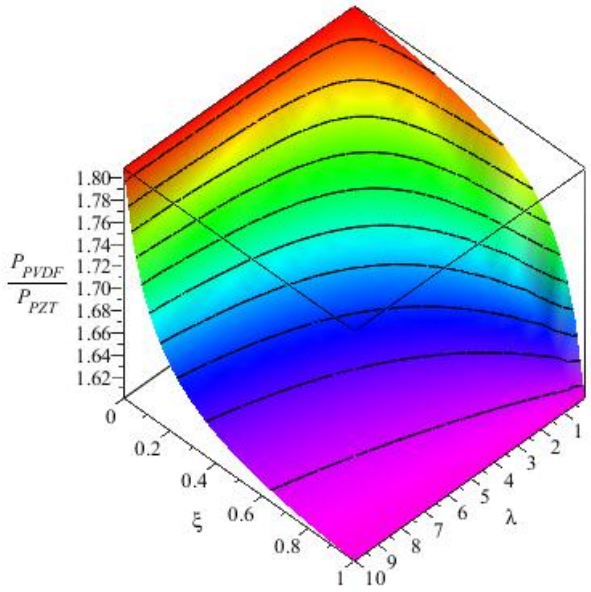

Figure 34: Power Ratio of PVDF to PZT for 10-Layered Active Laminate

Following the previous result from the heterogeneous bimorph, it was expected that the power produced by the N-Layered Active Laminate would be optimized when the piezoelectric thickness approached the total thickness of the harvester. The average power from the 10-Layered Active Laminate was divided by the new reference power multiplier and plotted over the design space, as shown in Figure 35.

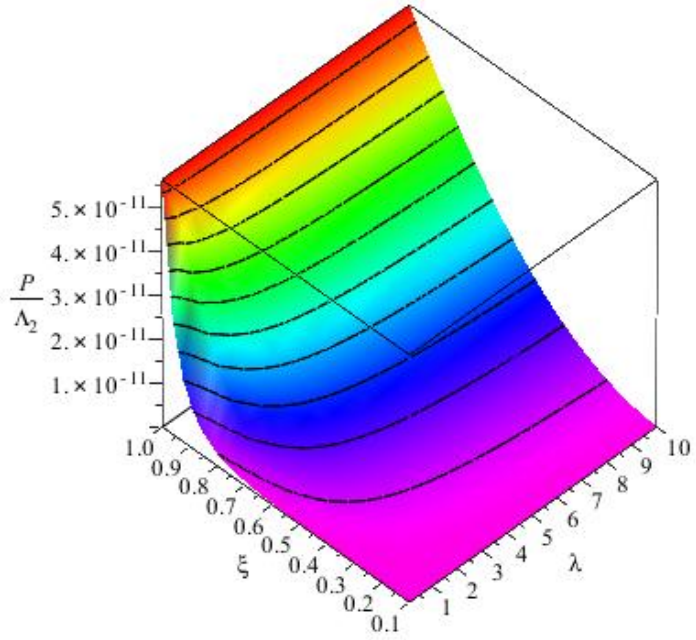

Figure 35: Effect of Construction on Power for 10-Layered Active Laminate

The average power equation for a 10-Layered Active Laminate was then divided by the average power equation for a homogeneous bimorph and varied over the design space to analyze the effects of construction. The result is shown in Figure 36.

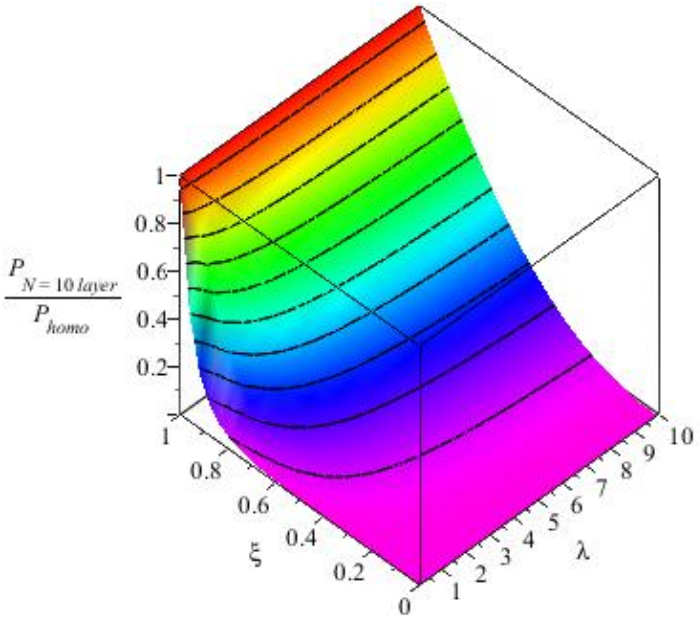

Figure 36: Power Ratio of a 10-Layered Active Laminate to Homogeneous Bimorph

The result from the 10-Layered Active Laminate was shown to bear a strong resemblance to the result from the heterogeneous bimorph. To directly compare the results, the average power from the 10-Layered Active Laminate was divided by the average power from the heterogeneous bimorph and varied over the design space.

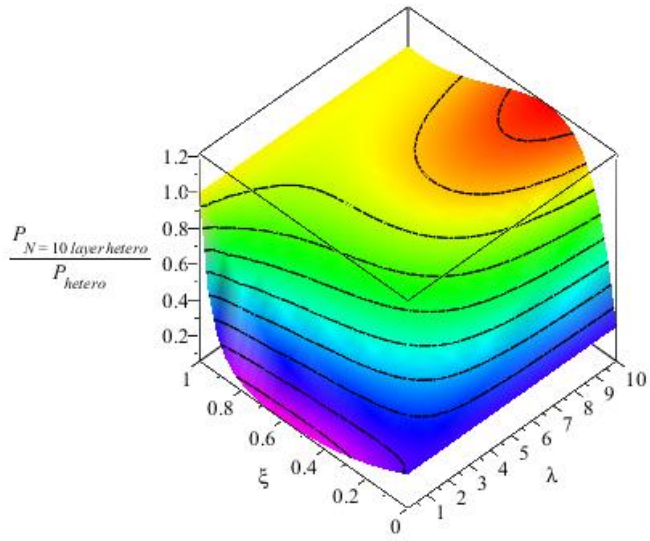

Figure 37: Construction Comparison to Heterogeneous Bimorph for PVDF

For large stiffness ratios, the 10-Layered active laminate exceeded the performance of the heterogeneous bimorph, and as expected for large thickness ratios, the 10-Layered Active Laminate converged to the result from the homogeneous bimorph.

3.1.4 Analysis of Unimorph Configuration

Finally, the analysis for optimized average power was extended to another common configuration in energy harvesting literature, the unimorph configuration. In the unimorph a single layer of an active material is layered upon an inactive material, as shown in Figure 38:

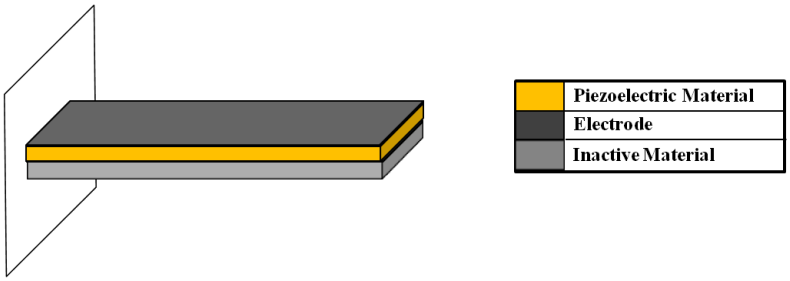

Figure 38: Design Configuration of Unimorph

The unimorph configuration was considered to be desirable because, for relatively stiff inactive materials, the configuration shifted the piezoelectric material further away from the neutral axis of the beam. The increased distance between the neutral axis and the piezoelectric element would increase the average stress in the piezoelectric element and increase power output.

Because the construction of the unimorph was not symmetric with respect to the middle of the beam, the neutral axis was not found to be located in the geometric center of the beam, but rather to be dependent upon material properties. For a beam composed of only inactive materials, the neutral axis would be found by balancing the internal moment of the beam about a single point along the x_3 axis for all curvature scenarios. However, because the beam was also composed of active materials connected across a voltage, the moment induced in the unimorph was also dependent upon the ratio between the stress in the beam induced by bending and the stress in the beam induced by the piezoelectric back-coupling, as seen in the following equation where x_3^* represents the distance of the neutral axis from the bottom of the beam.

$$x_3^* = \frac{1}{2}\frac{Y_i h^2 - 2Y_i h t_p + Y_i t_p^2 + 2Y_p h t_p - Y_p t_p^2}{Y_i h - Y_i t_p + Y_p t_p} + \frac{d_{31} Y_p}{Y_i h - Y_i t_p + Y_p t_p}\frac{V}{\kappa} \tag{117}$$

Then, the distance from the center of the piezoelectric layer to the neutral axis was determined to be:

$$\overline{x_{3,upper}} = h - \frac{t_p}{2} - x_3^* \tag{118}$$

Similar to the homogeneous bimorph, the total thickness of the inactive layer was defined to be the thickness of the total beam less the thickness of the thickness of the piezoelectric layer:

$$t_i = h - t_p \tag{119}$$

Using this relation, the moment-curvature and moment-voltage coupling coefficients were found to be:

$$\sum YI = \frac{1}{12}\frac{b\left(t_p^4 Y_p^2 - 2t_p^4 Y_i Y_p + 4ht_p^3 Y_i Y_p - 6h^2 t_p^3 Y_i Y_p + 4h^3 t_p Y_i Y_p + t_p^4 Y_i^2 - 4ht_p^3 Y_i^2 + 6h^2 t_p^2 Y_i^2 - 4h^3 t_p Y_i^2 + h^4 Y_i^2\right)}{Y_i\left(h - t_p\right) + Y_p t_p} \tag{120}$$

$$\Omega = \frac{bh\left(h - t_p\right)Y_i}{2\left(Y_i h - Y_i t_p + Y_p t_p\right)} d_{31} Y_p \tag{121}$$

Using the same stiffness and thickness ratios as before, the average power generated by the unimorph was derived and the thickness and stiffness ratios were substituted to non-dimensionalize the design space. Following the previously defined method for material comparison, the average power produced by a unimorph was compared for PVDF and PZT by plotting the ratio of average powers over the design space, as seen in Figure 39.

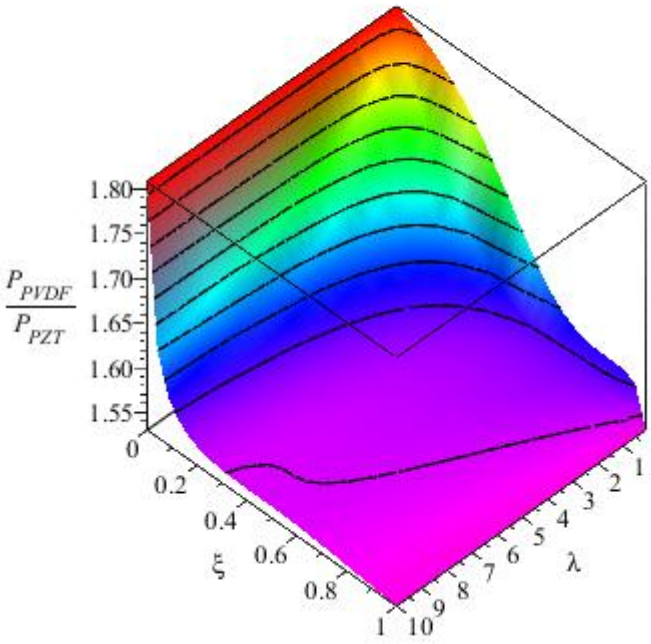

Figure 39: Power Ratio of PVDF to PZT for a Unimorph

For the unimorph configuration, the material comparison factor was bounded by the same values as for the previous configurations. It was expected that the unimorph would produce the most power for thin layers of piezoelectric material bonded to a very stiff inactive substrate. The average power equation for the unimorph was divided by the reference power multiplier and plotted over the design space in Figure 40.

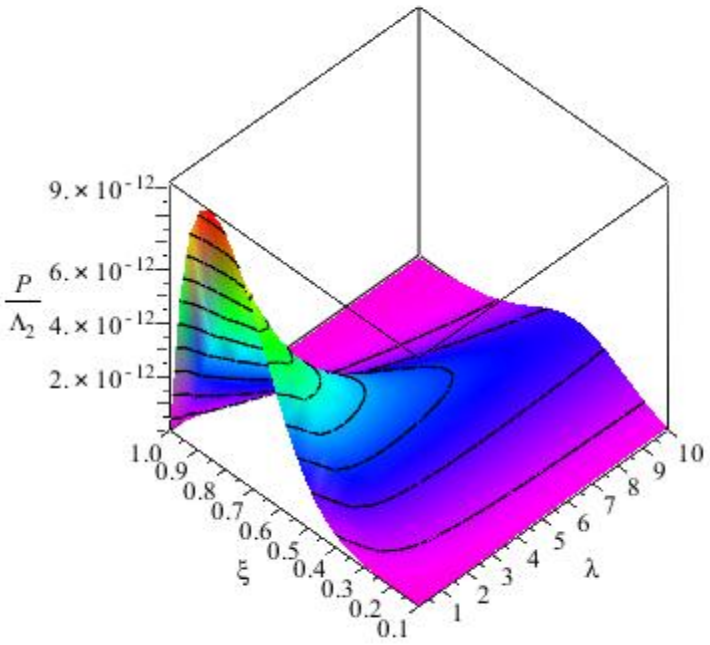

Figure 40: Effect of Construction on Power for a Unimorph

As expected, the power for the unimorph was maximized for a thin layer of piezoelectric material bonded to a relatively stiff inactive substrate. However, to clarify if such a configuration would produce the most average power for a specified thickness of piezoelectric material, the result was compared to the previously determined optimal configuration for energy harvester construction. Thus, the average power equation for a unimorph was then divided by the average power equation for a homogeneous bimorph and plotted over the design space, as shown in Figure 41.

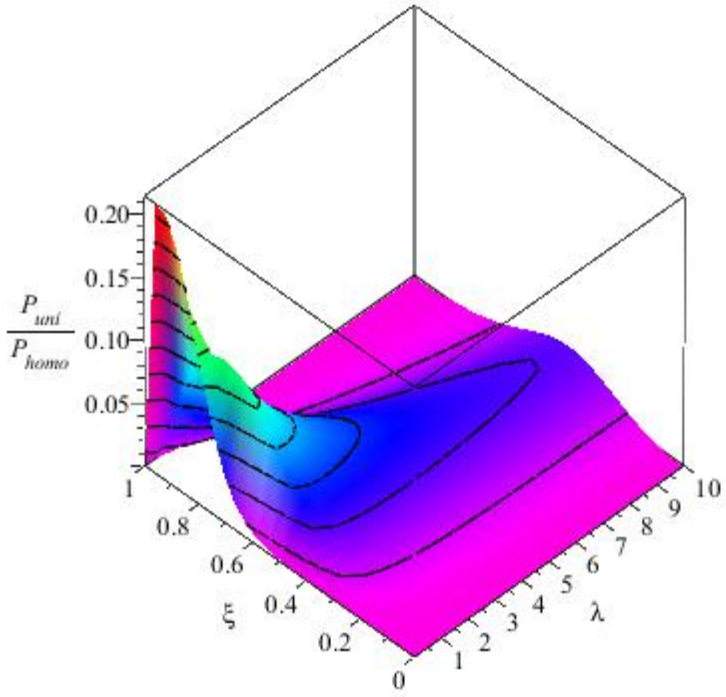

Figure 41: Power Ratio of a Unimorph to Homogeneous Bimorph

Even for very thin piezoelectric layers and relatively stiff inactive substrates, the unimorph configuration was shown to produce approximately 20% of the power compared to a homogeneous bimorph configuration with the same piezoelectric material.

As a final step in comparison, the unimorph configuration was compared to the heterogeneous bimorph configuration. The ratio between the average powers was plotted over the design space in Figure 42.

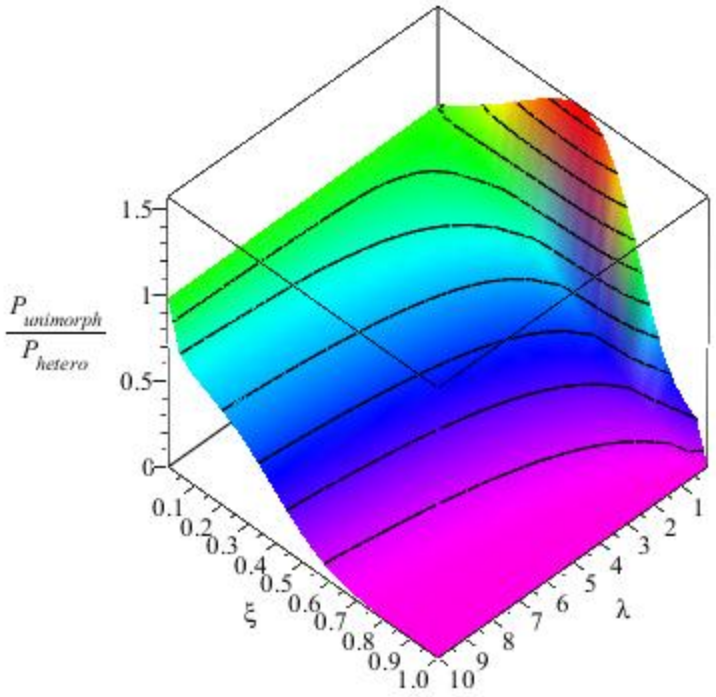

Figure 42: Power Ratio of Unimorph to a Heterogeneous Bimorph

For configurations where the substrate was more compliant than the piezoelectric material, the unimorph produced a power less than or equal to the heterogeneous bimorph. However, for very stiff inactive materials, the unimorph could produce more average power for lower thickness ratios. This plot highlights the advantages of the two configurations. The heterogeneous bimorph excels at producing power when bonded to relatively compliant materials where the piezoelectric material occupies the majority of the volume. The unimorph excels at producing power when the piezoelectric layer is bonded to a relatively stiff material and at low volume fractions of piezoelectric material. However, note that as previously stated, the optimal configuration for a given thickness of piezoelectric material was determined to be the homogeneous bimorph configuration.

3.2 Experimental Results

The calibrated moment applied to the inactive beam strain gage was measured at 100 Hz for 10 seconds, corresponding to 10 periods. The phase of the applied loading was determined by finding when the applied moment first crossed from a negative to a positive value. The magnitude of the applied moment was then fit to the data using a least squares approximation. A sample of the experimental data and the applied moment was shown below in Figure 43.

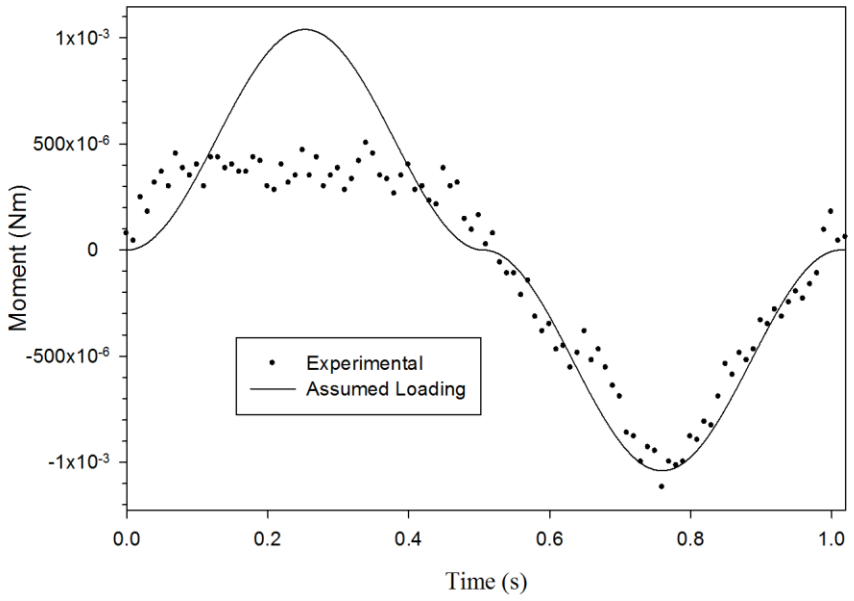

Figure 43: Sample of Applied Moment Data and Approximation

The results from the strain gage measurement were not symmetric either due to the wires from the strain gage preventing the beam bending completely for low magnitudes of force, or due to the wave height not varying exactly sinusoidally with time. An image of a cross section of the wave propagation is shown in Figure 44 with a 1 inch by 1 foot ruler shown at the bottom for a reference length.

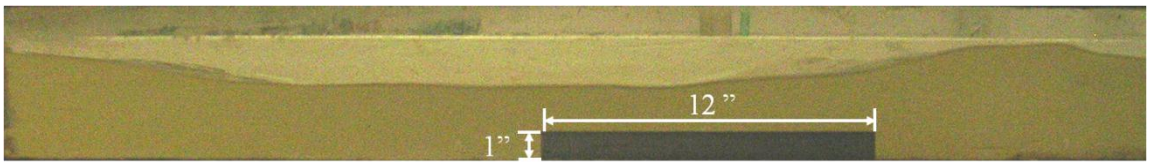

Figure 44: Cross-Section of Wave Profile

Using this initial measurement of the magnitude of the applied moment, the magnitude of the drag coefficient was determined using the calculated flow speed. Using the previous linear analysis, the approximate magnitude of the optimal load resistance was determined to be on the order of 1.5 MΩ. A 5 MΩ Honeywell potentiometer was used to vary the value of the load resistance to vary between 2.5 kΩ and 2.5 MΩ. The value of the load resistance was measured before each set of data acquisition by taking a known 5V and a known resistor of 1 MΩ. The load resistor was connected in series with the known resistor and the difference in voltage drop across the load resistor was compared with the known resistor to determine the value of the load resistor. It was assumed that the difference in resistance between the resistance calibration circuit and the energy harvester circuit was negligibly small compared to magnitude of the load resistance.

The power across the load resistor was calculated at each time step by dividing the square of the measured voltage by the load resistance magnitude. The resultant average power was found by averaging the power found at each time step over the total time for data acquisition. At each load resistance, the voltage was acquired at 100 Hz over a period of 10 seconds, assumedly capturing 10 periods. A sample of the measured voltage and the predicted voltage through linear analysis is shown below in Figure 45.

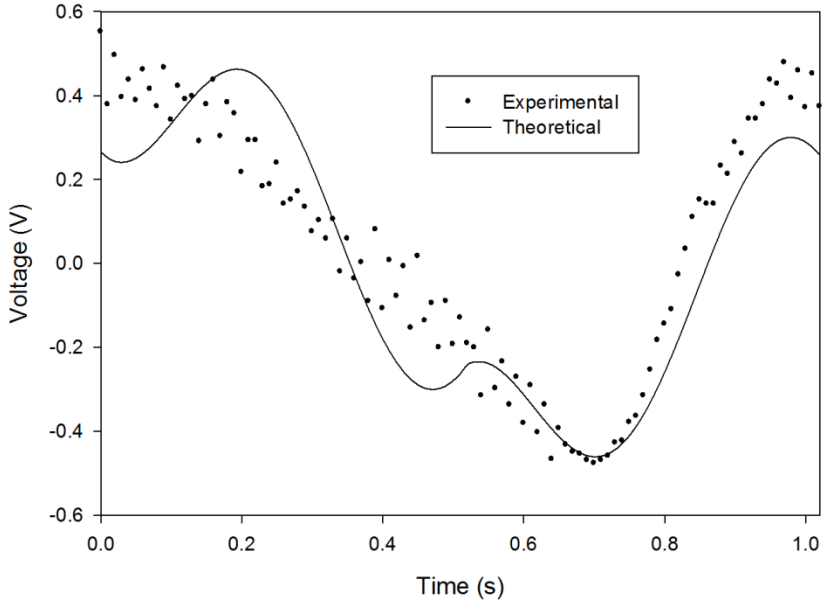

Figure 45: Sample Voltage across Load Resistor and Calibrated Approximation

Average power data was collected for the previously described range of load resistances for three QP20n harvesters under the same loading conditions. The results were plotted on the same plot as the predictions of linear analysis below in Figure 46 along with the optimized power and optimal load resistance listed next to the legend.

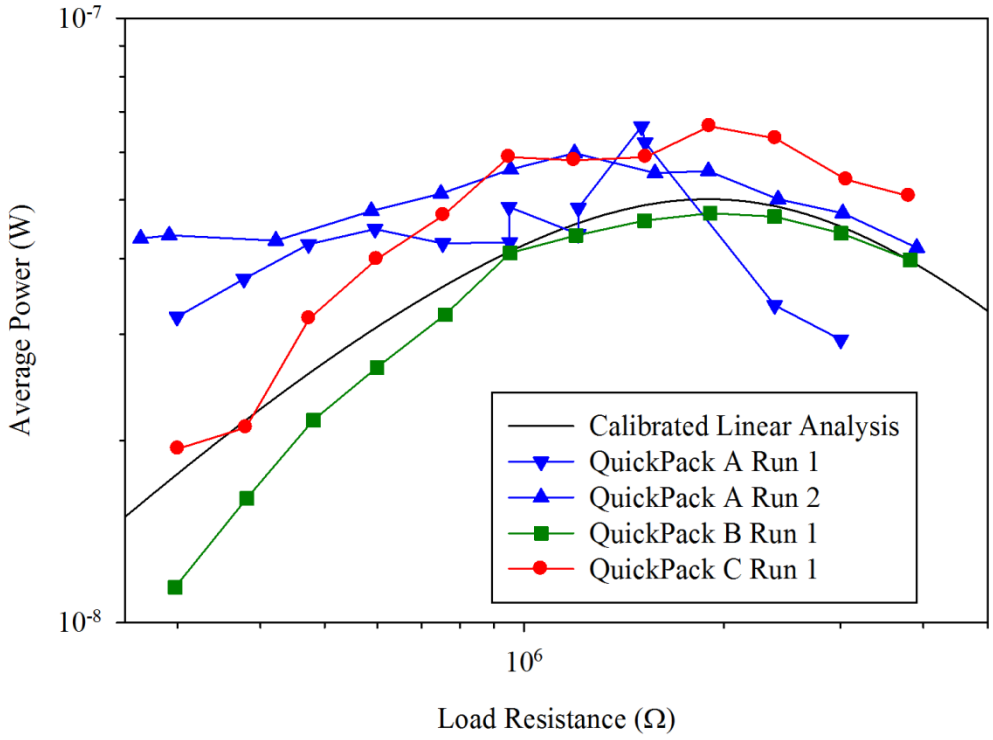

Figure 46: Experimental Average Power and Calibrated Approximation

As can be seen by the difference in the measured average power at the various resistances by testing three identical piezoelectric elements from the same batch under the same loading conditions with the same resistance, inaccuracy in measuring the characterization parameters of the loading conditions and dimensions accounted for the largest amount of error. Accordingly it was concluded that the average power prediction theory correctly predicted the correct order of magnitude of power production as well as the load resistance for peak power output.

3.3 Large Deflection Analysis Results

3.3.1 Comparison with Linear Analysis Results

The large deflection code was validated by comparing the calculated voltage over the time domain and the calculated average power with results predicted by linear analysis. To reduce the run-time of the code, it was assumed that the magnitude of the distributed load was constant over the length of the beam. The value for the magnitude of the distributed load was calculated at the midpoint along the length of the beam. A specific example was chosen for presentation from arbitrary conditions that from loading in a wave tank that would result in very small deflections of the energy harvester. The assumed conditions for the analysis are listed below in Table 5. The resultant amplitude of the charge displacement and the magnitude of the effective piezoelectric capacitance from linear analysis were also listed.

Table 5: Summary of Conditions Used for Comparison

Parameter	Value
Loading-Related Parameters	
Water Depth (d)	0.10 m
Wave Crest-Trough Distance (H)	0.02 m
Wave Period (τ)	1.60 sec
Calculated Wavelength (L)	1.54 m
Depth Averaged Maximum Flow Speed (u_{max})	9.57 cm/s
Drag Coefficient (C_d)	1.204
Beam-Characterizing Parameters	
Beam Length (l)	6 cm
Beam Width (b)	1 cm
Beam Thickness (h)	1 mm
Number of Active Material Layers	2
Construction Configuration	Homogeneous Bimorph
Active Material	PZT
Connection Pattern	Parallel
Large Deflection Convergence Parameters	
Number of Time Steps Used	80
Degree of Polynomial Approximation	12
TRE_M Criteria	10^{-11}
TRE_V Criteria	10^{-7}

The calculated voltage the across the time domain for linear analysis is shown below in Figure 47a and the linearly interpolated results for the voltage from the nonlinear beam bending program are shown in Figure 47b for the optimized load resistance.

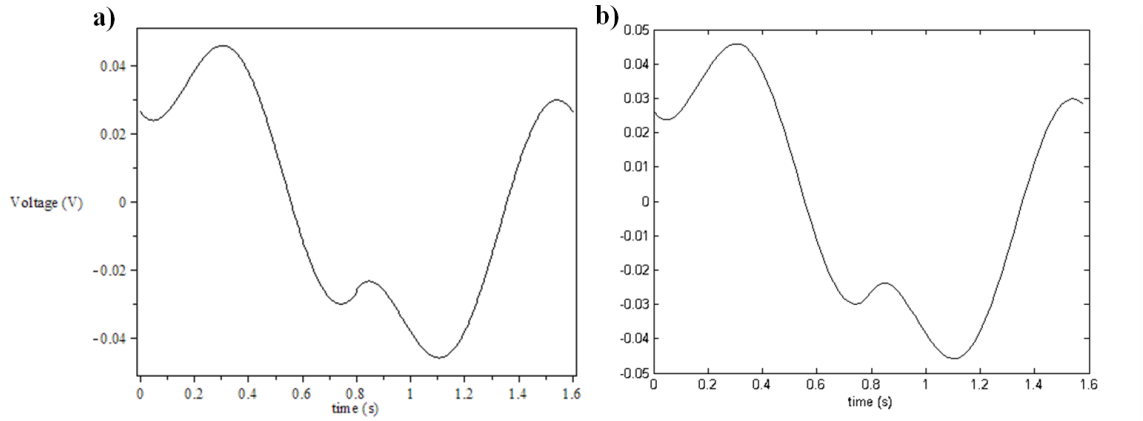

Figure 47: Sample Comparison of Voltage over One Period.
for (a) linear analysis and (b) large deflection program

As can be seen in the previous figure, the results from the nonlinear bending program accurately captured the voltage predicted by linear analysis. Table 6 lists the parameters used to calculate the optimized load resistance through linear analysis as well as a performance comparison.

Table 6: Results from Comparison

Parameter	Linear Value	Large Deflection Value
Charge Amplitude (Q_p)	$2.26 \cdot 10^{-9}$ A	-
Effective Piezo Capacitance (C_p)	$3.08 \cdot 10^{-8}$ F	-
Optimal Load Resistance (R_{load})	7.54 MΩ	-
Peak Voltage Value	0.0459 V	0.0471 V
Calculated Average Power	$1.255 \cdot 10^{-10}$ W	$1.256 \cdot 10^{-10}$ W

The large deflection code clearly captured the results of the linear analysis with arbitrary error, determined by the values of the total residual errors of moment and voltage that were chosen. For the finite values of total residual moment and voltage error, the program converged to a solution within a few iterations of voltage, as shown in Figure 48.

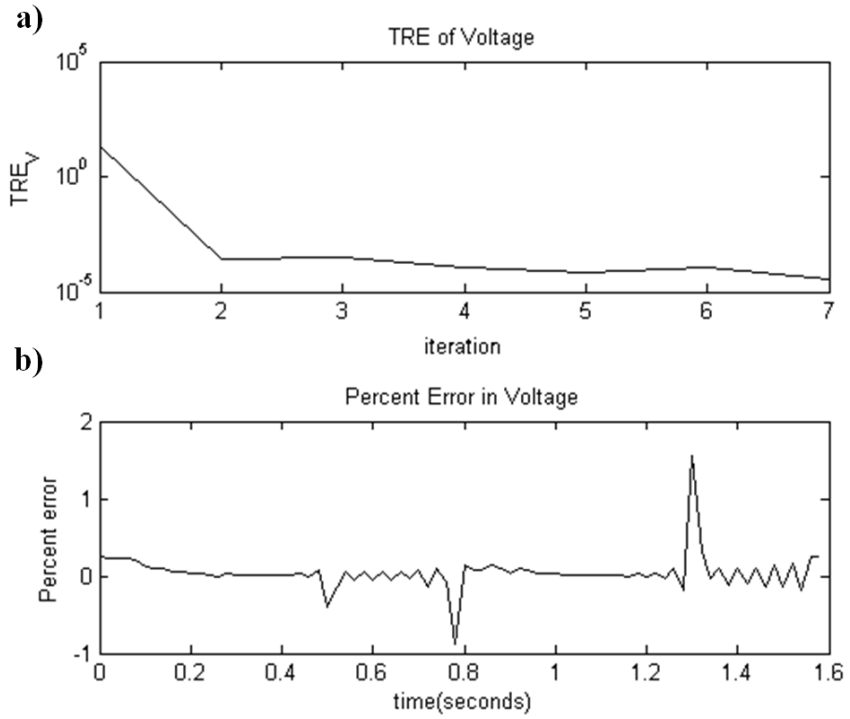

Figure 48: Sample Summary of Error in Voltage Calculation.
a) convergence of total residual error of voltage with iteration and
b) percent change in voltage at solution

3.3.2 Determination of Approximation Parameters

The previously mentioned code was written in MATLAB, parallelized and executed on a 64-bit 3.3 Ghz PC. Initially, the large deflection program was run using a 15^{th} order polynomial to approximate the curvature of the beam at 100 time steps over the period, which required over an hour to complete all of the required calculations and converge to a solution. It was sought to reduce the order of the polynomial approximation of curvature as well as the number of steps at which the curvature was evaluated in order to reduce the computation time of the result. The desired goal was to maintain 1% or less error in deviation of the average power calculation from the linear analysis while reducing the run-time of the code to less than 10 minutes. The sample configuration used for the analysis was a homogeneous bimorph with the dimensions

expected from the QuickPack harvester and for loading conditions expected from the wave tank. A trade study was completed for the analysis of the impact of the order of polynomial and the number of time steps used for analysis over the period. The results are shown in Table 7.

Table 7: Impact of Approximation Parameters on Run-Time

Degree of Polynomial Approximation of Local Angle	Number of Time Steps Used over Period	Calculated Power from Large Deflection Code	Percent Error in Average Power Calculation	Time Required for Convergence
13	20	9.96 nW	-1.20%	13.2 min
13	30	10.05 nW	-0.30%	16.6 min
13	40	10.10 nW	-0.15%	20.1 min
13	60	10.12 nW	-0.41%	27.2 min
13	80	10.13 nW	-0.50%	33.2 min
15	20	9.97 nW	-1.08%	27.5 min
11	20	9.87 nW	-2.13%	4.8 min
11	30	9.96 nW	-1.23%	6.7 min
11	40	10.00 nW	-0.82%	8.3 min
11	80	10.03 nW	-0.49%	16.7 min
12	30	10.03 nW	-0.49%	10.6 min
12	40	10.07 nW	-0.08%	14.3 min

The order of the polynomial approximation of curvature for the nonlinear beam bending strongly controlled the amount of time required for the program to converge. The result of the trade study showed that reduction of the degree of approximation to an 11^{th} order polynomial over 40 time steps, resulting in less than 1% error.

3.3.3 The Effect Piezoelectric Back-Coupling on Power Prediction

The large deflection code allowed for an iterative solution technique for solving the coupled equations of beam bending and voltage response in the circuit. Early in energy harvesting analysis and still persistent today, some analysis ignores the effect of the second constitutive relation, resulting in the following effective adjustment in the constitutive equations.

Ignoring the piezoelectric back-coupling effectively decouples the two equations, allowing for direct solution of the assumed voltage created by the charge displaced by the energy harvester interacting with the impedance of the circuit. This assumption is valid if the effect of the electric field on the stress in the beam is relatively small compared to the stresses induced by the bending strain, which is not always true, especially in large scale applications with large impedances where the voltage and electrical fields within the piezoelectric material can be very high. Direct solution of the voltage and thus power is desirable because it would allow the average power generated by the energy harvester to be calculated knowing only the loading on the harvester even for nonlinear large deflection analysis.

Both the linear analysis and large deflection program were used to determine the effect on the average power generated by the energy harvester by ignoring the piezoelectric back-coupling. The loading conditions for the given scenario used for the comparative analysis are listed in Table 8.

Table 8: Summary of Conditions Used for Device Selection

Parameter	Value
Loading-Related Parameters	
Water Depth (d)	0.127 m
Wave Crest-Trough Distance (H)	0.040 m
Wave Period (τ)	1.25 sec
Calculated Wavelength (L)	1.32
Depth Averaged Maximum Flow Speed (u_{max})	16.35 cm/s
Drag Coefficient (C_d)	1.14

The assumed sizes, dimensions and relevant parameters for several commercially available QuickPack harvesters were tabulated in Table 9 and the respective values for their volumetric PVDF equivalent were shown in Table 10.

Table 9: Summary of Parameters of Various QuickPack Harvesters

Parameter	QP20n	QP20w	QP21b	QP22b
Length (l)	4.59 cm	4.62 cm	3.36 cm	2.60 cm
Width (b)	2.05 cm	3.33 cm	1.42 cm	0.381 cm
Total Piezo Thickness (t_p)	0.508 mm	0.508 mm	0.406 mm	0.406 mm
Thickness (h)	0.762 mm			
Number of Active Material Layers	2			
Construction Configuration	Two-Layered Heterogeneous Bimorph			
Active Material	PZT			
Inactive Material	Epoxy			

Table 10: Summary of Parameters of Equivalent PVDF Harvesters

Parameter	**QP20n$_{equiv}$**	**QP20w$_{equiv}$**	**QP21b$_{equiv}$**	**QP22b$_{equiv}$**
Length (l)	4.59 cm	4.62 cm	3.36 cm	2.60 cm
Width (b)	1.90 cm	1.90 cm	1.20 cm	1.20 cm
Total Piezo Thickness (t_p)	0.520 mm	0.520 mm	0.416 mm	0.416 mm
Thickness (h)	0.640 mm		0.512 mm	
Number of Active Material Layers	10		8	
Construction Configuration	N-Layered Heterogeneous Bimorph			
Active Material	PVDF			
Inactive Material	Epoxy			

The optimal load resistance was calculated using linear analysis and then the average power generated by the various energy harvesters for the fully-coupled constitutive equations was calculated for linear analysis and confirmed using the large deflection code. The average power for each configuration was divided by the total volume of the energy harvester and plotted in Figure 49.

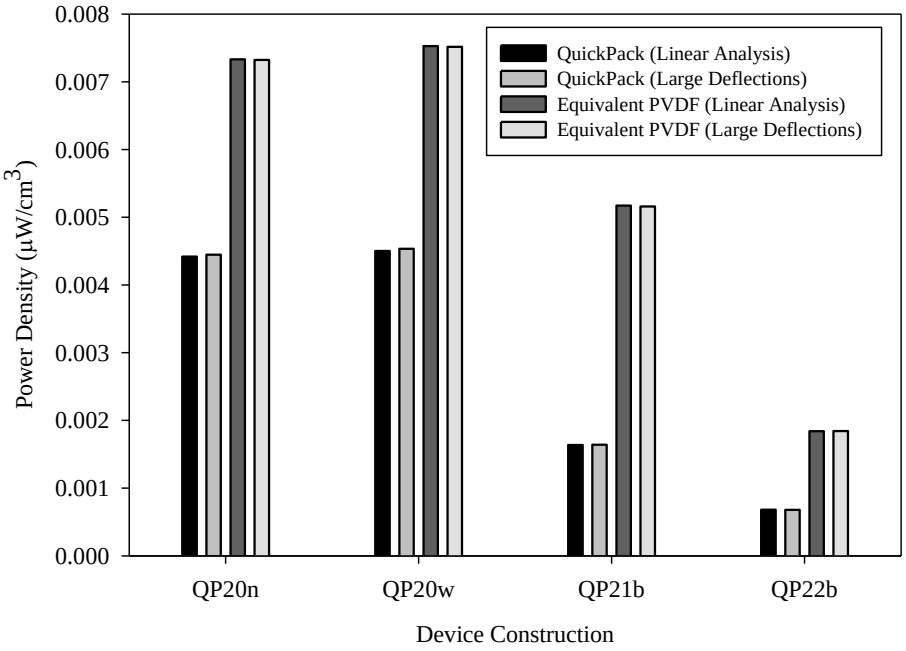

Figure 49: Comparison of Power Density for QuickPacks with Equivalent PVDF Constructions

As was previously illustrated by the linear analysis, equivalent PVDF harvesters to the PZT energy harvesters produced approximately twice the optimized volumetric average power as the PZT harvesters. The constitutive equations were then altered to remove the effect of the piezoelectric back-coupling from both the linear analysis and the large deflection code. The resultant percent change in average power for each of the configurations was plotted in Figure 50.

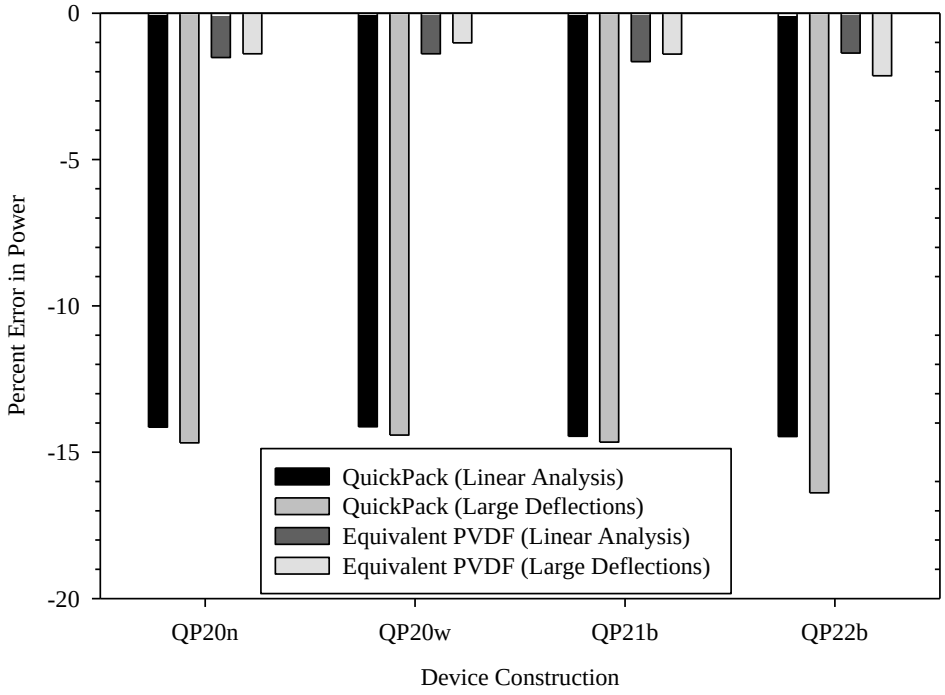

Figure 50: Error in Power Calculation with No Piezoelectric Back-Coupling

Interestingly, the effect of ignoring the piezoelectric back-coupling did not have the same effect for both PVDF and PZT harvesters.

3.3.4 Effect of Length on Power Density

Part of the variation of volumetric average power in energy harvesters in the previous figure was due to the difference in material choice. However, even the PZT harvesters showed a difference in volumetric average power. All of the QuickPack harvesters consisted of approximately the same construction resulting in approximately the same thickness, but the harvesters did not have the same lengths. As shown through linear analysis, the volumetric power of the energy harvester scales with approximately the fourth power of the length. To confirm this relation from linear analysis, the large deflection program was used to determine the average power generated by the harvester

for harvesters of various lengths. Initially, the relation was confirmed for harvesters under loading conditions that would result in very small deflections. The loading conditions previously mentioned in Table 8 were used. The optimized load resistances at each length were chosen using linear analysis. The characteristic parameters of the energy harvester were listed below in Table 11.

Table 11: Summary of Conditions for Harvester Length Study

Parameter	Value
Beam Length (l)	3.5 cm → 10 cm
Beam Width (b)	1.9 cm
Beam Thickness (h)	0.64 mm
Piezo Thickness (t_p)	0.52 mm
Number of Active Material Layers	10
Construction Configuration	N-Layered
Active Material	PVDF
Inactive Material	Epoxy (Y_i = 2 GPa)
Connection Pattern	Parallel

The results were fit using a least-squares method to a power function of degree 4 of the length of the beam. The result is also plotted in Figure 51.

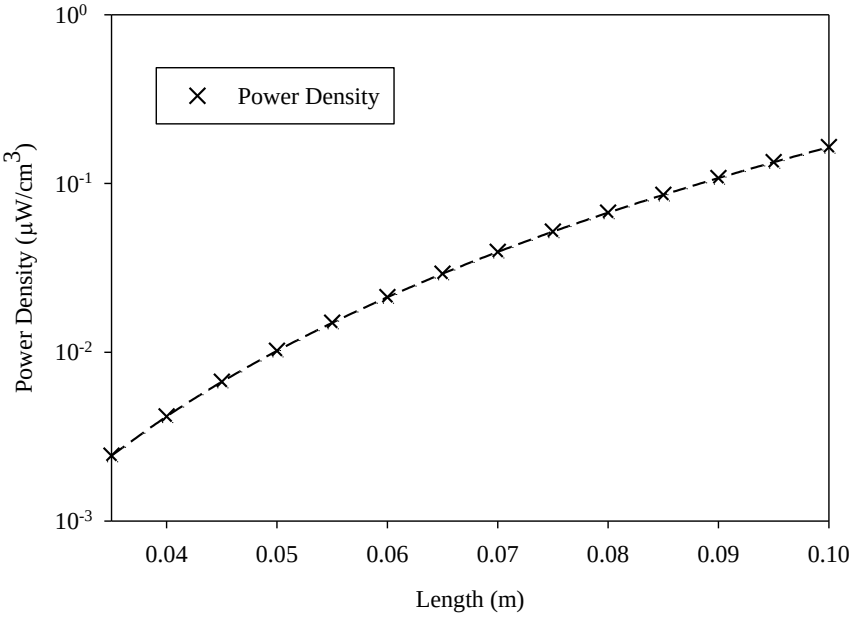

Figure 51: Effect of Length on Power Density for Small Deflections

This curve was then extrapolated for energy harvesters with lengths on the order of 1 meter. The average power was calculated using this extrapolated curve for a sample energy harvester of width and thickness similar and flow speed on the order of the linear analysis. The results from the extrapolated linear analysis are shown below in Table 12.

Table 12: Extrapolated Linear Analysis Results

Beam Length	Extrapolated Volumetric Avg. Power	Extrapolated Total Average Power
0.1 m	$1.64 \cdot 10^{-7}$ W/cm^3	$2.00 \cdot 10^{-7}$ W
0.5 m	$1.04 \cdot 10^{-4}$ W/cm^3	$6.35 \cdot 10^{-4}$ W
0.75 m	$5.38 \cdot 10^{-4}$ W/cm^3	$4.84 \cdot 10^{-3}$ W
1 m	$1.68 \cdot 10^{-3}$ W/cm^3	$2.05 \cdot 10^{-2}$ W
5 m	1.069 W/cm^3	65.0 W

For energy harvesters of length on the order of 1m, this *incorrect* linear extrapolation predicts that each harvester could produce power on the order of Watts. However, for harvesters of such low bending stiffness, the assumption that the projected length of the harvester in the flow remains the same was not expected to remain valid. Accordingly a trade-study of the effect of the length of the harvester on average power was conducted.

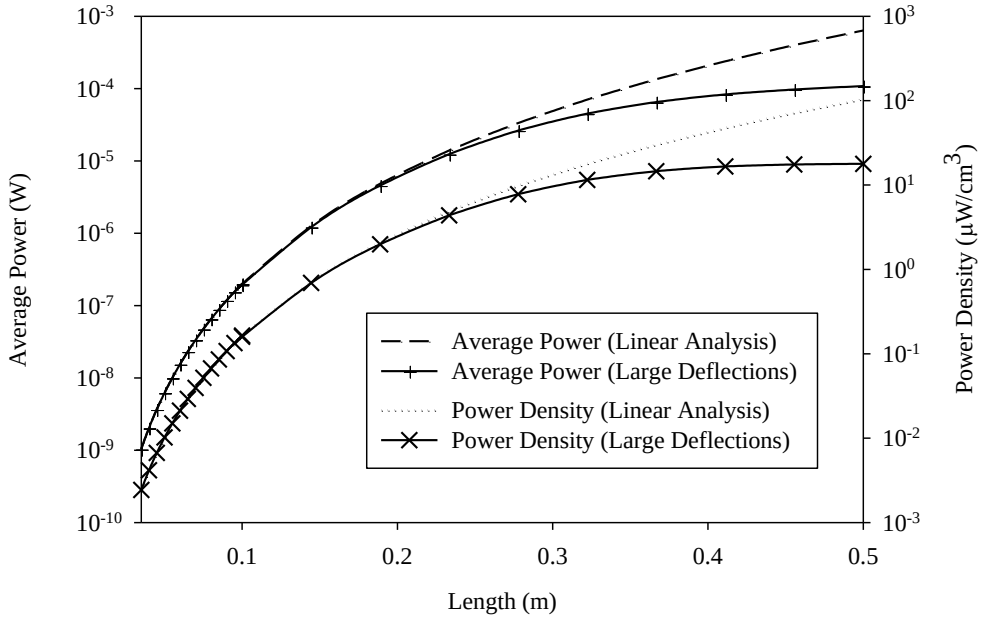

Figure 52: Effect of Length on Power and Power Density for Large Deflections

As can be seen by the results above, even though the extrapolation from linear analysis predicts an increase in power density with the fourth power of the length, the results from the large deflection program predict a much lower power density. The difference in expected power density originated in the harvester undergoing very large deflections. As the harvester was loaded with a larger applied moment relative to the stiffness of the beam, the out of plane deflections began to result in shortening of the projected length in the flow as the total arc length of the harvester was conserved. The maximum deflection and resultant projected length in the flow over the period of

oscillation for the harvester were normalized by the length of the beam and plotted as the length varied. The result can be found below in Figure 53, emphasizing the nonlinearity of high loading scenarios.

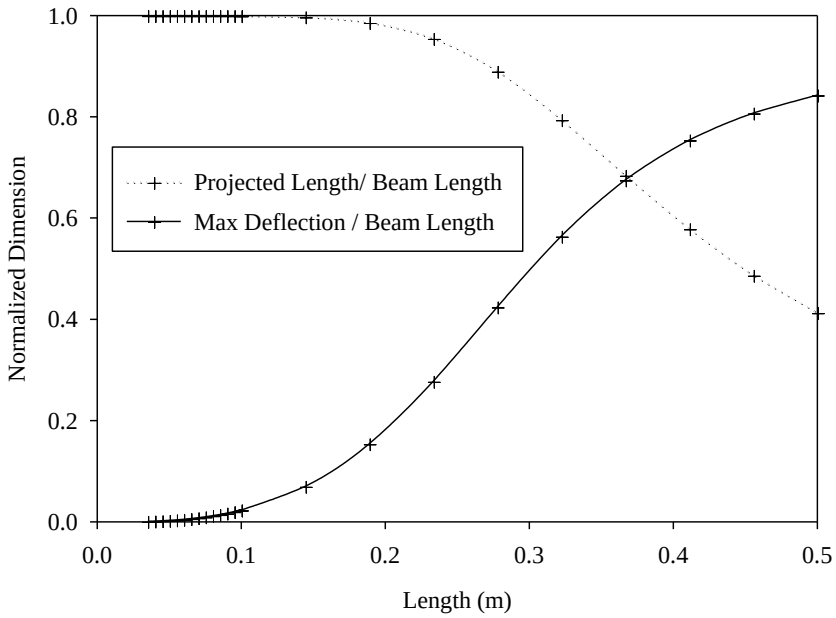

Figure 53: Effect of Length on Bending

Although the above figure only represents the case for the maximum loading scenario over the period of oscillation for the energy harvester, it shows where the divergence from linear theory occurs. As the length of the beam was increased beyond 23 cm, the harvester's projected length at maximum deflection was no longer found to be within 10% of the total harvester length, invalidating the small deflection assumptions. Accordingly, the power density and average power represent a significant deviation of 12.3% by this point. A summary of the results can be found below in Table 13.

Table 13: Comparison of Small and Large Deflection Results

Harvester Length (cm)	Optimized Power from Small Deflection Analysis (W)	Peak Power from Large Deflection Analysis (W)	Percent Difference
3.5	$1.04 \cdot 10^{-9}$	$1.04 \cdot 10^{-9}$	0.12
6.5	$2.31 \cdot 10^{-8}$	$2.31 \cdot 10^{-8}$	-0.06
10.0	$2.00 \cdot 10^{-7}$	$1.94 \cdot 10^{-7}$	3.04
14.4	$1.26 \cdot 10^{-6}$	$1.21 \cdot 10^{-6}$	3.89
18.9	$4.84 \cdot 10^{-6}$	$4.56 \cdot 10^{-6}$	6.11
23.3	$1.39 \cdot 10^{-5}$	$1.24 \cdot 10^{-5}$	12.38
27.8	$3.34 \cdot 10^{-5}$	$2.63 \cdot 10^{-5}$	27.06
32.2	$7.02 \cdot 10^{-5}$	$4.50 \cdot 10^{-5}$	56.08
36.7	$1.34 \cdot 10^{-4}$	$6.50 \cdot 10^{-5}$	106.34
41.1	$2.38 \cdot 10^{-4}$	$8.29 \cdot 10^{-5}$	187.05
45.6	$3.98 \cdot 10^{-4}$	$9.70 \cdot 10^{-5}$	310.45
50.0	$6.35 \cdot 10^{-4}$	$1.08 \cdot 10^{-4}$	485.19

For a PAK constructed with a thickness of 0.64 mm and width 1.9 cm, the maximum power for the harvester was achieved at a length of approximately 50 cm, producing approximately 0.1 mW of average power, albeit at very large deflections. To fully understand the relevance of this figure, a basis was needed to compare the average power produced by the PAK with other systems.

3.3.5 Comparison with Energy Harvesting Literature

Determining an appropriate figure of merit metric to evaluate the effectiveness of an energy harvester was complicated by the need to optimize the effectiveness of the

harvester from a systems-level approach including the source of the power that was harvested. Compared to the electrical power output of the energy harvesting device, the effective source of mechanical power is assumed to be comparatively limitless [16]. By changing the dimensions or shape of the harvester, the effective mechanical input experienced by the harvester was also changed. Several figures of merit involving vibration energy harvesters have been developed that include the amplitude of the source vibration, the frequency of oscillation and the power density [16].

However, significantly fewer metrics have been developed to compare the effectiveness of energy harvesters in a fluid flow. For harvesters utilizing turbine blades, comparison to the Betz coefficient allows for a rough comparison to a theoretical maximum of power that could be extracted from a flow. However, because the PAK does not utilize any moving parts, such metrics were determined not to be useful for comparison. It has been noted in literature that power density does not completely remove the size effect of the harvester from the analysis [16]. According to the analysis presented in this work, the power density for the PAK was determined to be highly dependent upon the thickness and length of the harvester. For lack of a better metric of measurement, both the average power and power density for the PAK harvester for several lengths were compared to other energy harvesting systems of similar loading frequencies. The results were tabulated below in Table 14 for the sample loading conditions previously discussed.

Table 14: Comparison of PAK Concept with Other Energy Harvesting Systems

Device/ Author	Input Frequency (Hz)	Average Power Output (μW)	Harvester Size (cm^3)	Power Density (μW/ cm^3)
3.5 cm PAK	0.85	$1.04 \cdot 10^{-3}$	0.426	$2.43 \cdot 10^{-3}$
10 cm PAK	0.85	0.194	1.216	0.159
50 cm PAK	0.85	108	6.080	17.8
PZT Bimorph/ Elvin [33]	0.5	0.25	0.101	2.47
PVDF Stave/ Kymissis [34]	0.91	1100	19.9	55.2
PZT Unimorph/ Kymissis [34]	0.91	1800	62.5	28.8
PZT Unimorph/ Ramsay [35]	1	2.3	1.1	2.09

As can be seen from the previous table, the power density projected to be available from a 50 cm long PAK harvester corresponds well with the power density of other piezoelectric energy harvesters of similar excitation frequency. At similar frequencies, the maximum power density available from energy harvesters was found to be tens of microwatts per cubic centimeter. To increase the output power density further or additional input power would be needed. The most common method for increasing input excitation is by adding a tip mass or magnet to the beam to provide additional loading. Alternatively, a means could be devised to increase the excitation frequency of the harvester. The majority of energy harvesting literature has focused on harvesting ambient vibrations from sources in the range of 1 Hz to 1 kHz [22]. Recent work has shown that vortex shedding of flows around bluff bodies creates high frequency periodic loading from stable frequency flows [36-39].

3.3.6 Full-Scale Comparison

The full-scale analysis used a harvester length on the order of 10m. The construction used an N-layered Active Beam where the prescribed piezoelectric thickness and epoxy layer thickness were the same as the previous analysis and the number of layers was varied to optimize power. A summary of the construction parameters for the full-scale harvester can be found below in Table 15.

Table 15: Summary of Harvester Parameters for Full-Scale Comparison

Parameter	Value
Beam Length (l)	10 m
Beam Width (b)	1 m
Beam Thickness (h)	N·0.064 mm
Piezo Thickness (t_p)	N·0.052 mm
Number of Active Material Layers	N
Construction Configuration	N-Layered
Active Material	PVDF
Inactive Material	Epoxy (Y_i = 2 GPa)
Connection Pattern	Parallel

The full-scale analysis was conducted using typical wave conditions from coastal waters, shown in Table 16. The results from the analysis are shown in Figure 54.

Table 16: Summary of Conditions Used for Full-Scale comparison

Parameter	Value
Loading-Related Parameters	
Water Depth (d)	15 m
Wave Crest-Trough Distance (H)	0.79 m
Wave Period (τ)	6.7 sec
Calculated Wavelength (L)	63.25 m
Depth Averaged Maximum Flow Speed (u_{max})	22.70 cm/s
Drag Coefficient (C_d)	1.14

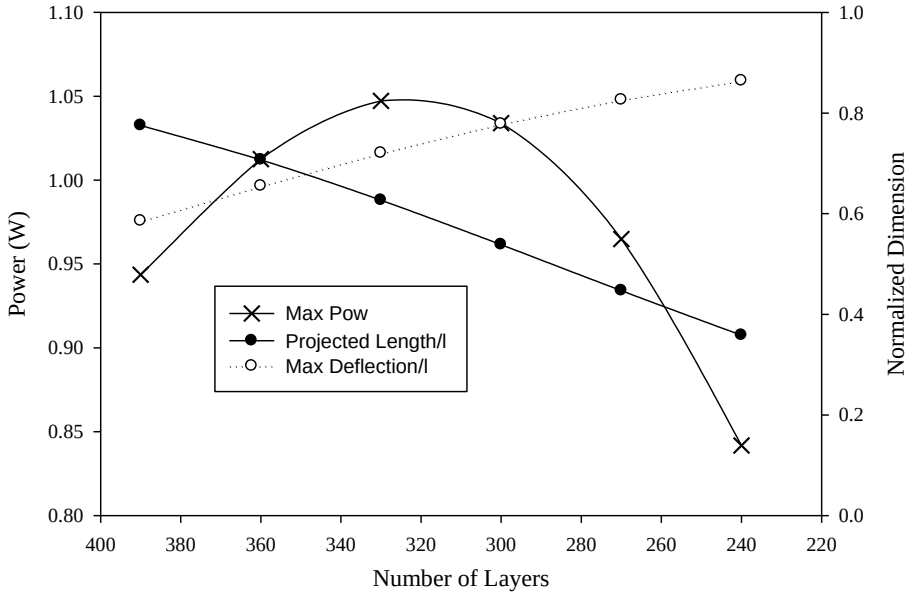

Figure 54: Full Scale-Power Output vs. Number of Layers

As seen in the previous figure, the optimized average power for a full-scale PAK harvester was found to be on the order of 1 Watt. Using this calculation, the number of PAK harvesters required to produce 30 MW of power would be over 30 million. Clearly, the power output per harvester would need to reduce this number to a realistically achievable level. Without additional power production through either redesign or orders

of magnitude greater input loading, it was concluded the PAK would not be able to generate power on usable levels for viability as an alternative power source.

4. SUMMARY AND CONCLUSIONS

The analysis from this work used the PAK concept for a flow-driven energy harvester to effectively compare the effects of design configuration and material choice on average output power. The optimized design configuration and material choice were then extended to a full-scale model to determine the average power output for the PAK concept under typical loading conditions in a coastal environment.

4.1 Summary

The analysis was performed using a quasi-static assumption of a cantilevered beam bending in an oscillating flow. The flow conditions were determined using linear wave theory and the fluid structure interaction was approximated using linear drag theory. The horizontal underwater currents were found using linear wave theory and were assumed to vary proportional to $\sin^2(t)$ with time. A simplified form of Morison's equation was used to find the loading conditions on the harvester where inertial effects are small and the drag coefficient was known for the given application.

The fully-coupled linear piezoelectric constitutive equations were used to couple the beam bending and the circuit voltage response. A simple load resistor in parallel with the energy harvester was used to determine the power produced by the energy harvester. It was shown that when the resistance was optimized for the assumed loading conditions, the average power generated by the harvester could be determined by knowing the magnitude of the charge displacement, the effective piezoelectric capacitance, and the period of the loading. The optimized average power generated by a piezoelectric energy harvester across an optimal load resistor was of the same form as Ottman et. al's circuit for use in charging a battery [6].

The optimized average power was then compared for several common cantilevered energy harvesting configurations. Based on the literature, four common configurations for beam construction were selected: a homogeneous bimorph, a

heterogeneous bimorph, an N-layered active beam, and a unimorph. Initially it was determined that for a harvester of a specified total thickness, the optimal configuration would concentrate the stress in the piezoelectric material by placing the piezoelectric elements on the outer surfaces of the beam and decreasing the stiffness of the supporting material. However, this method of analysis failed to take into account the effect of the size of the harvester. Consequently, a second method of analysis was developed where the thickness of the piezoelectric material was specified. For this method of analysis, the optimal configuration was shown to be the beam with the largest volume fraction of piezoelectric material, i.e. the homogeneous bimorph. The performance of the heterogeneous bimorph and unimorph were also compared, showing that for a relatively compliant inactive material, the unimorph could be used to produce larger amount of power than the heterogeneous bimorph, but the homogeneous bimorph performed best overall. The power output for an N-layered active beam was also derived. It was shown that it could be used to produce power roughly equivalent to that of the homogeneous bimorph for a large number, N, of layers or high piezoelectric volume fraction. This configuration is a practical substitution for the case when the desired thickness of the beam is much thicker than the maximum allowable thickness of a piezoelectric layer, thereby requiring many layers of inactive adhesive to construct the harvester.

Having determined that the homogeneous bimorph configuration results in the highest average power output, the next step of optimization focused on the type of piezoelectric materials: i.e. ceramic vs. polymer. Towards that end, a metric was derived to compare the performance of energy harvesters constructed with various piezoelectric materials for the homogeneous bimorph configuration, namely:

$$\left\langle \hat{P} \right\rangle \sim \frac{k_{31}{}^{2}}{Y_{p}\left(4 - 7k_{31}^{2}\right)}$$

Using the defined metric, PVDF was shown to produce 1.6 times as much power as PZT for a homogeneous bimorph. A first-order Taylor series approximation showed the metric to be on the order of k_{31}^2/Y_p or d_{31}^2/ε for small k_{31}. Although less accurate for large k_{31}, this approximation can be used as a rough approximation for determining the

power produced by a piezoelectric material. Using this first order approximation, PVDF was shown to produce approximately 2.1 times as much power as PZT for a homogeneous bimorph. Although the small k_{31} approximation overestimated the advantage of selecting PVDF over PZT for the harvester, it provided a rough ratio for comparison.

For long, slender beams of low stiffness, an iterative solution program was developed to determine the average power generated by a quasi-static cantilevered bimorph with known loading conditions. The large deflection code followed the technique of Dado et. al approximating the local change in angle of the beam as an N-degree polynomial [32]. Although the technique allowed for complex loading variable over the arc-length, the loading in this work was approximated as a distributed load of constant magnitude. The coefficients of the unknown polynomial coefficient were found using an iterative Newton-Rhapson technique that minimized the integrated error over the arc length of the beam. This minimization was performed at several points over the period of oscillation for the harvester and coupled with the impedance of the circuit to find a steady-state voltage produced by the harvester. The average power produced by the harvester was found by numerically integrating the power produced at each time step over the interval of analysis. This large deflection code was used to explore the theoretical power output of a cantilevered energy harvester undergoing very large deflection and it was also used to generate a realistic approximation of the power that would be produced by a full-scale PAK device.

The predictions for average power were experimentally validated using a small-scale harvester in a wave tank. The loading on the harvester was determined using a strain gage attached to a reference (inactive) beam of the same dimensions and loading conditions. By varying the load resistance and measuring the average power, both the optimized average power and the load resistance predicted for the harvester from small deflection analysis were verified. The PAK concept was then compared to other energy harvesting systems from literature with similar periods of oscillation: i.e. frequency of external load. Through the analysis of volumetric power density, it was determined that

the PAK concept produced volumetric power on the same order as similar cantilevered beam energy harvesting systems. The analysis was extended to a full-scale model with a 10 meter long harvester constructed of an N-layered active beam of PVDF in typical loading condition where the average power produced was determined to be on the order of 1 Watt. Compared to other energy harvesting cantilevered beams in the literature, which often have lengths on the order of 10 cm and produce power on the order of milliwatts, the full-scale PAK system is approximately 2 orders of magnitude longer and produces approximately 3 orders of magnitude higher power.

4.2 Final Conclusions

The optimal configuration of a flow-driven cantilevered energy harvester with specified thickness of piezoelectric element was determined to be a homogeneous bimorph, where the piezoelectric material occupies the entirety of the beam. For thick harvesters where designing a homogeneous bimorph would not be feasible, the homogeneous bimorph configuration could be approximated using the N-layered active beam. Additionally, in contrast to the order of magnitude difference in electromechanical coupling coefficients between PZT and PVDF, harvesters based on PVDF were shown to produce approximately 1.6 times as much power as harvesters constructed using monolithic PZT, for all configurations. This result was surprising considering that PZT has an electromechanical coupling coefficient almost an order of magnitude higher than that of PVDF. This finding also contrasts previous comparisons of piezoelectric materials used in displacement-specified energy harvesting where PZT was shown to have a higher power output than PVDF.

With optimized design and material selection, the PAK concept was shown to have a power density on the order of other piezoelectric energy harvesting concepts. Extended to full scale, the average power output produced by a PAK harvester on the order of 10m would be approximately 1 Watt. Accordingly it was determined that the PAK concept would produce power per square foot occupied much lower than other

alternative energy concepts. To feasibly achieve the goal of a 30 MW off-shore alternative energy plant without building millions of PAK harvesters, the average power by the individual harvester would need to be increased several orders of magnitude to at least 100's of Watts per harvester. Designing a piezoelectric material with higher electromechanical coupling coefficient and lower permittivity would help to increase the output power of the PAK. Additionally, altering the boundary conditions of the harvester so that both ends are fixed could increase the stress on the end of the beam that is currently freely moving, resulting in greater power output. Finally, additional power could be obtained by either increasing the external forcing stimulus (or load) or by operating at a higher input frequency. In each of these scenarios, the large deflection iterative program developed for the analysis of the PAK could be useful for the estimation of power output. The program could also be used to investigate the power output of other flow-driven energy harvesters such as the current focus of cantilevered harvesters behind bluff-bodies in flows.

4.3 Future Work

The previously defined metrics for material comparison in energy harvesters could be used to help materials researchers to identify piezoelectric materials that would have higher power output than currently available materials. As seen in the small k_{31} approximation for the material power multiplier, the power produced by a force-specified cantilevered beam energy harvester scales roughly with the following grouping of piezoelectric material parameters:

$$\left\langle \hat{P} \right\rangle \sim \frac{d_{31}^{\ 2}}{\varepsilon_{33}^{T}} \tag{107}$$

Clearly, piezoelectric materials with a higher piezoelectric coupling coefficient will produce higher average power, however the permittivity of the piezoelectric material must also be considered. Even though piezoceramics typically have coupling coefficients roughly one order of magnitude higher than piezopolymers, piezoceramics also typically

have permittivities at least two orders of magnitude higher than piezopolymers. As a result, marginal increases in coupling coefficient or permittivity of piezopolymers can have large effects on average power. The research in this work shows that the goal for design of future piezoelectric materials would be a material with an increased piezoelectric coupling coefficient and decreased permittivity.

Future research should also seek to experimentally verify the higher average power production of PVDF compared to PZT. Even though the predicted load resistances needed for small PVDF harvesters is very high (~10 MΩ), the present wave tank could be used, and several layers of PVDF in an N-layered active beam configuration could be constructed to verify the analysis for lower load resistances (~1 MΩ). Verification of the previously derived result will aid in further identifying the effect of piezoelectric material choice on average power in piezoelectric energy harvesters in displacement-specified harvesters and force-specified harvesters.

To increase the power output of the PAK system, it is also suggested to investigate alternative configurations for the harvester that would increase the stress along the length of the harvester. One such design concept would be to attach several flotation devices spaced along the length of the harvester. This alternative concept would keep the harvester upright in the water column, while effectively subdividing the harvester to create many smaller beams with clamped boundary conditions on each of their ends. In such a design, the average strain experienced by the beam would increase under the same loading conditions, effectively increasing power output. Additionally, the design limitation for the maximum strain would not be encountered at the root of the beam, but simultaneously across the entire length of the beam.

REFERENCES

[1] G. Cada, J. Ahlgrimm, M. Bahleda, T. Bigford, S. D. Stavrakas*, et al.*, "potential impacts of hydrokinetic and wave energy conversion technologies on aquatic environments," *Fisheries,* vol. 32, pp. 174-181, 2007.

[2] W. D. Callister and D. G. Rethwisch, *Fundamentals of Materials Science and Engineering: An Integrated Approach*: Hoboken, NJ, John Wiley & Sons, 2007.

[3] K. Lefki and G. Dormans, "measurement of piezoelectric coefficients of ferroelectric thin films," *Journal of Applied Physics,* vol. 76, pp. 1764-1767, 1994.

[4] H. A. Sodano, D. J. Inman, and G. Park, "comparison of piezoelectric energy harvesting devices for recharging batteries," *Journal of Intelligent Material Systems and Structures,* vol. 16, p. 799, 2005.

[5] H. Sodano, D. Inman, and G. Park, "a review of power harvesting from vibration using piezoelectric materials," *Shock and Vibration Digest,* vol. 36, pp. 197-206, 2004.

[6] G. K. Ottman, H. F. Hofmann, and G. A. Lesieutre, "optimized piezoelectric energy harvesting circuit using step-down converter in discontinuous conduction mode," *IEEE Transactions on Power Electronics,* vol. 18, pp. 696-703, 2003.

[7] H. A. Sodano, G. Park, and D. Inman, "estimation of electric charge output for piezoelectric energy harvesting," *Strain,* vol. 40, pp. 49-58, 2004.

[8] A. Erturk and D. J. Inman, "on mechanical modeling of cantilevered piezoelectric vibration energy harvesters," *Journal of Intelligent Material Systems and Structures,* vol. 19, p. 1311, 2008.

[9] G. K. Ottman, H. F. Hofmann, A. C. Bhatt, and G. A. Lesieutre, "adaptive piezoelectric energy harvesting circuit for wireless remote power supply," *IEEE Transactions on Power Electronics,* vol. 17, pp. 669-676, 2002.

[10] G. Lesieutre, G. Ottman, and H. Hofmann, "damping as a result of piezoelectric energy harvesting," *Journal of Sound and Vibration,* vol. 269, pp. 991-1001, 2004.

[11] E. Lefeuvre, A. Badel, C. Richard, and D. Guyomar, "piezoelectric energy harvesting device optimization by synchronous electric charge extraction," *Journal of Intelligent Material Systems and Structures,* vol. 16, p. 865, 2005.

[12] M. Lallart, L. Garbuio, L. Petit, C. Richard, and D. Guyomar, "double synchronized switch harvesting (dssh): a new energy harvesting scheme for efficient energy extraction," *IEEE Transactions on Ultrasonics, Ferroelectrics and Frequency Control,* vol. 55, pp. 2119-2130, 2008.

[13] A. Erturk and D. J. Inman, "issues in mathematical modeling of piezoelectric energy harvesters," *Smart Materials and Structures,* vol. 17, p. 065016, 2008.

[14] J. M. Renno, M. F. Daqaq, and D. J. Inman, "on the optimal energy harvesting from a vibration source," *Journal of Sound and Vibration,* vol. 320, pp. 386-405, 2009.

[15] S. Adhikari, M. Friswell, and D. Inman, "piezoelectric energy harvesting from broadband random vibrations," *Smart Materials and Structures,* vol. 18, p. 115005, 2009.

[16] P. D. Mitcheson, E. M. Yeatman, G. K. Rao, A. S. Holmes, and T. C. Green, "energy harvesting from human and machine motion for wireless electronic devices," *Proceedings of the IEEE,* vol. 96, pp. 1457-1486, 2008.

[17] A. Erturk and D. J. Inman, "an experimentally validated bimorph cantilever model for piezoelectric energy harvesting from base excitations," *Smart Materials and Structures,* vol. 18, p. 025009, 2009.

[18] F. Cottone, H. Vocca, and L. Gammaitoni, "nonlinear energy harvesting," *Physical Review Letters,* vol. 102, p. 080601, 2009.

[19] S. C. Stanton, C. C. McGehee, and B. P. Mann, "reversible hysteresis for broadband magnetopiezoelastic energy harvesting," *Applied Physics Letters,* vol. 95, p. 174103, 2009.

[20] S. C. Stanton, C. C. McGehee, and B. P. Mann, "nonlinear dynamics for broadband energy harvesting: investigation of a bistable piezoelectric inertial generator," *Physica D: Nonlinear Phenomena,* vol. 239, pp. 640-653, 2010.

[21] S. C. Stanton, A. Erturk, B. P. Mann, and D. J. Inman, "nonlinear piezoelectricity in electroelastic energy harvesters: modeling and experimental identification," *Journal of Applied Physics,* vol. 108, pp. 074903-074903-9, 2010.

[22] S. Beeby, M. Tudor, and N. White, "energy harvesting vibration sources for microsystems applications," *Measurement Science and Technology,* vol. 17, p. R175, 2006.

[23] D. Vatansever, R. Hadimani, T. Shah, and E. Siores, "an investigation of energy harvesting from renewable sources with pvdf and pzt," *Smart Materials and Structures,* vol. 20, p. 055019, 2011.

[24] J. Fraden, *Handbook of Modern Sensors: Physics, Designs, and Applications*: New York, NY, Springer, 2010.

[25] A. Khaligh, P. Zeng, and C. Zheng, "kinetic energy harvesting using piezoelectric and electromagnetic technologies—state of the art," *IEEE Transactions on Industrial Electronics,* vol. 57, pp. 850-860, 2010.

[26] G. W. Taylor, J. R. Burns, S. Kammann, W. B. Powers, and T. R. Welsh, "the energy harvesting eel: a small subsurface ocean/river power generator," *IEEE Journal of Oceanic Engineering,* vol. 26, pp. 539-547, 2001.

[27] H. Kawai, "the piezoelectricity of poly (vinylidene fluoride)," *Japanese Journal of Applied Physics,* vol. 8, pp. 975-976, 1969.

[28] M. L. Schwartz, *Encyclopedia of Coastal Science.* vol. 24: The Netherlands, Kluwer Academic Pub, 2005.

[29] B. Kinsman, *Wind Waves: Their Generation and Propagation on the Ocean Surface*: Dover Pubns, 2002.

[30] R. E. Randall, *Elements of Ocean Engineering*: Jersey City, NJ, The Society of Naval Architects and Marine Engineers, 1997.

[31] G. B. Airy, "tides and waves," *Encyclopaedia Metropolitana.* 1841.

[32] M. Dado and S. Al-Sadder, "a new technique for large deflection analysis of non-prismatic cantilever beams," *Mechanics Research Communications,* vol. 32, pp. 692-703, 2005.

[33] N. G. Elvin, N. Lajnef, and A. A. Elvin, "feasibility of structural monitoring with vibration powered sensors," *Smart Materials and Structures,* vol. 15, p. 977, 2006.

[34] J. Kymissis, C. Kendall, J. Paradiso, and N. Gershenfeld, "parasitic power harvesting in shoes," *Proceedings of the Second IEEE Conference on Wearable Computing (ISWC)*, pp. 132-139, 1998.

[35] M. J. Ramsay and W. W. Clark, "piezoelectric energy harvesting for bio-mems applications," *Proceedings of SPIE*, p. 429, 2001.

[36] J. Allen and A. Smits, "energy harvesting eel," *Journal of Fluids and Structures,* vol. 15, pp. 629-640, 2001.

[37] S. Pobering, S. Ebermeyer, and N. Schwesinger, "generation of electrical energy using short piezoelectric cantilevers in flowing media," *Proceedings of SPIE*, p. 728807, 2009.

[38] D. Zhu, S. Beeby, J. Tudor, N. White, and N. Harris, "a novel miniature wind generator for wireless sensing applications," *IEEE Sensors 2010*.

[39] B. I. Toolkit, S. G. C. Model, B. Generation, and P. Policy, "design feasibility of a vortex induced vibration based hydro-kinetic energy harvesting system," *IEEE Green Technologies Conference*, pp. 1-6, 2001.

APPENDIX A

WAVE TANK RESTORATION

Initial State:

Sanding:

Caulking:

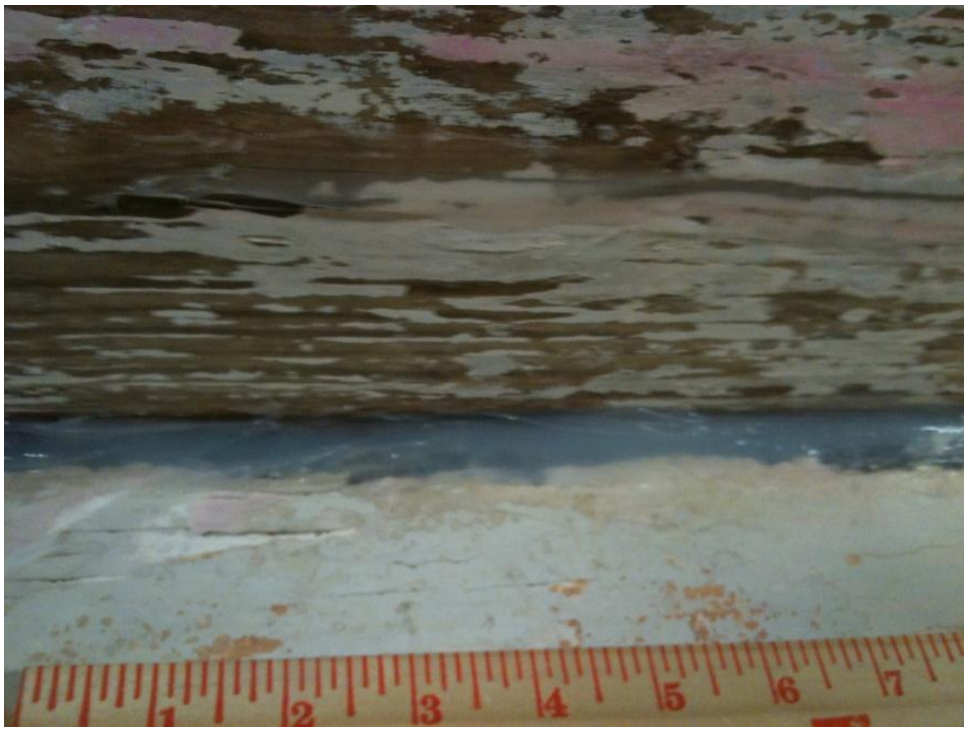

Painting and Waterproof Testing:

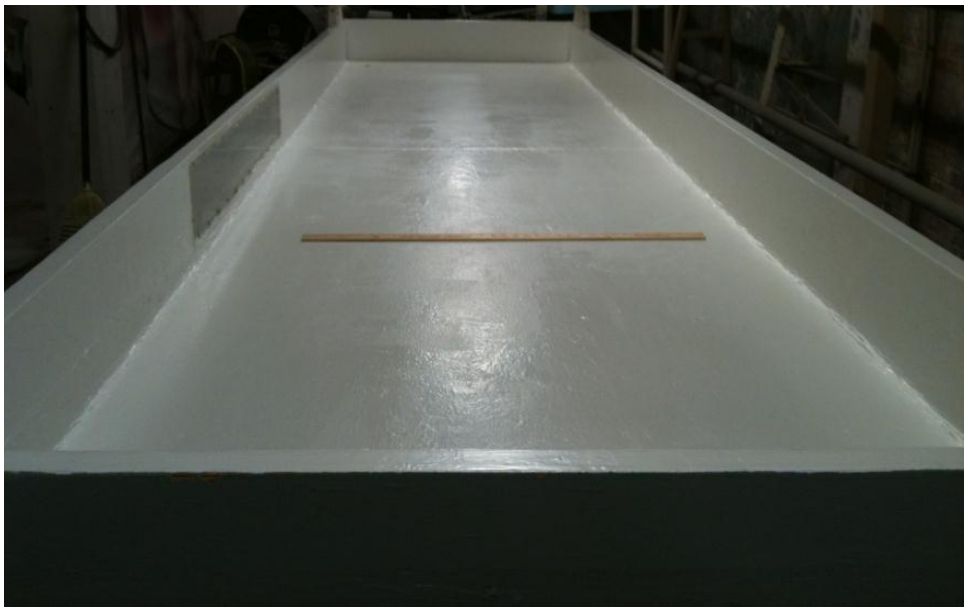

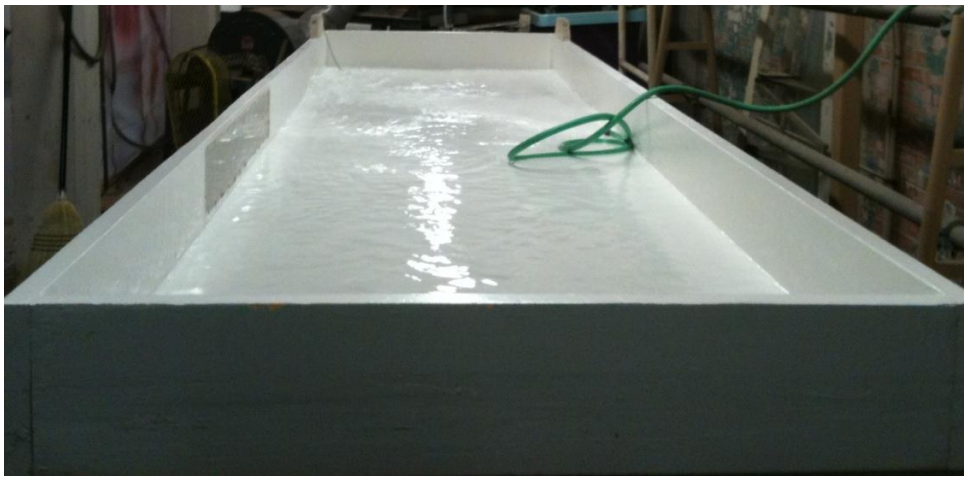

With Sand and Wave Maker:

APPENDIX B

EQUATIONS FROM ANALYSIS

Homogeneous Bimorph:

$$Q_p := \frac{6.\, d_{31}\, b\, \psi}{t_p^2}$$

$$C_p := -\frac{\left(7\, d_{31}^2\, Y_p - 4\, \varepsilon_{33}^T\right) b\, l}{t_p}$$

$$\langle P \rangle := -\frac{43.49811600\, b\, \psi^2\, k_{31}^2}{\tau\, t_p^3\, Y_p \left(7.\, k_{31}^2 - 4.\right) l}$$

$$\Lambda_2 := \frac{b\, \psi^2}{\tau\, t_p^3\, l}$$

$$P_{mult} := -\frac{43.49811600\, k_{31}^2}{Y_p \left(7.\, k_{31}^2 - 4.\right)}$$

Heterogeneous Bimorph:

$$Q_p := \left(6.\, d_{31}\, Y_p \left(2.\, h - 1.\, t_p\right) b\, \psi\right) \Big/ \left(3.\, Y_p\, h^2\, t_p - 3.\, Y_p\, h\, t_p^2 + Y_p\, t_p^3 + Y_i\, h^3 - 3.\, Y_i\, h^2\, t_p + 3.\, Y_i\, h\, t_p^2 - 1.\, Y_i\, t_p^3\right)$$

$$C_p := -\Big(\Big(24\, d_{31}^2\, Y_p^2\, t_p\, h^2 - 24\, d_{31}^2\, Y_p^2\, t_p^2\, h + 7\, d_{31}^2\, Y_p^2\, t_p^3 - 12\, \varepsilon_{33}^T\, Y_p\, h^2\, t_p + 12\, \varepsilon_{33}^T\, Y_p\, h\, t_p^2 - 4\, \varepsilon_{33}^T\, Y_p\, t_p^3 - 4\, \varepsilon_{33}^T\, Y_i\, h^3 + 12\, \varepsilon_{33}^T\, Y_i\, h^2\, t_p - 12\, \varepsilon_{33}^T\, Y_i\, h\, t_p^2 + 4\, \varepsilon_{33}^T\, Y_i\, t_p^3 + 4\, d_{31}^2\, Y_p\, Y_i\, h^3 - 12\, d_{31}^2\, Y_p\, Y_i\, h^2\, t_p + 12\, d_{31}^2\, Y_p\, Y_i\, h\, t_p^2 - 4\, d_{31}^2\, Y_p\, Y_i\, t_p^3\Big)\, b\, l\Big) \Big/ \Big(\Big(3\, Y_p\, h^2\, t_p - 3\, Y_p\, h\, t_p^2 + Y_p\, t_p^3 + Y_i\, h^3 - 3\, Y_i\, h^2\, t_p + 3\, Y_i\, h\, t_p^2 - Y_i\, t_p^3\Big)\, t_p\Big)$$

$$\langle P\rangle := -\left(43.49811600\, Y_p \left(2.\, h - 1.\, t_p\right)^2 b\, \psi^2\, k_{31}^2\, t_p\right) \Big/ \left(\tau \left(3.\, Y_p\, h^2\, t_p - 3.\, Y_p\, h\, t_p^2 + Y_p\, t_p^3 + Y_i\, h^3 - 3.\, Y_i\, h^2\, t_p + 3.\, Y_i\, h\, t_p^2 - 1.\, Y_i\, t_p^3\right) \left(24.\, Y_p\, t_p\, h^2\, k_{31}^2 - 24.\, Y_p\, t_p^2\, h\, k_{31}^2 + 7.\, Y_p\, t_p^3\, k_{31}^2 - 12.\, Y_p\, h^2\, t_p + 12.\, Y_p\, h\, t_p^2 - 4.\, Y_p\, t_p^3 - 4.\, Y_i\, h^3 + 12.\, Y_i\, h^2\, t_p - 12.\, Y_i\, h\, t_p^2 + 4.\, Y_i\, t_p^3 + 4.\, Y_i\, h^3\, k_{31}^2 - 12.\, Y_i\, h^2\, t_p\, k_{31}^2 + 12.\, Y_i\, h\, t_p^2\, k_{31}^2 - 4.\, Y_i\, t_p^3\, k_{31}^2\right) 1\right)$$

$$P_{mult} := -\left(43.49811600\, Y_p \left(2.\, h - 1.\, t_p\right)^2 k_{31}^2\, t_p^4\right) \Big/ \left(\left(3.\, Y_p\, h^2\, t_p - 3.\, Y_p\, h\, t_p^2 + Y_p\, t_p^3 + Y_i\, h^3 - 3.\, Y_i\, h^2\, t_p + 3.\, Y_i\, h\, t_p^2 - 1.\, Y_i\, t_p^3\right) \left(24.\, Y_p\, t_p\, h^2\, k_{31}^2 - 24.\, Y_p\, t_p^2\, h\, k_{31}^2 + 7.\, Y_p\, t_p^3\, k_{31}^2 - 12.\, Y_p\, h^2\, t_p + 12.\, Y_p\, h\, t_p^2 - 4.\, Y_p\, t_p^3 - 4.\, Y_i\, h^3 + 12.\, Y_i\, h^2\, t_p - 12.\, Y_i\, h\, t_p^2 + 4.\, Y_i\, t_p^3 + 4.\, Y_i\, h^3\, k_{31}^2 - 12.\, Y_i\, h^2\, t_p\, k_{31}^2 + 12.\, Y_i\, h\, t_p^2\, k_{31}^2 - 4.\, Y_i\, t_p^3\, k_{31}^2\right)\right)$$

N-Layered Active Laminate:

$$Q_p := \left(3.\, d_{31}\, Y_p\, h\, N^3\, b\, \psi\right) \Big/ \left(Y_i\, h^3\, N^2 + Y_i\, h^2\, t_p - 1.\, Y_p\, h^2\, t_p - 1.\, Y_i\, h^2\, t_p\, N^2 + Y_p\, t_p\, h^2\, N^2 + Y_p\, t_p^3 - 1.\, Y_i\, t_p^3\right)$$

$$C_p := -\frac{1}{4}\left(N^2 \left(-4\, d_{31}^2\, Y_p^2\, t_p\, h^2 - 4\, \varepsilon_{33}^T\, Y_i\, h^3\, N^2 - 4\, \varepsilon_{33}^T\, Y_p\, t_p^3 + 4\, \varepsilon_{33}^T\, Y_i\, t_p^3 + 4\, d_{31}^2\, Y_p^2\, t_p^3 + 4\, d_{31}^2\, Y_p\, Y_i\, h^2\, t_p - 4\, d_{31}^2\, Y_p\, Y_i\, h^2\, t_p\, N^2 - 4\, \varepsilon_{33}^T\, Y_i\, h^2\, t_p + 4\, \varepsilon_{33}^T\, Y_p\, h^2\, t_p + 4\, \varepsilon_{33}^T\, Y_i\, h^2\, t_p\, N^2 - 4\, \varepsilon_{33}^T\, Y_p\, t_p\, h^2\, N^2 + 4\, d_{31}^2\, Y_p\, Y_i\, h^3\, N^2 + 7\, d_{31}^2\, Y_p^2\, t_p\, h^2\, N^2 - 4\, d_{31}^2\, Y_p\, Y_i\, t_p^3\right) b\, 1\right) \Big/ \left(\left(Y_i\, h^3\, N^2 + Y_i\, h^2\, t_p - Y_p\, h^2\, t_p - Y_i\, h^2\, t_p\, N^2 + Y_p\, t_p\, h^2\, N^2 + Y_p\, t_p^3 - Y_i\, t_p^3\right) t_p\right)$$

$$\langle P\rangle := -\left(43.49811600\, Y_p\, h^2\, N^4\, b\, \psi^2\, k_{31}^2\, t_p\right) \Big/ \left(\tau \left(Y_i\, h^3\, N^2 + Y_i\, h^2\, t_p - 1.\, Y_p\, h^2\, t_p - 1.\, Y_i\, h^2\, t_p\, N^2 + Y_p\, t_p\, h^2\, N^2 + Y_p\, t_p^3 - 1.\, Y_i\, t_p^3\right)\left(-4.\, Y_p\, t_p\, h^2\, k_{31}^2 - 4.\, Y_i\, h^3\, N^2 - 4.\, Y_p\, t_p^3 + 4.\, Y_i\, t_p^3 + 4.\, Y_p\, t_p^3\, k_{31}^2 + 4.\, Y_i\, h^2\, t_p\, k_{31}^2 - 4.\, Y_i\, h^2\, t_p\, N^2\, k_{31}^2 - 4.\, Y_i\, h^2\, t_p + 4.\, Y_p\, h^2\, t_p + 4.\, Y_i\, h^2\, t_p\, N^2 - 4.\, Y_p\, t_p\, h^2\, N^2 + 4.\, Y_i\, h^3\, N^2\, k_{31}^2 + 7.\, Y_p\, t_p\, h^2\, N^2\, k_{31}^2 - 4.\, Y_i\, t_p^3\, k_{31}^2\right) 1\right)$$

$$P_{mult} := -\left(43.49811600\, Y_p\, h^2\, N^4\, k_{31}^2\, t_p^4\right) \Big/ \left(\left(Y_i\, h^3\, N^2 + Y_i\, h^2\, t_p - 1.\, Y_p\, h^2\, t_p - 1.\, Y_i\, h^2\, t_p\, N^2 + Y_p\, t_p\, h^2\, N^2 + Y_p\, t_p^3 - 1.\, Y_i\, t_p^3\right)\left(-4.\, Y_p\, t_p\, h^2\, k_{31}^2 - 4.\, Y_i\, h^3\, N^2 - 4.\, Y_p\, t_p^3 + 4.\, Y_i\, t_p^3 + 4.\, Y_p\, t_p^3\, k_{31}^2 + 4.\, Y_i\, h^2\, t_p\, k_{31}^2 - 4.\, Y_i\, h^2\, t_p\, N^2\, k_{31}^2 - 4.\, Y_i\, h^2\, t_p + 4.\, Y_p\, h^2\, t_p + 4.\, Y_i\, h^2\, t_p\, N^2 - 4.\, Y_p\, t_p\, h^2\, N^2 + 4.\, Y_i\, h^3\, N^2\, k_{31}^2 + 7.\, Y_p\, t_p\, h^2\, N^2\, k_{31}^2 - 4.\, Y_i\, t_p^3\, k_{31}^2\right)\right)$$

10-Layered Active Laminate:

$$Q_p := \frac{3000.\, d_{31}\, Y_p\, h\, b\, \psi}{Y_p\, t_p^3 + 100.\, Y_i\, h^3 - 1.\, Y_i\, t_p^3 - 99.\, Y_i\, h^2\, t_p + 99.\, Y_p\, h^2\, t_p}$$

$$C_p := -\left(100\left(174\, d_{31}^2\, Y_p^2\, t_p\, h^2 - \varepsilon_{33}^T\, Y_p\, t_p^3 - 100\, \varepsilon_{33}^T\, Y_i\, h^3 + \varepsilon_{33}^T\, Y_i\, t_p^3 + 99\, \varepsilon_{33}^T\, Y_i\, h^2\, t_p - 99\, \varepsilon_{33}^T\, Y_p\, h^2\, t_p + d_{31}^2\, Y_p^2\, t_p^3 + 100\, d_{31}^2\, Y_p\, Y_i\, h^3 - d_{31}^2\, Y_p\, Y_i\, t_p^3 - 99\, d_{31}^2\, Y_p\, Y_i\, h^2\, t_p\right) b\, 1\right) \Big/ \left(\left(Y_p\, t_p^3 + 100\, Y_i\, h^3 - Y_i\, t_p^3 - 99\, Y_i\, h^2\, t_p + 99\, Y_p\, h^2\, t_p\right) t_p\right)$$

$$\langle P\rangle := -\left(1.087452900\, 10^5\, Y_p\, h^2\, b\, \psi^2\, k_{31}^2\, t_p\right) \Big/ \left(\tau \left(Y_p\, t_p^3 + 100.\, Y_i\, h^3 - 1.\, Y_i\, t_p^3 - 99.\, Y_i\, h^2\, t_p + 99.\, Y_p\, h^2\, t_p\right)\left(174.\, Y_p\, t_p\, h^2\, k_{31}^2 - 1.\, Y_p\, t_p^3 - 100.\, Y_i\, h^3 + Y_i\, t_p^3 + 99.\, Y_i\, h^2\, t_p - 99.\, Y_p\, h^2\, t_p + Y_p\, t_p^3\, k_{31}^2 + 100.\, Y_i\, h^3\, k_{31}^2 - 1.\, Y_i\, t_p^3\, k_{31}^2 - 99.\, Y_i\, h^2\, t_p\, k_{31}^2\right) 1\right)$$

$$P_{mult} := -\left(1.087452900\,10^5\, Y_p\, h^2\, k_{31}^2\, t_p^4\right) \Big/ \left(\left(Y_p\, t_p^3 + 100.\, Y_i\, h^3 - 1.\, Y_i\, t_p^3 - 99.\, Y_i\, h^2\, t_p + 99.\, Y_p\, h^2\, t_p\right)\left(174.\, Y_p\, t_p\, h^2\, k_{31}^2 - 1.\, Y_p\, t_p^3 - 100.\, Y_i\, h^3 + Y_i\, t_p^3 + 99.\, Y_i\, h^2\, t_p - 99.\, Y_p\, h^2\, t_p + Y_p\, t_p^3\, k_{31}^2 + 100.\, Y_i\, h^3\, k_{31}^2 - 1.\, Y_i\, t_p^3\, k_{31}^2 - 99.\, Y_i\, h^2\, t_p\, k_{31}^2\right)\right)$$

Unimorph

$$Q_p := \left(6.\, d_{31}\, Y_p\, h\, Y_i\, b\, \psi\left(h - 1.\, t_p\right)\right) \Big/ \left(h^4\, Y_i^2 - 4.\, h^3\, Y_i^2\, t_p + 4.\, h^3\, Y_i\, Y_p\, t_p + 6.\, h^2\, Y_i^2\, t_p^2 - 6.\, h^2\, Y_i\, t_p^2\, Y_p - 4.\, h\, t_p^3\, Y_i^2 + 4.\, h\, t_p^3\, Y_i\, Y_p + t_p^4\, Y_i^2 - 2.\, t_p^4\, Y_i\, Y_p + t_p^4\, Y_p^2\right)$$

$$C_p := -\left(b\left(7\, d_{31}^2\, Y_p^2\, h\, t_p^3\, Y_i - 12\, d_{31}^2\, Y_p^2\, h^2\, Y_i\, t_p^2 + 8\, d_{31}^2\, Y_p^2\, h^3\, Y_i\, t_p - 4\, d_{31}^2\, Y_p\, h\, t_p^3\, Y_i^2 + 6\, d_{31}^2\, Y_p\, h^2\, Y_i^2\, t_p^2 - 4\, d_{31}^2\, Y_p\, h^3\, Y_i^2\, t_p - 4\, \varepsilon_{33}^T\, h\, t_p^3\, Y_i\, Y_p + 6\, \varepsilon_{33}^T\, h^2\, Y_i\, t_p^2\, Y_p - 4\, \varepsilon_{33}^T\, h^3\, Y_i\, Y_p\, t_p + 4\, \varepsilon_{33}^T\, h\, t_p^3\, Y_i^2 + 2\, \varepsilon_{33}^T\, t_p^4\, Y_i\, Y_p + d_{31}^2\, Y_p\, h^4\, Y_i^2 + d_{31}^2\, Y_p\, t_p^4\, Y_i^2 - 3\, d_{31}^2\, Y_p^2\, t_p^4\, Y_i + 4\, \varepsilon_{33}^T\, h^3\, Y_i^2\, t_p - 6\, \varepsilon_{33}^T\, h^2\, Y_i^2\, t_p^2 + 2\, d_{31}^2\, Y_p^3\, t_p^4 - \varepsilon_{33}^T\, h^4\, Y_i^2 - \varepsilon_{33}^T\, t_p^4\, Y_i^2 - \varepsilon_{33}^T\, t_p^4\, Y_p^2\right) 1\right) \Big/ \left(t_p\left(h^4\, Y_i^2 - 4\, h^3\, Y_i^2\, t_p + 4\, h^3\, Y_i\, Y_p\, t_p + 6\, h^2\, Y_i^2\, t_p^2 - 6\, h^2\, Y_i\, t_p^2\, Y_p - 4\, h\, t_p^3\, Y_i^2 + 4\, h\, t_p^3\, Y_i\, Y_p + t_p^4\, Y_i^2 - 2\, t_p^4\, Y_i\, Y_p + t_p^4\, Y_p^2\right)\right)$$

$$\langle P\rangle := -\left(43.49811600\, Y_p\, h^2\, Y_i^2\, b\, \psi^2\left(h - 1.\, t_p\right)^2\, k_{31}^2\, t_p\right) \Big/ \left(\tau\left(h^4\, Y_i^2 - 4.\, h^3\, Y_i^2\, t_p + 4.\, h^3\, Y_i\, Y_p\, t_p + 6.\, h^2\, Y_i^2\, t_p^2 - 6.\, h^2\, Y_i\, t_p^2\, Y_p - 4.\, h\, t_p^3\, Y_i^2 + 4.\, h\, t_p^3\, Y_i\, Y_p + t_p^4\, Y_i^2 - 2.\, t_p^4\, Y_i\, Y_p + t_p^4\, Y_p^2\right)\left(7.\, Y_p\, h\, t_p^3\, Y_i\, k_{31}^2 - 12.\, Y_p\, h^2\, Y_i\, t_p^2\, k_{31}^2 + 8.\, Y_p\, h^3\, Y_i\, t_p\, k_{31}^2 - 4.\, h\, t_p^3\, Y_i^2\, k_{31}^2 + 6.\, h^2\, Y_i^2\, t_p^2\, k_{31}^2 - 4.\, h^3\, Y_i^2\, t_p\, k_{31}^2 - 4.\, h\, t_p^3\, Y_i\, Y_p + 6.\, h^2\, Y_i\, t_p^2\, Y_p - 4.\, h^3\, Y_i\, Y_p\, t_p + 4.\, h\, t_p^3\, Y_i^2 + 2.\, t_p^4\, Y_i\, Y_p + h^4\, Y_i^2\, k_{31}^2 + t_p^4\, Y_i^2\, k_{31}^2 - 3.\, Y_p\, t_p^4\, Y_i\, k_{31}^2 + 4.\, h^3\, Y_i^2\, t_p - 6.\, h^2\, Y_i^2\, t_p^2 + 2.\, Y_p^2\, t_p^4\, k_{31}^2 - 1.\, h^4\, Y_i^2 - 1.\, t_p^4\, Y_i^2 - 1.\, t_p^4\, Y_p^2\right) 1\right)$$

$$P_{mult} := -\left(43.49811600\, Y_p\, h^2\, Y_i^2\, \left(h - 1.\, t_p\right)^2\, k_{31}^2\, t_p^4\right) \Big/ \left(\left(h^4\, Y_i^2 - 4.\, h^3\, Y_i^2\, t_p + 4.\, h^3\, Y_i\, Y_p\, t_p + 6.\, h^2\, Y_i^2\, t_p^2 - 6.\, h^2\, Y_i\, t_p^2\, Y_p - 4.\, h\, t_p^3\, Y_i^2 + 4.\, h\, t_p^3\, Y_i\, Y_p + t_p^4\, Y_i^2 - 2.\, t_p^4\, Y_i\, Y_p + t_p^4\, Y_p^2\right) \left(7.\, Y_p\, h\, t_p^3\, Y_i\, k_{31}^2 - 12.\, Y_p\, h^2\, Y_i\, t_p^2\, k_{31}^2 + 8.\, Y_p\, h^3\, Y_i\, t_p\, k_{31}^2 - 4.\, h\, t_p^3\, Y_i^2\, k_{31}^2 + 6.\, h^2\, Y_i^2\, t_p^2\, k_{31}^2 - 4.\, h^3\, Y_i^2\, t_p\, k_{31}^2 - 4.\, h\, t_p^3\, Y_i\, Y_p + 6.\, h^2\, Y_i\, t_p^2\, Y_p - 4.\, h^3\, Y_i\, Y_p\, t_p + 4.\, h\, t_p^3\, Y_i^2 + 2.\, t_p^4\, Y_i\, Y_p + h^4\, Y_i^2\, k_{31}^2 + t_p^4\, Y_i^2\, k_{31}^2 - 3.\, Y_p\, t_p^4\, Y_i\, k_{31}^2 + 4.\, h^3\, Y_i^2\, t_p - 6.\, h^2\, Y_i^2\, t_p^2 + 2.\, Y_p^2\, t_p^4\, k_{31}^2 - 1.\, h^4\, Y_i^2 - 1.\, t_p^4\, Y_i^2 - 1.\, t_p^4\, Y_p^2\right)\right)$$

APPENDIX C

MATLAB CODE

Main Large Deflection Voltage Determination Code:

```
% Large Deflection Average Power Calculation
% Alex Pankonien

clc; clear all;close all; format compact;

%*************************************************************************
%************************PRE-RUN SETUP **********************************

%Change the file you want to write to for data
diary('April_13.txt');

%Add debugging if desired
%dbstop in Large_Deflections_Average_Power at 290;

%Start parallelization if supported
if matlabpool('size') == 0 % checking to see if pool is already open
   matlabpool open 2
end

%% *************************************************************************
%************************** USER INPUT ************************************

%-----------------------------------------------
%LOADING CONDITIONS

%Wave Conditions
disp('Wave Conditions in SI');
Crest_trough_distance=0.04 %meters
Water_depth=.127 % meters
Tau_wave=1.25 % seconds

%-----------------------------------------------
%ENERGY HARVESTER CONSTRUCTION

%MATERIAL CHOICE
%PVDF-1,PZT-2
piezo_material=1;
%Aluminum-1,Steel-2,QuickPack Epoxy-3,PVDF Epoxy-4
inactive_material=4;

%BEAM DIMENSIONS
disp('Harvester Dimensions in SI')
if piezo_material==1
   L=.026 %meters
   b=.012 %meters
   h=0.000512 %meters
   piezo_frac=.000416/.000512; %fraction
elseif piezo_material==2
   L=.0462 %meters
   b=.0333 %meters
   h=.000762 %meters
   piezo_frac=.000508/.00762;  %fraction
end

% CONSTRUCTION PARAMETERS
%Homo Bimorph-1,Hetero Bimorph-2, N-Layered Active Laminate-3, Unimorph-4
construction_type=3;
%Number of piezo layers used in construction
```

```
num_layers=8;
%Electrical connection pattern: %Parallel-1,Series-2
connection=1;

% APPROXIMATION PARAMETERS
%Input the number of time steps analyzed over one period of oscillation
num_time_steps=80;
%Degree of polynomial approximation for angle of rotation
deg_poly=13;
%Error criteria for moment balance for a single deflection calculation
TRE_M_individual_criteria=1e-11;
%Error criteria for voltage calculation
TRE_V_error_limit=1e-6;
%Maximum number of voltage iterations allowed for total voltage convergence
Voltage_iteration_limit=10;

%% ************************************************************************
%******************** MATERIAL PARAMETERS TO MEASURE **********************

% APPLY PIEZO MATERIAL PROPERTIES

piezo_mat_names={'PVDF','PZT'};
piezo_mat_names{piezo_material}

switch piezo_material
   case 1 %Piezo Material is PVDF
      c11_E_p=4e9              %Pa
      eps_33_t=12*8.85e-12     %F/m
      d_31=23e-12              %C/N
      R_internal_singlelayer=(10^13); %Ohms
   case 2 %Piezo Material is PZT-5H
      c11_E_p=60.9e9           %Pa
      eps_33_t=1700*8.85e-12   %F/m
      d_31=190e-12             %pC/N
      R_internal_singlelayer=(10^13); %Ohms
end

% APPLY INACTIVE MATERIAL PROPERTIES

inactive_mat_names={'Aluminum','Steel','QuickPack Epoxy','Epon 862'};
inactive_mat_names{inactive_material}

switch inactive_material
   case 1 %Inactive Material is Aluminum
      Y_i=70e9 %Pa
   case 2 %Inactive Material is Steel
      Y_i=200e9 %Pa
   case 3 %Inactive Material QuickPack Epoxy
      Y_i=4.5e9 %Pa
   case 4 %Inactive Material is PVDF Epoxy
      Y_i=2.4e9  %Pa
end

%% ************************************************************************
%********************PRE CONVERGENCE CALCULATIONS**************************

%FOR INTERVAL OF ANALYSIS

%Calculate Total Allowed Error Moment Criteria
TRE_M_combined_error_limit=TRE_M_individual_criteria*num_time_steps;

%Establish individual points of analysis
t_0=0;
end_time=Tau_wave;
delta_t=end_time/num_time_steps; %seconds
```

```
%Note: the last point in time isn't used for the analysis because the first
% and last point in time are the same given analysis of one period
time_space=[0:delta_t:end_time-delta_t];
n_time=length(time_space);

%% FOR BEAM PROPERTIES

%Calculate other material parameters
eps_33_s=eps_33_t-d_31^2*c11_E_p;
e_31=c11_E_p*d_31;
k_31=d_31^2*c11_E_p/eps_33_t;

%Calculate resultant thickness of Piezo Material
t_p=piezo_frac*h;
%Calculate resultant thickness of Inactive Material
t_i=(1-piezo_frac)*h;

%Calculate the thickness of each Piezo Layer
t_p_layer=t_p/num_layers;
%Calculate the thickness of each Inactive Layer
t_i_layer=t_i/num_layers;

%Calculate the position of  the center of each piezo layer
z_mid=zeros(1,num_layers/2); %measured from the bottom of the beam
for layer_number=[1:num_layers/2]
   z_mid(layer_number)=h*layer_number/num_layers-h/(2*num_layers)+h/2;
end

%Define the position of the neutral axis of the beam
switch construction_type
   case 1
      z_star_invariant=h/2; %measured from the bottom of the beam
   case 2
      z_star_invariant=h/2; %measured from the bottom of the beam
   case 3
      z_star_invariant=h/2;%measured from the bottom of the beam
   case 4
      z_star_invariant=1/2*((h^2-(t-t_p)^2)*c11_E_p+(h-t_p)^2*Y_i)/(t_p*c11_E_p+(h-t_p)*Y_i);

end
del_z=z_star_invariant-z_mid;

%Find average distance between piezo layer center and neutral axis
avg_del_z=sum(del_z)/(num_layers/2);

%Find furthest distance between piezo layer center and neutral axis
max_del_z=max(del_z);

%Define Moment/strain and Moment/voltage coupling coefficients
%       Sig_YI              Omega
if(construction_type==1) %homo bimorph
   Sig_YI=b*h^3/12*c11_E_p
   Omega=b*t_p/2*e_31
elseif(construction_type==2) %hetero bimorph
   Sig_YI=b*(h-t_p)^3*(Y_i-c11_E_p)+b*h^3/12*c11_E_p
   Omega=b*(2*h-t_p)/2*e_31
elseif(construction_type==3) %N-Layered active laminate
   Sig_YI=(1/12)*b*Y_i/(num_layers^2)*(-1*t_p^3+h^3*num_layers^2+h^2*t_p-h^2*t_p*num_layers^2)+...
      (1/12)*b*c11_E_p/(num_layers^2)*(-1*h^2*t_p+t_p^3+h^2*t_p*num_layers^2)
   Omega=1/4*b*h*num_layers*e_31;
else                    %unimorph
   Sig_YI=1/12*b*(t_p^4*+c11_E_p^2-2*t_p^4*Y_i*+c11_E_p+4*h*t_p^3*Y_i*...
      c11_E_p-6*h^2*Y_i*t_p^2*c11_E_p+4*h^3*Y_i*c11_E_p*t_p+...
      t_p^4*Y_i^2-4*h*t_p^3*Y_i^2+6*h^2*Y_i^2*t_p^2-4*h^3*Y_i^2*t_p+...
      h^4*Y_i^2)/(Y_i*h-Y_i*t_p+c11_E_p*t_p)
   Omega=1/2*b*Y_i*h*(h-t_p)/(Y_i*h-Y_i*t_p+c11_E_p*t_p)*e_31
```

```
end

%Calculate total capacitance and internal resistance
switch connection
   case 1 %parallel
      C_p_tot=eps_33_s*b*L/(t_p/num_layers)*num_layers
      R_internal=R_internal_singlelayer/num_layers;
   case 2 % series
      C_p_tot=eps_33_s*b*L/t_p
      R_internal=R_internal_singlelayer*num_layers;
end


%% FOR CIRCUIT

%Calculate the approximate optimal load resistance from linear analysis
% First, calculate the adjusted piezo capacitance from linear analysis
if(construction_type==1)   %homogeneous bimorph
  C_p_tot_linear=(4*eps_33_t-7*d_31^2*c11_E_p)*b*L/t_p

elseif(construction_type==2) %heterogeneous bimorph
  C_p_tot_linear=-1*(24*d_31^2*c11_E_p^2*t_p*h^2-24*d_31^2*Yp^2*t_p^2*h+...
     7*d_31^2*c11_E_p^2*t_p^3-12*eps_33_t*c11_E_p*h^2*t_p+12*eps_33_t*...
     c11_E_p*h*t_p^2-4*eps_33_t*c11_E_p*t_p^3-4*eps_33_t*Y_i*h^3+12*...
     eps_33_t*Y_i*h^2*t_p-12*eps_33_t*Y_i*h*t_p^2+4*eps_33_t*...
     Y_i*t_p^3+4*d_31^2*c11_E_p*Y_i*h^3-12*d_31^2*c11_E_p*Y_i*h^2*t_p+...
     12*d_31^2*c11_E_p*Y_i*h*t_p^2-4*d_31^2*c11_E_p*Y_i*t_p^3)/...
     (3*c11_E_p*h^2*t_p-3*c11_E_p*h*t_p^2+c11_E_p*t_p^3+Y_i*h^3-3*...
     Y_i*h^2*t_p+3*Y_i*h*t_p^2-Y_i*t_p^3)*b*L/t_p
elseif(construction_type==3) %N-layered active beam
   C_p_tot_linear=-1/4*num_layers^2*(4*eps_33_t*Y_i*t_p^3-4*eps_33_t*...
      t_p^3*c11_E_p-4*eps_33_t*Y_i*h^3*num_layers^2+4*d_31^2*c11_E_p^2*...
      t_p^3-4*d_31^2*c11_E_p^2*h^2*t_p-4*d_31^2*c11_E_p*Y_i*h^2*t_p*...
      num_layers^2+4*d_31^2*c11_E_p*Y_i*t_p*h^2-4*d_31^2*c11_E_p*Y_i*...
      t_p^3+4*d_31^2*c11_E_p*Y_i*h^3*num_layers^2+4*eps_33_t*Y_i*h^2*...
      t_p*num_layers^2-4*eps_33_t*c11_E_p*t_p*h^2*num_layers^2-4*...
      eps_33_t*Y_i*t_p*h^2+4*eps_33_t*h^2*t_p*c11_E_p+7*d_31^2*c11_E_p^2*...
      t_p*h^2*num_layers^2)/(-Y_i*h^2*t_p*num_layers^2+c11_E_p*t_p*h^2*...
      num_layers^2+Y_i*t_p*h^2-h^2*t_p*c11_E_p-Y_i*t_p^3+t_p^3*c11_E_p+...
      Y_i*h^3*num_layers^2)*b*L/t_p
else                    %unimorph
   C_p_tot_linear=-1*(-6*eps_33_t*h^2*Y_i^2*t_p^2+d_31^2*c11_E_p*...
      t_p^4*Y_i^2+d_31^2*c11_E_p*h^4*Y_i^2+4*eps_33_t*h^3*Y_i^2*t_p+...
      2*d_31^2*c11_E_p^3*t_p^4-eps_33_t*h^4*Y_i^2-eps_33_t*t_p^4*...
      Y_i^2-eps_33_t*t_p^4*c11_E_p^2+4*eps_33_t*h*t_p^3*Y_i^2+...
      2*eps_33_t*t_p^4*Y_i*c11_E_p-4*eps_33_t*h*t_p^3*Y_i*c11_E_p+...
      7*d_31^2*c11_E_p^2*h*t_p^3*Y_i+8*d_31^2*c11_E_p^2*h^3*Y_i*...
      t_p-12*d_31^2*c11_E_p^2*h^2*Y_i*t_p^2-4*eps_33_t*h^3*Y_i*...
      c11_E_p*t_p+6*eps_33_t*h^2*Y_i*t_p^2*c11_E_p+6*d_31^2*c11_E_p*...
      h^2*Y_i^2*t_p^2-4*d_31^2*c11_E_p*h*t_p^3*Y_i^2-4*d_31^2*c11_E_p*...
      h^3*Y_i^2*t_p-3*d_31^2*c11_E_p^2*t_p^4*Y_i)/(t_p^4*c11_E_p^2-2*...
      t_p^4*Y_i*c11_E_p+4*h*t_p^3*Y_i*c11_E_p-6*h^2*Y_i*t_p^2*c11_E_p+...
      4*h^3*Y_i*c11_E_p*t_p+t_p^4*Y_i^2-4*h*t_p^3*Y_i^2+6*h^2*Y_i^2*...
      t_p^2-4*h^3*Y_i^2*t_p+h^4*Y_i^2)*b*L/t_p
end

%Identify relevant circuit parameter: time constant
time_constant_linear=Tau_wave/(R_internal*C_p_tot_linear)

%Establish range for convergence for circuit parameter: R_divider
Rdivider_guess_low=1e0;Rdivider_guess_high=1e8;

%Call bisection method optimization of load resistance
R_load=FindOptimalR(time_constant_linear,R_internal,Rdivider_guess_low,Rdivider_guess_high)

%Calculate total load resistance
```

```
disp('Total Resistance in Circuit');
R_tot=1/(1/R_load+1/R_internal)

%% FOR LOADING

% First,Calculate Maximum Flow Speed

% Calculate Wavelength using iterative method
gravity=9.8; %m/s
Wavelength_old=0;Wavelength_new=1;Wavelength_iteration_count=0;
while Wavelength_iteration_count<10000
   Wavelength_iteration_count=Wavelength_iteration_count+1;
   Wavelength_new=gravity*Tau_wave^2/(2*pi)*tanh(2*pi*Water_depth/Wavelength_old);
   if (abs(Wavelength_old-Wavelength_new)<1e-5)
      break;
   end
   Wavelength_old=Wavelength_new;
end
Wavelength_iteration_count;
Wavelength=Wavelength_new %meters

%Is the shallow water approximation valid?
disp('Is the shallow water approximation valid?');
disp('investigate depth ratio d/L is water depth/wavelength');
disp('d/L>0.5 is deep,0.5>d/L>0.05 is intermediate,0.05>d/L is shallow');
Water_depth/Wavelength
disp('Is above number <0.05?');

%Calculate maximum flow speed
disp('Maximum flow speed (m/s)');
u_max=pi*Crest_trough_distance/Tau_wave*cosh(2*pi/Wavelength*Water_depth/2)/...
   sinh(2*pi/Wavelength*Water_depth) %(m/s)

%Calculate and plot flow speed vs time
u_vs_t=u_max*sin(2*pi/Tau_wave*time_space);
figure;
plot(time_space,u_vs_t,'x-');xlabel('seconds');ylabel('water velocity (m/s)');

%Calculate drag coefficient
disp('drag coefficient');
C_d=0.37*tanh(0.25*L/b-2.6)+1.5

%Calculate resultant loading
rho=1000; %kg/m^3
pressure_vs_t=1/2*C_d*rho*(u_vs_t).^2.*sign(u_vs_t);
qy_vs_t=pressure_vs_t*b;
qy_max=max(qy_vs_t);

%Plot loading versus time
figure;
plot(time_space,qy_vs_t,'-x'); ylabel('Distributed Load Magnitude (N/m)');
xlabel('time (s)');title('Loading vs. time');axis tight;

% Set additional loading conditions
qx=0;Fx=0;Fy=0;Me=0;

% Define cell array of loading at each point in time
Loading_Conditions={};
for k_time=[1:n_time]
   Loading_Conditions{k_time}=[qx,qy_vs_t(k_time),Fx,Fy,Me];
end

%Define Gaussian Quadarature Integration Points and Weights
xi1=[0.0950125098376374,0.281603550779258,0.458016777657227,0.617876244402643,...
0.755404408355003,0.865631202387831,0.944575023073232,0.989400934991649];
xi2=fliplr(-1*xi1);xi=[xi2,xi1];
```

```
sbar_points=1/2*xi+1/2;

w1=[0.094725305227534,0.091301707522462,0.084578096975013,0.074797994408288,...
0.062314485627767,0.047579255841246,0.031126761969324,0.013576229705876];
w2=[0.013576229705876,0.031126761969324,0.047579255841246,0.062314485627767,...
0.074797994408288,0.084578096975013,0.091301707522462,0.094725305227534];
weights=[w2,w1];

%Assemble integration parameters for passing to deflection calculation
Int_Param={TRE_M_individual_criteria,deg_poly,sbar_points,weights};

%% ************************************************************************
%**********************ITERATIVE SOLUTION TECHNIQUE************************

%Initial Voltage Guess
V_old=zeros(1,n_time);

%Initial Curvature Polynomial Coefficient Guess
A_initial_guess=zeros(deg_poly+1,n_time);

%Parameters for Saving Information per iteration later
V_store={};    %Saves voltage vs. time for each iteration
TRE_V_Plot=[]; %Saves Total residual voltage error vs. iteration
TRE_M_Combined_Plot=[]; %Saves Total residual strain error vs. iteration

%Instantiate other  relevant variables
V_new=zeros(1,n_time); %Calculated voltage vs. time.
A_vs_time={};          %Curvature polynomial coefficients vs. time
bending_out={};        %Curvature polynomail coefficient for specific time
TRE_V=1;               %Total residual voltage error
TRE_S=1;               %Total residual strain error
V_count=0;             %Number of iterations required until voltage converges

while(TRE_V>TRE_V_error_limit||TRE_M_combined>TRE_M_combined_error_limit)

   %Increment number of iterations for voltage
   close all;
   disp('****************************************************************')
   disp('****************************************************************')
   disp('Currently on voltage iteration number:')
   V_count=V_count+1
   V_store{V_count}=V_old;

   %% CALCULATE CURVATURE AT EACH TIME STEP
   parfor k_time=(1:n_time)

        %Percent of bending calculations completed for this iteration
        disp('------------------------------------------------------------');
        perc_time=(k_time-1)/(n_time-1)*100;


        %Call Large Deflection bending program
        [bending_out]=Large_Def_Bending(Sig_YI,L,Omega,...
            V_old(k_time),Loading_Conditions{k_time},...
            A_initial_guess(:,k_time),Int_Param,perc_time);

        %The result from the bending code should be sum of a(i) and the Total Residual Error
        %Write output from bending code to arrays
        A_out=bending_out{1};
        TRE_M_individual(k_time)=bending_out{2};

        %Save polynomial coefficients also as guess for next iteration
        A_vs_time{k_time}=A_out;
        A_initial_guess(:,k_time)=A_out;
   end
```

```
%This stores the calculated coefficients for the previous case
%to ensure that all cases have convergent solutions
A_backstore=[A_initial_guess(:,n_time),A_initial_guess(:,2:n_time-1),A_initial_guess(:,1)];

%Check to ensure that all cases have convergent solutions,
%before calculating charge

for k_time=[1:n_time]

   %Calculate displaced charge from layer on average
   Q_3_layer_strain=-1*b*e_31*avg_del_z*sum(A_vs_time{k_time});

   %Apply connection pattern
   if connection==1 %parallel
      Q_3_tot_strain(k_time)=Q_3_layer_strain*num_layers;
   else           %series
      Q_3_tot_strain(k_time)=Q_3_layer_strain;
   end
end

%% CALCULATE VOLTAGES V_new FOR GIVEN STRAINS A_out

%Instantiate Matricies
Over_Z_Matrix=zeros(n_time,n_time);
I_Vector=zeros(n_time,1);

%Assemble Matricies
for v_index=[1:n_time]
   if(v_index==1)
      Over_Z_Matrix(v_index,n_time)=-1*C_p_tot/(2*delta_t);
      Over_Z_Matrix(v_index,v_index)=1/R_tot;
      Over_Z_Matrix(v_index,v_index+1)=C_p_tot/(2*delta_t);
      I_Vector(v_index,1)=(-1*Q_3_tot_strain(n_time)+Q_3_tot_strain(2))/(2*delta_t);
   elseif(v_index==n_time)
      Over_Z_Matrix(v_index,v_index-1)=-1*C_p_tot/(2*delta_t);
      Over_Z_Matrix(v_index,v_index)=1/R_tot;
      Over_Z_Matrix(v_index,1)=C_p_tot/(2*delta_t);
      I_Vector(v_index,1)=(-1*Q_3_tot_strain(n_time-1)+Q_3_tot_strain(1))/(2*delta_t);
   else
      Over_Z_Matrix(v_index,v_index-1)=-1*C_p_tot/(2*delta_t);
      Over_Z_Matrix(v_index,v_index)=1/R_tot;
      Over_Z_Matrix(v_index,v_index+1)=C_p_tot/(2*delta_t);
      I_Vector(v_index,1)=(-1*Q_3_tot_strain(v_index-1)+Q_3_tot_strain(v_index+1))/(2*delta_t);
   end
end

%Solve for new voltages and convert into row array
V_vertical=Over_Z_Matrix\I_Vector;
V_new=V_vertical';

%Calculate total residual error in voltage across timespace between voltage calculations
TRE_V=sum((V_new-V_old).^2)
%Calculate total residual error in moment balance across timespace between voltage calculations
TRE_M_Combined=sum(abs(TRE_M_individual));

%Save Voltages, TRE_Voltage and TRE_Moment for analysis later
V_store{V_count}=V_new;
TRE_V_Plot=[TRE_V_Plot,TRE_V];
TRE_M_Combined_Plot=[TRE_M_Combined_Plot,TRE_M_Combined];

%% ******************OUTPUT FOR CONVERGENCE CHECK**********************
%Plot Charge and current and loading versus time
figure;
subplot(3,1,1);%Charge vs. time
plot(time_space,Q_3_tot_strain);axis tight;
title('Charge Displaced vs. time');
```

```
xlabel('time (s)');ylabel('Charge (Coulombs)');
subplot(3,1,2);%Current vs. time
plot(time_space,I_Vector');axis tight;
title('Current vs. time')
xlabel('time (s)');ylabel('Current (Amps)');
subplot(3,1,3);%Loading vs. time
plot(time_space,q_y*sin(time_space.*2*pi/Tau_wave).^2.*sign(sin(time_space.*2*pi/Tau_wave)),'k-');
axis tight;
title('Loading vs. time');
xlabel('time (s)');ylabel('Distributed Load Magnitude (N/m)');

%Plot Voltage, and Error in Voltage versus time
figure;
subplot(2,1,1);
plot(time_space,V_new,time_space,V_old);ylabel('Voltage (V)');
legend('New Voltage','Old Voltage');title('Change in Voltage between Iterations');
subplot(2,1,2);
plot(time_space,(V_new-V_old)./V_new*100);xlabel('time(seconds)');ylabel('Percent error');
title('Percent Error in Voltage');

%Plot Error in Moment balance vs. time
figure;
up_limit=TRE_M_individual_criteria;
low_limit=up_limit/2;
semilogy(time_space,TRE_M_individual);axis([0 time_space(length(time_space)) low_limit up_limit])
xlabel('time(s)');ylabel('TRE_Moment_individual');title('Error in Moment Balance vs time')

%Plot New Voltage only vs. time
figure;
plot(time_space,V_new);
N=deg_poly;
title(['Voltage Generated for qy=',num2str(q_y),' and N=',num2str(N)]);
xlabel('time (s)');ylabel('Voltage (V)');

%Plot Deflection vs. time
figure;hold on;
del_sbar=.01;        %How fine should the plotting mesh be
s_check=0;
del_s=del_sbar*L;
i_array=[0:1:N];

for k_time=[1:n_time]
   last_x=0;last_y=0;    %Starting point for the graph
   a=A_vs_time{k_time};
   x=[last_x];y=[last_y];
   for sbar=[0:del_sbar:(1-del_sbar)]
      theta_point=sum(a'.*sbar.^i_array);

      del_x=del_s*cos(theta_point);
      last_x=last_x+del_x;
      x=[x,last_x];

      del_y=del_s*sin(theta_point);
      last_y=last_y+del_y;
      y=[y,last_y];

      s_check=s_check+sqrt(1+(tan(theta_point))^2)*del_x;
   end
   if k_time<n_time/2
      plotstr='r-';
   else
      plotstr='k-';
   end
   plot(x,y,plotstr);
end
xlabel('x (m)');ylabel('y(m)');axis([0 L L/(-2) L/2]);
```

```
title(['Deflections of Beam Across Time for qy=',num2str(q_y,3),...
    ' and Target TRE of ',num2str(TRE_M_individual_criteria,'%3.0e\n'),...
    'and \theta =a_0x^0+....a_Nx^N, N=',num2str(N,2)]);
hold off;

%Plot TRE_V and TRE_M_combined versus iteration
figure
subplot(2,1,1);
semilogy([1:V_count],TRE_V_Plot);
ylabel('TRE_V');title('TRE of Voltage');
subplot(2,1,2);
semilogy([1:V_count],TRE_M_Combined_Plot);xlabel('iteration');
ylabel('TRE_M_combined');title('TRE of Moment, Combined across timespace');

%% ************ AVERAGE POWER GENERATED/PERCENT LOST**************
%Average Power Generated Calculation
%Calculate power generated across load resistor
Power_generated=V_new.^2/R_load;

%Integrate the power generated using Simpson's rule
Power_sum=0;
for k=[1:n_time+1]
   if (k==1)
      Power_sum=Power_sum+Power_generated(1);
   elseif (k==(n_time+1))
      Power_sum=Power_sum+Power_generated(1);
   elseif(mod(k,2)==0)
      Power_sum=Power_sum+4*Power_generated(k);
   else
      Power_sum=Power_sum+2*Power_generated(k);
   end
end

disp('Average Power Generated Across Internal Resistance')
Avg_Power_generated=1/Tau_wave*delta_t/3*Power_sum %Watts
Error_in_Power_Generated_Integration=delta_t^4/180*(Tau_wave)*abs(max(Power_generated));

%Average Power Lost Across Internal Resistance
%Calculate average power from the individual voltages
Power_lost=V_new.^2/R_internal;

%Integrate the power generated using Simpson's rule
Power_sum=0;
for k=[1:n_time+1]
   if (k==1)
      Power_sum=Power_sum+Power_lost(1);
   elseif (k==(n_time+1))
      Power_sum=Power_sum+Power_lost(1);
   elseif(mod(k,2)==0)
      Power_sum=Power_sum+4*Power_lost(k);
   else
      Power_sum=Power_sum+2*Power_lost(k);
   end
end

Avg_Power_lost=1/Tau_wave*delta_t/3*Power_sum %Watts
Error_in_Power_Lost_Integration=delta_t^4/180*(Tau_wave)*abs(max(Power_lost));

disp('The Percent Power Lost to internal Resistance')
Avg_Power_lost/(Avg_Power_generated+Avg_Power_lost)*100;


%Escape from the while loop
if(TRE_V<=TRE_V_error_limit) %If the voltages are within error limits
   break;
elseif(V_count>=Voltage_iteration_limit) %if the voltage iteration limit is reached
```

```
      break;
   end

   %Continue to next voltage iteration
   %Make the new voltage into the old voltage
   V_old=V_new;

end

%Plot Final Voltage versus time
figure;
plot(time_space,V_new,'k-'); ylabel('Voltage (V)');axis tight;
title('Voltage Across Load Resistance');

V_count
diary off;
matlabpool close;
```

Large Deflection Bending function:

```
function [a_TRE_output]=Large_Def_Bending(Sum_YI,L,Omeg,V_Applied,Forces_Applied,A_init,Int_Parameters,time_mark);

% Large Deflection Bending Code
% Alex Pankonien
warning off all; format compact;

disp('starting iteration where perc_time=')
time_mark

%% ************************************************************************
% ********************** INPUT  ***********************************

%Strain/Moment coupling-   Sigma YI
%Beam length,          -   L
%Strain/Efield coupling-   Omeg
%Voltage applied       -   Volt
%Forces_Applied

qx=Forces_Applied(1);
qy=Forces_Applied(2),  % qy is the only nonzero loading for this case
Fx=Forces_Applied(3);
Fy=Forces_Applied(4);
Me=Forces_Applied(5);

%Input TRE criteria and degree of polynomial
TRE_Criteria=Int_Parameters{1};
poly_deg=Int_Parameters{2};

%Input numeric integration approximation parameters
int_sbar=Int_Parameters{3};
int_w=Int_Parameters{4};

%% ************************************************************************
% ************** INSTANTIATE CONVERGENCE VARIABLES, MATRICIES

%The maximum number of iterations allowed for convergence
escape_count=1000;
%The minimum number of iterations allowed for convergence
min_count=20;

%Shorter named variables for total number of coefficients to solve for
N=poly_deg;   %paper math, starts counting with 0, important for correct derivatives
M=poly_deg+1; %index count because matlab starts counting with 1

%Instantiate Solution Matrix and Vector
```

```
K=zeros(M-2,M-2);    %"Stiffness" Matrix
f=zeros(M-2,1);      %Loading Vector
i_array=[0:1:N];     %Array of polnomial degrees starting with zero

%% Initial Guess for Coefficients
a=A_init;

%% Pre-Calculate the error for the initial guess
er=zeros(1,length(int_sbar));
for s_index=[1:length(int_sbar)]

  sbar=int_sbar(s_index);

  er(s_index)=(1/L)^2*Sum_YI*sum(i_array.*(i_array-1).*a'.*sbar.^(i_array-2))+...
  ((L)*qy.*(1-sbar)+Fy).*cos(sum(a'.*sbar.^i_array))...
  -1*((L)*qx.*(1-sbar)+Fx).*sin(sum(a'.*sbar.^i_array));
end
integrand=er.*er;
TRE=sum(int_w.*integrand);

%% INSTANTIATE ERROR CONTROL VARIABLES
%Reference Variables
TRE_start=TRE*10^5;

%Count Variables
conv_count=0;

%Storage Variables
TRE_plot=[];last_f=zeros(M-2,1);
cond_plot=[];logcond_plot=[];

%Arrays for derivatives of error
deda=zeros(M,length(int_sbar));
d2eda2=zeros(M-2,M-2,length(int_sbar));
d2eda2_array=zeros(1,length(int_sbar));

%% ***************************************************************************
% CONVERGENCE CALCULATIONS

while TRE>TRE_Criteria || (TRE>1e-20 && conv_count<min_count)

   conv_count=conv_count+1; %Increment convergence count

   % Calculate Second derivative of error: f(i)
   for i=[1:M-2] % Start i coefficient loop
      i_index=i;

      for k_index=[1:length(int_sbar)]

         sbar=int_sbar(k_index);
         deda(i_index,k_index)=(1/L)^2*Sum_YI*(i*(i-1)*sbar.^(i-2))...
         -((L)*qy.*(1-sbar)+Fy).*sin(sum(a'.*sbar.^i_array))*(sbar.^i)...
         -((L)*qx.*(1-sbar)+Fx).*cos(sum(a'.*sbar.^i_array))*(sbar.^i);

      end
      %Integrate numerically to find f
      integrand=er.*deda(i_index,:);
      f(i_index)=sum(int_w.*integrand);
   end

   % Calculate first derivative of error: K(i,j)

   for i=[1:M-2] % Start i coefficient loop
         i_index=i;
         for j=[1:M-2] % Start j coefficient loop
            j_index=j;
```

```
        %Find the value of the second derivative at all of the integration points and store it in an array;
        for s_index=[1:length(int_sbar)] % Start loop for sbar, use dummy variable

           sbar=int_sbar(s_index);

           d2eda2_point=-1*(L*qy.*(1-sbar)+Fy).*...
           cos(sum(a'.*sbar.^i_array)).*(sbar.^i).*(sbar.^j)...
           +1*(L*qx.*(1-sbar)+Fx).*...
           (sin(sum(a'.*sbar.^i_array)).*(sbar.^i).*(sbar.^j));

           d2eda2_array(s_index)=d2eda2_point;
        end

        d2eda2(i_index,j_index,:)=d2eda2_array;

        %Integrate to find Kij
        integrand=deda(i_index,:).*deda(j_index,:)+er.*d2eda2_array;
        K(i_index,j_index)=sum(int_w.*integrand);

     end
end

%% SOLVE FOR NEW COEFFICIENTS
% Solve for change in coeefficients
del_a=K\f;

% Implement boundary conditions
%Enforce B.C. at s=0
first_coef=0;

%Enforce B.C. at s=1
short_a_new=short_a-del_a;
%using first consitutive relation
last_coef_new=-1/N*(sum(i_array(1:M-1).*[first_coef;short_a_new]')+1*Omeg*V_Applied*L/Sum_YI);

%Combined calculated coefficients to form new guess for coefficients
a_new=[first_coef;short_a_new;last_coef_new];

%% CALCULATE TRE_M USING NEW COEFFICIENTS
%Calculate the error at each integration point
for k_index=[1:length(int_sbar)]
   sbar=int_sbar(k_index);

   er(k_index)=(1/L)^2*Sum_YI*sum(i_array.*(i_array-1).*a_new'.*sbar.^(i_array-2))+...
   (L*qy.*(1-sbar)+Fy).*cos(sum(a_new'.*sbar.^i_array))...
   -1*(L*qx.*(1-sbar)+Fx).*sin(sum(a_new'.*sbar.^i_array));
end

%Calculate Total Residual error by integrating the error over the length domain
integrand=er.*er;
TRE=sum(int_w.*integrand);

%Make changes in coefficients final
short_a=short_a_new;
a=a_new;

%% STORE VARIABLES FOR PLOTTING*****************************
%Store TRE for Plot in Output
TRE_plot(conv_count)=TRE;

%% ESCAPE CRITERIA ************************************
%Break if error limit was not reached
if(conv_count>escape_count)
   disp('error criteria was not reached')
   conv_count;
```

```
        break;
    end

end

%% ******************************OUTPUT*********************************
%Summary of variables to be passed out of program
disp('finished iteration for perc_time=')
time_mark
disp('and loading=')
qy
disp('a')
a'
disp('the number of counts for strain convergence were');
conv_count
disp('TRE')
TRE

%% OUTPUT PARAMETERS PASSED TO ORIGINAL PROGRAM*********************
a_TRE_output{1}=a;
a_TRE_output{2}=TRE;
```

Load Resistance Optimization function:

```
function [ Optimal_Rload ] = FindOptimalR(timeconst,R_internal,Rdiv_low,Rdiv_high )

Rdiv_mid=(Rdiv_low+Rdiv_high)/2;
Pi=pi;

for R_conv_count=1:1000

    %escape criteria
    delta_R_rel=((R_internal/Rdiv_high)-(R_internal/Rdiv_low))/(R_internal/Rdiv_mid);
    if (abs(delta_R_rel)<1e-10)
        break;
    end

    Rdiv_array=[Rdiv_low,Rdiv_mid,Rdiv_high];
    for which_Rdiv=1:3

        Rdivider=Rdiv_array(which_Rdiv);
        diffAvPow=2*(8*exp(1/2*timeconst*(1+Rdivider))*Pi^2*timeconst^2+...
            8*exp(1/2*timeconst*(1+Rdivider))*Pi^2*timeconst^2*Rdivider+...
            80*exp(1/2*timeconst*(1+Rdivider))*Pi^2*timeconst+3/2*exp(1/2*...
            timeconst*(1+Rdivider))*timeconst^4*Rdivider^2+6*exp(1/2*timeconst...
            *(1+Rdivider))*timeconst^3*Rdivider+1/2*exp(1/2*timeconst*(1+...
            Rdivider))*timeconst^4*Rdivider^3+3*exp(1/2*timeconst*(1+Rdivider...
            ))*timeconst^3*Rdivider^2+16*Pi^2*timeconst+32*Pi^2*timeconst*...
            exp(-2*timeconst*(1+Rdivider))-72*Pi^2*timeconst*exp(-1/2*timeconst...
            *(1+Rdivider))-72*Pi^2*timeconst*exp(-3/2*timeconst*(1+Rdivider))...
            +112*Pi^2*timeconst*exp(-timeconst*(1+Rdivider))+3/2*...
            exp(1/2*timeconst*(1+Rdivider))*timeconst^4*Rdivider+3*exp(1/2*...
            timeconst*(1+Rdivider))*timeconst^3+3*timeconst^3+6*timeconst^3*...
            Rdivider+3*timeconst^3*Rdivider^2+1/2*exp(1/2*timeconst*(1+Rdivider...
            ))*timeconst^4)*Pi^2*Rdivider/(4*exp(1/2*timeconst*(1+Rdivider))*...
            timeconst^4*Rdivider+6*exp(1/2*timeconst*(1+Rdivider))*timeconst^4*...
            Rdivider^2+4*exp(1/2*timeconst*(1+Rdivider))*timeconst^4*Rdivider^3+...
            exp(1/2*timeconst*(1+Rdivider))*timeconst^4*Rdivider^4+32*exp(1/2*...
            timeconst*(1+Rdivider))*Pi^2*timeconst^2+64*exp(1/2*timeconst*(1+...
            Rdivider))*Pi^2*timeconst^2*Rdivider+32*exp(1/2*timeconst*(1+...
            Rdivider))*Pi^2*timeconst^2*Rdivider^2+256*Pi^4*exp(1/2*timeconst*...
            (1+Rdivider))+exp(1/2*timeconst*(1+Rdivider))*timeconst^4+4*...
            timeconst^4*Rdivider+6*timeconst^4*Rdivider^2+4*timeconst^4*...
            Rdivider^3+timeconst^4*Rdivider^4+32*Pi^2*timeconst^2+64*Pi^2*...
            timeconst^2*Rdivider+32*Pi^2*timeconst^2*Rdivider^2+256*Pi^4+...
```

```
timeconst^4)/(1+Rdivider)+2*(16*exp(1/2*timeconst*(1+Rdivider))*...
Pi^2*timeconst+16*exp(1/2*timeconst*(1+Rdivider))*Pi^2*timeconst*...
Rdivider+16*Pi^2*timeconst-192*Pi^2+3*exp(1/2*timeconst*(1+...
Rdivider))*timeconst^3*Rdivider^2+exp(1/2*timeconst*(1+Rdivider))*...
timeconst^3*Rdivider^3+16*Pi^2*timeconst*Rdivider-16*Pi^2*exp(-2*...
timeconst*(1+Rdivider))+timeconst^3+144*Pi^2*exp(-1/2*timeconst*(1+...
Rdivider))+48*Pi^2*exp(-3/2*timeconst*(1+Rdivider))-112*Pi^2*exp(-timeconst*...
(1+Rdivider))+3*exp(1/2*timeconst*(1+Rdivider))*timeconst^3*Rdivider+3*timeconst...
^3*Rdivider+3*timeconst^3*Rdivider^2+timeconst^3*Rdivider^3+128*Pi^2*...
exp(1/2*timeconst*(1+Rdivider))+exp(1/2*timeconst*(1+Rdivider))*...
timeconst^3)*Pi^2/(4*exp(1/2*timeconst*(1+Rdivider))*timeconst^4*...
Rdivider+6*exp(1/2*timeconst*(1+Rdivider))*timeconst^4*Rdivider^2+4*...
exp(1/2*timeconst*(1+Rdivider))*timeconst^4*Rdivider^3+exp(1/2*timeconst*...
(1+Rdivider))*timeconst^4*Rdivider^4+32*exp(1/2*timeconst*(1+Rdivider))*...
Pi^2*timeconst^2+64*exp(1/2*timeconst*(1+Rdivider))*Pi^2*timeconst^2*...
Rdivider+32*exp(1/2*timeconst*(1+Rdivider))*Pi^2*timeconst^2*Rdivider^2+...
256*Pi^4*exp(1/2*timeconst*(1+Rdivider))+exp(1/2*timeconst*(1+Rdivider))*...
timeconst^4+4*timeconst^4*Rdivider+6*timeconst^4*Rdivider^2+4*timeconst^4*...
Rdivider^3+timeconst^4*Rdivider^4+32*Pi^2*timeconst^2+64*Pi^2*timeconst^2*...
Rdivider+32*Pi^2*timeconst^2*Rdivider^2+256*Pi^4+timeconst^4)/(1+Rdivider)-2*...
(16*exp(1/2*timeconst*(1+Rdivider))*Pi^2*timeconst+16*exp(1/2*timeconst*(1+Rdivider))*...
Pi^2*timeconst*Rdivider+16*Pi^2*timeconst-192*Pi^2+3*exp(1/2*timeconst*(1+Rdivider))*...
timeconst^3*Rdivider^2+exp(1/2*timeconst*(1+Rdivider))*timeconst^3*Rdivider^3+16*Pi^2*...
timeconst*Rdivider-16*Pi^2*exp(-2*timeconst*(1+Rdivider))+timeconst^3+144*Pi^2*exp(-1/2*...
timeconst*(1+Rdivider))+48*Pi^2*exp(-3/2*timeconst*(1+Rdivider))-112*Pi^2*exp(-timeconst*...
(1+Rdivider))+3*exp(1/2*timeconst*(1+Rdivider))*timeconst^3*Rdivider+3*timeconst^3*Rdivider+3*...
timeconst^3*Rdivider^2+timeconst^3*Rdivider^3+128*Pi^2*exp(1/2*timeconst*(1+Rdivider))+...
exp(1/2*timeconst*(1+Rdivider))*timeconst^3)*Pi^2*Rdivider/(4*exp(1/2*timeconst*(1+Rdivider))*…
timeconst^4*Rdivider+6*exp(1/2*timeconst*(1+Rdivider))*timeconst^4*Rdivider^2+4*exp(1/2*timeconst*...
(1+Rdivider))*timeconst^4*Rdivider^3+exp(1/2*timeconst*(1+Rdivider))*timeconst^4*Rdivider^4+32*exp(1/2*...
timeconst*(1+Rdivider))*Pi^2*timeconst^2+64*exp(1/2*timeconst*(1+Rdivider))*Pi^2*timeconst^2*...
Rdivider+32*exp(1/2*timeconst*(1+Rdivider))*Pi^2*timeconst^2*Rdivider^2+256*Pi^4*exp(1/2*timeconst*...
(1+Rdivider))+exp(1/2*timeconst*(1+Rdivider))*timeconst^4+4*timeconst^4*Rdivider+6*timeconst^4*...
Rdivider^2+4*timeconst^4*Rdivider^3+timeconst^4*Rdivider^4+32*Pi^2*timeconst^2+64*Pi^2*timeconst^2*...
Rdivider+32*Pi^2*timeconst^2*Rdivider^2+256*Pi^4+timeconst^4)^2/(1+Rdivider)*(2*timeconst^5*exp(1/2*timeconst...
*(1+Rdivider))*Rdivider+4*exp(1/2*timeconst*(1+Rdivider))*timeconst^4+3*timeconst^5*exp(1/2*...
timeconst*(1+Rdivider))*Rdivider^2+12*exp(1/2*timeconst*(1+Rdivider))*timeconst^4*Rdivider+2*...
timeconst^5*exp(1/2*timeconst*(1+Rdivider))*Rdivider^3+12*exp(1/2*timeconst*(1+Rdivider))*...
timeconst^4*Rdivider^2+1/2*timeconst^5*exp(1/2*timeconst*(1+Rdivider))*Rdivider^4+4*exp(1/2*...
timeconst*(1+Rdivider))*timeconst^4*Rdivider^3+16*timeconst^3*exp(1/2*timeconst*(1+Rdivider...
))*Pi^2+32*timeconst^3*exp(1/2*timeconst*(1+Rdivider))*Pi^2*Rdivider+64*exp(1/2*timeconst*...
(1+Rdivider))*Pi^2*timeconst^2+16*timeconst^3*exp(1/2*timeconst*(1+Rdivider))*Pi^2*Rdivider^2+...
64*exp(1/2*timeconst*(1+Rdivider))*Pi^2*timeconst^2*Rdivider+128*Pi^4*timeconst*exp(1/2*timeconst*...
(1+Rdivider))+1/2*timeconst^5*exp(1/2*timeconst*(1+Rdivider))+4*timeconst^4+12*timeconst^4*Rdivider+...
12*timeconst^4*Rdivider^2+4*timeconst^4*Rdivider^3+64*Pi^2*timeconst^2+...
64*Pi^2*timeconst^2*Rdivider)-2*(16*exp(1/2*timeconst*(1+Rdivider))*Pi^2*timeconst+...
16*exp(1/2*timeconst*(1+Rdivider))*Pi^2*timeconst*Rdivider+16*Pi^2*timeconst-192*Pi^2+...
3*exp(1/2*timeconst*(1+Rdivider))*timeconst^3*Rdivider^2+exp(1/2*timeconst*(1+Rdivider))*...
timeconst^3*Rdivider^3+16*Pi^2*timeconst*Rdivider-16*Pi^2*exp(-2*timeconst*(1+Rdivider))+...
timeconst^3+144*Pi^2*exp(-1/2*timeconst*(1+Rdivider))+48*Pi^2*exp(-3/2*timeconst*(1+Rdivider))-...
112*Pi^2*exp(-timeconst*(1+Rdivider))+3*exp(1/2*timeconst*(1+Rdivider))*timeconst^3*Rdivider+...
3*timeconst^3*Rdivider+3*timeconst^3*Rdivider^2+timeconst^3*Rdivider^3+128*Pi^2*exp(1/2*timeconst*...
(1+Rdivider))+exp(1/2*timeconst*(1+Rdivider))*timeconst^3)*Pi^2*Rdivider/(4*exp(1/2*timeconst*(1+Rdivider))*...

timeconst^4*Rdivider+6*exp(1/2*timeconst*(1+Rdivider))*timeconst^4*Rdivider^2+4*exp(1/2*timeconst*(1+Rdivider))*...
timeconst^4*Rdivider^3+exp(1/2*timeconst*(1+Rdivider))*timeconst^4*Rdivider^4+32*...
exp(1/2*timeconst*(1+Rdivider))*Pi^2*timeconst^2+64*exp(1/2*timeconst*(1+Rdivider))*...
Pi^2*timeconst^2*Rdivider+32*exp(1/2*timeconst*(1+Rdivider))*Pi^2*timeconst^2*Rdivider^2+...
256*Pi^4*exp(1/2*timeconst*(1+Rdivider))+exp(1/2*timeconst*(1+Rdivider))*timeconst^4+...
4*timeconst^4*Rdivider+6*timeconst^4*Rdivider^2+4*timeconst^4*Rdivider^3+timeconst^4*...
Rdivider^4+32*Pi^2*timeconst^2+64*Pi^2*timeconst^2*Rdivider+32*Pi^2*timeconst^2*Rdivider^2+...
256*Pi^4+timeconst^4)/(1+Rdivider)^2;
switch which_Rdiv
   case 1 % low
      diffAvPow_low=diffAvPow;
   case 2 % mid
```

```
            diffAvPow_mid=diffAvPow;
          case 3 % high
            diffAvPow_high=diffAvPow;
        end
    end

    if sign(diffAvPow_low)>0&&sign(diffAvPow_mid)<0&&sign(diffAvPow_high)<0 %root  is between rload low and rload mid
        Rdiv_high=Rdiv_mid;
    elseif sign(diffAvPow_low)>0&&sign(diffAvPow_mid)>0&&sign(diffAvPow_high)<0 %root is between rload mid and rload
high
        Rdiv_low=Rdiv_mid;
    elseif sign(diffAvPow_low)==sign(diffAvPow_high)
        %picked bad initial points resulting in bad optimization
        Rdiv_low=Rdiv_low*10;
        Rdiv_high=Rdiv_high/10;
    else
        %Fix nan problems
        if isnan(diffAvPow_low)
            Rdiv_low=Rdiv_low*10;
        end
        if isnan(diffAvPow_high)
            Rdiv_high=Rdiv_high/10;
        end
    end

    Rdiv_mid=(Rdiv_low+Rdiv_high)/2;
end

Rdivider=Rdiv_mid;
NondimAvPow=2*((timeconst^3+exp(1/2*timeconst*(1+Rdivider))*timeconst^3)*...
        Rdivider^3+(3*exp(1/2*timeconst*(1+Rdivider))*timeconst^3+3*timeconst^3)*...
        Rdivider^2+(16*exp(1/2*timeconst*(1+Rdivider))*Pi^2*timeconst+3*timeconst^3+...
        16*Pi^2*timeconst+3*exp(1/2*timeconst*(1+Rdivider))*timeconst^3)*Rdivider+...
        16*exp(1/2*timeconst*(1+Rdivider))*Pi^2*timeconst+144*Pi^2*...
        exp(-1/2*timeconst*(1+Rdivider))+16*Pi^2*timeconst-192*Pi^2+...
        exp(1/2*timeconst*(1+Rdivider))*timeconst^3+48*Pi^2*...
        exp(-3/2*timeconst*(1+Rdivider))-16*Pi^2*exp(-2*timeconst*(1+Rdivider))...
        +timeconst^3-112*Pi^2*exp(-timeconst*(1+Rdivider))+128*Pi^2*exp(1/2*...
        timeconst*(1+Rdivider)))*Pi^2*Rdivider/((timeconst^4+exp(1/2*timeconst*...
        (1+Rdivider))*timeconst^4)*Rdivider^4+(4*timeconst^4+4*exp(1/2*timeconst*...
        (1+Rdivider))*timeconst^4)*Rdivider^3+(32*Pi^2*timeconst^2+32*exp(1/2*timeconst...
        *(1+Rdivider))*Pi^2*timeconst^2+6*timeconst^4+6*exp(1/2*timeconst*(1+Rdivider))...
        *timeconst^4)*Rdivider^2+(64*Pi^2*timeconst^2+64*exp(1/2*timeconst*(1+Rdivider))...
        *Pi^2*timeconst^2+4*timeconst^4+4*exp(1/2*timeconst*(1+Rdivider))*timeconst^4)...
        *Rdivider+32*Pi^2*timeconst^2+timeconst^4+256*Pi^4+32*exp(1/2*timeconst*(1+...
        Rdivider))*Pi^2*timeconst^2+256*Pi^4*exp(1/2*timeconst*(1+Rdivider))+...
        exp(1/2*timeconst*(1+Rdivider))*timeconst^4)/(1+Rdivider);
percentoffinAvPow=(NondimAvPow-1.208277)/1.208277*100
Optimal_Rload=R_internal/Rdiv_mid;
```

VITA

Alexander Morgan Pankonien received his Bachelor of Science degree in aerospace engineering from Texas A&M University in 2009. He then continued the pursuit of his studies at Texas A&M University in September 2009 and received his Master of Science degree in August 2011. His research interests include multifunctional materials and multi-physics interactions. He plans to continue his research at the University of Michigan in the Fall of 2011.

Mr. Pankonien may be reached at 701 H.R. Bright Building, Aerospace Engineering Department, College Station, TX 77843. His email is apankon87@tamu.edu.